Department of Applied Physics

Domain Wall Coupling in Ferromagnetic/ Ferroelectric Heterostructures: Scaling Behaviour and Electric Field Driven Motion

Kévin Franke

Aalto University

DOCTORAL DISSERTATIONS

Aalto University publication series
DOCTORAL DISSERTATIONS 95/2016

Domain Wall Coupling in Ferromagnetic/ Ferroelectric Heterostructures: Scaling Behaviour and Electric Field Driven Motion

Kévin Franke

A doctoral dissertation completed for the degree of Doctor of Science (Technology) to be defended, with the permission of the Aalto University School of Science, at a public examination held at the lecture hall T2 (Konemiehentie 2, Espoo) of the school on 17 June 2016 at 12.

Aalto University
School of Science
Department of Applied Physics
Nanomagnetism and Spintronics

Supervising professor
Prof. Sebastiaan van Dijken

Thesis advisor
Prof. Sebastiaan van Dijken

Preliminary examiners
Prof. Kathrin Dörr, Martin Luther University of Halle-Wittenberg, Germany
Dr. Thomas Moore, University of Leeds, United Kingdom

Opponent
Prof. Bert Koopmans, Eindhoven University of Technology, Netherlands

Aalto University publication series
DOCTORAL DISSERTATIONS 95/2016

ISBN 978-952-60-6816-9 (printed)
ISBN 978-952-60-6817-6 (pdf)
ISSN-L 1799-4934
ISSN 1799-4934 (printed)
ISSN 1799-4942 (pdf)
http://urn.fi/URN:ISBN:978-952-60-6817-6

Unigrafia Oy
Helsinki 2016

Finland

NORDIC ECOLABEL
441 697
Printed matter

Aalto University

Abstract

Aalto University, P.O. Box 11000, FI-00076 Aalto www.aalto.fi

Author
Kévin Franke

Name of the doctoral dissertation
Domain Wall Coupling in Ferromagnetic/Ferroelectric Heterostructures: Scaling Behaviour and Electric Field Driven Motion

Publisher School of Science

Unit Department of Applied Physics

Series Aalto University publication series DOCTORAL DISSERTATIONS 95/2016

Field of research Engineering Physics

Manuscript submitted 11 March 2016 **Date of the defence** 17 June 2016

Permission to publish granted (date) 4 May 2016 **Language** English

☐ **Monograph** ☒ **Article dissertation** ☐ **Essay dissertation**

Abstract

Ferromagnetic and ferroelectric materials exhibit an order parameter that can be controlled and switched with an external field conjugate to it. This property has been used in practical applications such as memory devices or sensors. In an effort to further scale down the size and energy consumption of devices, multiferroic materials are investigated. In these materials multiple ferroic orders coexist and coupling between them allows tailoring of magnetic properties in an electric field or vice versa. The observation of novel physical phenomena and the promise of new device concepts make these materials attractive. However, due to the incompatibility of the conventional mechanisms that give rise to ferromagnetism and ferroelectricity, strong coupling of sizeable order parameters at room temperature is difficult to obtain in single phase materials. A promising alternative is the use of hybrid material systems, such as thin film heterostructures, where ferromagnetic and ferroelectric compounds are artificially assembled.

In this Thesis I present results on elastically coupled domain walls in ferromagnetic/ferroelectric heterostructures. $BaTiO_3$ substrates exhibiting regular ferroelastic stripe domains are used as the ferroelectric component. Ferromagnetic thin films or multilayers are deposited using Electron Beam Evaporation, Magnetron Sputtering, or Molecular Beam Epitaxy depending on the material. The heterostructures are investigated by Magneto-Optical Kerr Effect (MOKE) microscopy and Scanning Electron Microscopy with Polarisation Analysis (SEMPA). Micromagnetic simulations and analytical modelling complement and expand upon the experimental results.

Strain transfer from the laterally modulated ferroelectric domains in the substrate induces anisotropies in the ferromagnetic thin films via inverse magnetostriction. The abrupt changes in symmetry and orientation of these anisotropies on top of ferroelectric domain boundaries lead to strong pinning of magnetic domain walls. As a result, two types of domain walls - uncharged and charged - can be initialised. They differ in width, energy, and chirality and are tuned by magnetic fields. The remanent magnetisation and switching behaviour of the films are strongly affected by these domain walls when the dimensions of the domains are scaled down to a length comparable to the width of the domain walls. In an electric field, both in-plane and alternating in-plane/out-of-plane magnetic domain patterns can be rewritten. Finally, controlled and reversible electric field induced magnetic domain wall motion is demonstrated. This novel driving mechanism functions without the use of spin polarised currents or magnetic fields. As a result, high density and low power devices based on magnetic domain walls can be envisaged.

Keywords ferromagnetism, ferroelectricity, multiferroic, magnetism, magnetic domains, magnetic domain walls, spintronics, electric field control of magnetism

ISBN (printed) 978-952-60-6816-9 **ISBN (pdf)** 978-952-60-6817-6

ISSN-L 1799-4934 **ISSN (printed)** 1799-4934 **ISSN (pdf)** 1799-4942

Location of publisher Helsinki **Location of printing** Helsinki **Year** 2016

Pages 210 **urn** http://urn.fi/URN:ISBN:978-952-60-6817-6

Preface

> Je n'ai fait celle-ci plus longue que parce que je n'ai pas eu le loisir de la faire plus courte.
>
> Blaise Pascal

You are holding in your hands the first book I have ever published[1]. Although I wrote it in only two or three months[2], it took me almost five years to gain the knowledge, and obtain the results presented here. Despite only my name being featured on the cover, this Thesis required considerable effort and support from others. It would never have been possible without the guidance, support, and knowledge of my supervisor, Prof. Sebastiaan van Dijken. I am grateful to him for giving me the opportunity to join the Nanomagnetism and Spintronics (NanoSpin) group led by him at the Department of Applied Physics in Aalto University. I am indebted to him for patiently answering and discussing all the questions I could come up with.

I inherited my research topic from Dr Tuomas Lahtinen who had been working on the topic for a few years when I joined the NanoSpin group. During the two years that we worked together I learned a lot from him and the work presented in this Thesis would not have been possible without his help. Over time Tuomas became more than a colleague and I have found a good friend in him.

I would like to thank Diego López González and Dr Arianna Casiraghi for their many contributions to my research and Sampo Hämäläinen for his extremely useful computer scripts. I appreciate the feedback from Dr Curtis Wood regarding my language skills. I was fortunate to visit Hamburg University to conduct SEMPA imaging and I would like to thank Prof. Hans Peter Oepen for inviting me and Dr Stefan Rößler for assisting me

[1] It is most likely also the first book I have ever written.

[2] I am glad to not have encountered the problems that have led to the results not published in Reference [1].

with the measurements. I also visited the Tokyo Institute of Technology for MBE growth of samples. I am indebted to Prof. Tomoyasu Taniyama for inviting me and for providing some of the samples that were used for the work presented in this Thesis. Along the way I have had the pleasure to work with Dr Ben Van de Wiele from Ghent University and I am still impressed with his expertise regarding Micromagnetic simulations.
In experimental research, things usually do not go as planned, or as fast as one would hope for. My efforts to pattern my samples have not borne fruit early enough to be included here, but I would like to thank Francisco Freire Fernandez, Mikko Kataja, and especially Dr Qihang Qin for their help. I appreciate the scientific and non-scientific discussions I have had with current and past group members Sampo Inkinen, Sara Pourjamal, Dr Sayani Majumdar, Dr Lide Yao, Dr Godhuli Sinha, and especially Dr Laura Äkäslompolo. I have enjoyed the contributions of Dr Francesco Massel, Dr Jussi Kajala, Dr Antti-Pekka Eskelinen, Dr Miikka Heikkinen, Anne-Maria Visuri, Dr Anton Kuzyk, Dr Robert Moerland, Dr Jildou Baarsma, Dr Arya Dhar, Tomy Cherian, Dr Angel Sanchez Sanchez, and anyone I have forgotten to mention to a pleasant atmosphere in Nanotalo.
Finally, I would like to thank those who have been there for me outside of work (and long before starting this project). This includes of course my family, especially Solange Crüsemann, Alfons Franke, Morgan Franke, Elisabeth Franke, Lucette Denes and Gudrun Reissert. The person that is apart from myself most responsible for my being where I am right now is Mirjami Markkinen. I am lucky to be with her and grateful for her putting up with me even at my most insane moments. I would also like to thank Liisa, Maria, and Minna Markkinen for welcoming me into their family. Finally, I would like to thank Figaro and Stella for their moral support, Lyyti and Taito for chaos and destruction, and Ahti for his stoic calm.
If you, dear reader, have made it this far in my thesis: Why stop now? There are only one hundred pages left and there are some very colourful images later on!

Helsinki, May 2, 2016,

Kévin Franke

Contents

List of Publications

This Thesis consists of an overview and of the following publications which are referred to in the text by their Roman numerals.

I Tuomas H. E. Lahtinen, Kévin J. A. Franke and Sebastiaan van Dijken. Electric-field control of magnetic domain wall motion and local magnetization reversal. *Scientific Reports*, **2,** 258, February 2012.

II Kévin J. A. Franke, Tuomas H. E. Lahtinen and Sebastiaan van Dijken. Field tuning of ferromagnetic domain walls on elastically coupled ferroelectric domain boundaries. *Physical Review B*, **85,** 094423, March 2012.

III Tuomas H. E. Lahtinen, Yasuhiro Shirahata, Lide Yao, Kévin J. A. Franke, Gorige Venkataiah, Tomoyasu Taniyama and Sebastiaan van Dijken. Alternating domains with uniaxial and biaxial magnetic anisotropy in epitaxial Fe films on $BaTiO_3$. *Applied Physics Letters*, **101,** 262405, December 2012.

IV Kévin J. A. Franke, Diego López González, Sampo J. Hämäläinen and Sebastiaan van Dijken. Size Dependence of Domain Pattern Transfer in Multiferroic Heterostructures. *Physical Review Letters*, **112,** 017201, January 2014.

V Kévin J. A. Franke, Ben Van de Wiele, Yasuhiro Shirahata, Sampo J. Hämäläinen, Tomoyasu Taniyama and Sebastiaan van Dijken. Reversible Electric-Field-Driven Magnetic Domain-Wall Motion. *Physical Review X*, **5,** 011010, February 2015.

VI Yasuhiro Shirahata, Ryota Shiina, Diego López González, Kévin J. A. Franke, Aiji Wada, Mitsuru Itoh, Nikolay A. Pertsev, Sebastiaan

van Dijken and Tomoyasu Taniyama. Electric-field switching of perpendicular magnetized multilayers. *NPG Asia Materials*, **7,** e198, July 2015.

VII Arianna Casiraghi, Teresa Rincón Domínguez, Stefan Rössler, Kévin J. A. Franke, Diego López González, Sampo J. Hämäläinen, Robert Frömter, Hans Peter Oepen and Sebastiaan van Dijken. Influence of elastically pinned magnetic domain walls on magnetization reversal in multiferroic heterostructures. *Physical Review B*, **92,** 054406, August 2015.

Author's Contribution

Publication I: "Electric-field control of magnetic domain wall motion and local magnetization reversal"

The author performed and analysed the Micromagnetic simulations and discussed the results with co-authors.

Publication II: "Field tuning of ferromagnetic domain walls on elastically coupled ferroelectric domain boundaries"

The author performed and analysed the Micromagnetic simulations. He obtained Magneto-Optical Kerr Effect (MOKE) microscopy images in a rotating magnetic field, discussed all results with co-authors, and co-wrote the manuscript.

Publication III: "Alternating domains with uniaxial and biaxial magnetic anisotropy in epitaxial Fe films on $BaTiO_3$"

The author performed and analysed the Micromagnetic simulations. He discussed all results with co-authors.

Publication IV: "Size Dependence of Domain Pattern Transfer in Multiferroic Heterostructures"

The author performed and analysed Micromagnetic simulations. He instructed and supervised the second author who performed MOKE microscopy measurements. He derived the analytical model, discussed all results with co-authors, and wrote the first draft of the manuscript.

Publication V: "Reversible Electric-Field-Driven Magnetic Domain-Wall Motion"

The author designed and performed all experiments, analysed the data, discussed the results with co-authors and wrote the first draft of the manuscript.

Publication VI: "Electric-field switching of perpendicular magnetized multilayers"

The author performed the MOKE microscopy measurements, discussed results with co-authors and contributed to the writing of the manuscript.

Publication VII: "Influence of elastically pinned magnetic domain walls on magnetization reversal in multiferroic heterostructures"

The author performed preliminary experiments, contributed to the SEMPA measurements and discussed the results and their analysis with the co-authors.

Other Publications

The author has also contributed to the following publications that are not included in this Thesis.

A Ben Van de Wiele, Lasse Laurson, Kévin J. A. Franke and Sebastiaan van Dijken. Electric field driven magnetic domain wall motion in ferromagnetic-ferroelectric heterostructures. *Applied Physics Letters*, **104,** 012401, January 2014.

B Florian Brandl, Kévin J. A. Franke, Tuomas H. E. Lahtinen, Sebastiaan van Dijken and Dirk Grundler. Spin waves in CoFeB on ferroelectric domains combining spin mechanics and magnonics. *Solid State Communications*, **198,** 13, November 2014.

C Ben Van de Wiele, Jonathan Leliaert, Kévin J. A. Franke and Sebastiaan van Dijken. Electric-field-driven dynamics of magnetic domain walls in magnetic nanowires patterned on ferroelectric domains. *New Journal of Physics*, **18,** 033027, March 2016.

1. Introduction

> The behaviour of large and complex aggregates of elementary particles, it turns out, is not to be understood in terms of a simple extrapolation of the properties of a few particles. Instead, at each level of complexity entirely new properties appear.
>
> Philip Warren Anderson

Present information technologies rely on the motion of charge for data storage and logic operations. Currents allow the writing of information in magnetism based data storage via their Oersted field, while semiconductor based logic technologies rely directly on the flow of currents. Significant effort is spent on scaling devices to smaller dimensions in order to increase storage densities and device speeds. Unfortunately, further downscaling aggravates the issue of heating generated by the flow of electrons. The associated energy dissipation has become the main hindrance for technological improvements. New concepts and physical phenomena thus have to be exploited in order to sustain the miniaturisation and improvements in efficiency of microelectronics.

Spintronics – as opposed to conventional electronics – utilises the spin of electrons, or their associated magnetic moment, instead of their charge to perform logic operations, store information, or sense magnetic fields [2, 3]. Fast switching, high storage densities, and non-volatility make magnetism based technologies advantageous. Examples of commercially available devices include magnetic read heads in Hard Disc Drives (HDD) that are based on Giant Magneto-Resistance (GMR) and Magnetic Random Access Memory (MRAM). Another proposed and intensively investigated data storage technology is the so-called Racetrack Memory [4–6] that relies on the motion of magnetic domain walls. Nonetheless, present spintronic devices rely on magnetic switching or magnetic domain wall

motion induced by an external magnetic field or electric currents. Both mechanisms have disadvantages: The generation of magnetic fields relies on currents and requires bulky components. The Spin Transfer Torque (STT) mechanism also requires high current densities that lead to undesirable heating and substantial power dissipation.

Control of magnetism with electric fields (i.e. voltages) would not require the flow of electric charges and may thus reduce power consumption by several orders of magnitude [7]. It therefore constitutes a promising low power alternative to existing and proposed memory and logic technologies. One approach to electric field control of magnetism relies on magnetoelectric multiferroics. These materials exhibit both ferromagnetism and ferroelectricity and allow for the control of magnetisation using electric fields instead of magnetic fields or currents. Unfortunately, multiferroic materials are rare and show only weak coupling effects, usually well below room temperature. Attractive alternatives are hybrid or composite material systems, in which ferromagnetic and ferroelectric compounds are artificially assembled, e.g., in thin-film heterostructures. In these systems, the coupling between the two ferroic phases is mediated via strain, charge modulation, or other electronic effects at the interfaces. Multiferroic heterostructures are appealing not only because they exhibit the properties of both parent compounds, but also because interactions between magnetic and electric polarisations can lead to entirely new functionalities. For instance, coupling could in principle permit data to be written electrically and stored magnetically. This would allow for new high speed information technologies with reduced power consumption.

In this Thesis, I present results on elastically coupled domain walls in ferromagnetic/ferroelectric heterostructures. $BaTiO_3$ substrates exhibiting regular ferroelastic stripe domains are used as the ferroelectric component. At room temperature the ferroelectric polarisation is associated with a tetragonal lattice elongation. Relaxation of stress leads to the formation of ferroelastic stripe patterns, where the lattice elongation and correlated polarisation change by 90° between domains. When this lattice elongation rotates between in-plane domains, so-called a_1–a_2 domain patterns provide a 1.1% modulation of lateral strain. Thin films of $Co_{60}Fe_{40}$ or $Co_{40}Fe_{40}B_{20}$ are deposited by Electron Beam Evaporation or Magnetron Sputtering, respectively. Strain transfer at the interface and inverse magnetostriction in the ferromagnetic films induce uniaxial anisotropies that are correlated with the orientation of the ferroelectric polarisation. Con-

sequently, imprinting of regular ferroelectric domains into continuous ferromagnetic films is realised.

Using Magneto-Optical Kerr Effect (MOKE) Microscopy and Scanning Electron Microscopy with Polarisation Analysis (SEMPA), I demonstrate that magnetic domain walls are strongly pinned by the abrupt changes in the anisotropy direction. Ergo, ferromagnetic and ferroelectric domain walls are coupled. Moreover, two types of domain walls – magnetically uncharged and charged – can be initialised. They differ in width, energy, and chirality, and can be tuned by magnetic fields. Hysteretic switching between both wall types is demonstrated in a rotating magnetic field.

As the width of domains is reduced, magnetic domain walls are brought closer together and start to interact. This has a significant impact on the magnetic properties of the heterostructures, both at remanence and in applied magnetic fields. Combining Micromagnetic simulations and analytical modelling, I show that when the widths of domains and domain walls become comparable, domain pattern transfer breaks down and correlations between the ferroelectric substrate and ferromagnetic thin film are lost. As two types of domain walls with distinct widths can be initialised, two scaling regimes of pattern transfer may be obtained. Recurrent switching between both regimes in a rotating magnetic field allows for the writing and erasure of magnetic domains. Results on $Co_{40}Fe_{40}B_{20}/BaTiO_3$ heterostructures confirm the theoretical predictions.

An electric field applied across the substrate of a $Co_{60}Fe_{40}/BaTiO_3$ heterostructure switches the ferroelectric polarisation from in-plane a_1–a_2 domains to fully out-of-plane. In the magnetic film, new compressive strains are imposed along the direction in which the lattice was initially elongated. Hence, local anisotropy directions rotate throughout the film, preserving the domain pattern. After removal of the electric field, $BaTiO_3$ relaxes into an a–c domain pattern where the polarisation alternates between in-plane and out-of-plane. As a result, new strains are imposed on the ferromagnetic film and the domain pattern is rewritten.

In heterostructures with a Ni/Cu multilayer grown onto an in-plane polarised $BaTiO_3$ substrate by Molecular Beam Epitaxy (MBE), the magnetisation points out-of-plane in the as-deposited state. The perpendicular magnetic anisotropy is a consequence of the strain that develops due to lattice matching at the Ni/Cu interfaces. Again, the polarisation of the substrate can be switched out-of-plane electrically. The resulting strains switch the magnetisation of the ferromagnetic multilayer into the film

plane. At electric remanence an a–c domain pattern in the substrate is imprinted into the ferromagnetic multilayer as alternating in-plane-out-of-plane magnetised domains. Electric fields allow for the reversible control of these domains.

As a highlight, reversible electric field driven magnetic domain wall motion is demonstrated for epitaxial Fe films grown by MBE onto a $BaTiO_3$ substrate exhibiting a–c domains. The mechanism is also based on pinning of magnetic domain walls onto their ferroelectric counterpart. The induced motion is fully controlled and reversible, and the velocity of the domain walls increases exponentially as a function of out-of-plane electric field. This novel driving mechanism functions without the concurrent use of electric currents or magnetic fields. This proof of principle study opens up the possibility to devise low power technologies based on the motion of magnetic domain walls. Micromagnetic simulations show that despite the moderate domain wall angle induced by domain pattern transfer, near to 180° domain walls can be initialised in magnetic nanowires due to competing shape anisotropy. Furthermore, fast domain wall motion can be sustained up to several hundreds of m/s.

The remainder of the Thesis is organised as follows: In Chapter 2, I introduce ferromagnetism in the framework of Micromagnetism and review the pertinent literature. Ferroelectricity is presented in Chapter 3, while the coexistence and coupling of ferroic orders is discussed in Chapter 4. In Chapter 5, I present the methods used. They include Electron Beam Evaporation, Molecular Beam Epitaxy, and Magnetron Sputtering to deposit thin films. The heterostructures are characterised using Magneto-Optical Kerr Effect (MOKE) Microscopy and Scanning Electron Microscopy with Polarisation Analysis (SEMPA). The experimental results are complemented and expanded upon with Micromagnetic simulations and analytical modelling. The results are presented and discussed in Chapter 6. I conclude in Chapter 7 with a short summary.

2. Ferromagnetism

> The existence of this spontaneous magnetisation is explained by the Weiss "molecular field" postulate, amended quantum-mechanically by Heisenberg; the amendment replaces the mysterious molecular field by exchange forces, which are less mysterious or more so according to one's feeling towards quantum mechanics.
>
> William Fuller Brown

Ferromagnetic materials undergo a phase transition from a high temperature phase that does not exhibit a macroscopic magnetic moment to a low temperature phase displaying a spontaneous magnetisation that can be switched by the application of an external magnetic field. Unlike for paramagnets ($\chi = M/H > 0$) and diamagnets ($\chi < 0$), the susceptibility χ of a ferromagnet is not constant as a function of magnetic field. On a macroscopic level, ferromagnetic materials are characterised by a hysteresis curve (cf. Figure 2.1). It displays the macroscopic magnetisation M as a function – and along the direction – of an applied magnetic field H. In a large magnetic field the magnetisation is fully aligned with the external field and the saturation magnetisation M_S is measured. The field required to reach saturation is called the saturation field H_S. As the magnetic field is reduced to zero, the remanent magnetisation M_R is observed. Finally, the coercive field H_C is the field that needs to be applied opposite the saturating field in order to reduce the magnetisation to zero. This does not mean that the microscopic magnetic moments that make up the macroscopic magnetisation vanish, but that the average of their projection onto the field direction is zero. The changes in magnetisation observed in the hysteresis curve can be caused by two independent mechanisms: Rotation of the direction of magnetic moments or creation and growth of magnetic domains [8–12].

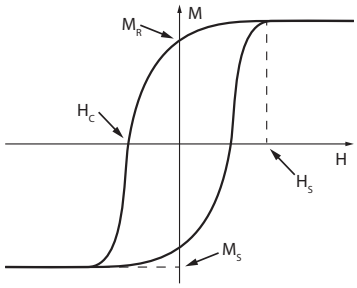

Figure 2.1. Schematic of a ferromagnetic hysteresis curve: When the magnitude of the magnetic field is larger than the saturation field H_S, the magnetisation is fully aligned with the field and reaches the saturation magnetisation M_S. The remanent magnetisation M_R is measured in zero magnetic field, while the coercive field H_C needs to be applied in order to bring the average macroscopic magnetisation down to zero.

Origin of Magnetic Moments

Microscopically the magnetic moment originates from the spin and orbital angular momenta of electrons. In a naive classical image of the atom, an electron can be modelled as orbiting the nucleus on a circular orbit. This model is equivalent to a tiny current loop which can be shown to correspond to a classical magnetic moment [13]:

$$\overrightarrow{m} = -\frac{e\mu_0}{2m_e}\overrightarrow{l}, \tag{2.1}$$

where e is the elementary charge, μ_0 is the permeability of free space, m_e is the electron mass, and $\overrightarrow{l}$ is the classical angular momentum of the orbiting electron. The minus sign is courtesy of Ben Franklin and the negative charge of the electron. As a result, the magnetic moment of the electron is anti-parallel to its angular momentum.

Of course the electron is not on a simple circular orbit around the nucleus of the atom. Quantum mechanically the electron is described by an angular wave function with its angular moment quantised in units of the Bohr magneton [14]:

$$\mu_B = \frac{e\mu_0\hbar}{2m_e}. \tag{2.2}$$

Moreover, only the expectation value $\langle\overrightarrow{l_z}\rangle = \hbar l_z$ of the angular momentum operator along the quantisation axis (here: z-direction) can be observed.

In addition to the orbital angular momentum the electron itself exhibits an intrinsic angular momentum known as spin. Despite being associated with a spin quantum number of only $s = \hbar/2$ with expectation values $\langle\overrightarrow{s_z}\rangle = \hbar l_z/2$, it generates a full Bohr magneton. The total magnetic moment of the electron is then given by the sum of the orbital and spin

magnetic moments as [13]:

$$\langle m_{z,tot} \rangle = -\frac{\mu_B}{\hbar} \left(\langle l_z \rangle + g_s \langle s_z \rangle \right), \tag{2.3}$$

where the so-called g-factor $g_\mathrm{s} \approx 2$. Due to the much larger mass of the proton when compared to that of the electron (by three orders of magnitude) nuclear magnetic moments do not contribute significantly to the magnetisation of an atom.

The spin and orbital angular momenta are not completely independent. The so-called spin–orbit coupling (SOI) leads to a correction in the total angular momentum of the electron. While this correction is only small, it is relevant in magnetic materials as will be shown later. The interaction can be intuitively understood in the classical picture introduced above: The angular momentum is viewed as arising from a circular motion of the electron around the nucleus. Switching into a frame where the electron is at rest, the nucleus is considered as rotating around the electron. The current loop thus created gives rise to a magnetic field that interacts with the spin magnetic moment of the electron. Thus, the spin of the electron is coupled to its orbital motion [13].

Most atoms contain more than one electron. In fully filled electron shells the various contributions to the angular momentum cancel each other out resulting in zero total angular momentum J. The empirical Hund's rules can be used in order to determine the electronic ground state in partially filled shells [11, 15]:

1. The total atomic spin S is maximised without violating the Pauli exclusion principle. This means that, as far as possible, electrons will occupy states with parallel spins.
2. Maintaining consistency with the obtained value of S, the total atomic orbital angular momentum L is maximised.
3. The total angular momentum J equals $\mathrm{L} + \mathrm{S}$ if the shell is more than half full and J equals $\mathrm{L} - \mathrm{S}$ if the shell is less than half full.

The third rule is a consequence of spin–orbit coupling. The second rule is a consequence of Coulomb repulsion: Electrons orbiting in the same direction meet less often than if they were orbiting in opposite directions. Hund's first rule is also a consequence of the Coulomb interaction: In order to minimise the electrostatic energy, electrons are kept as far apart from each other as possible. This is achieved by having the electrons occupy different orbitals. The corresponding wave function is then antisym-

metric in space and must therefore be symmetric in spin. The first rule is hence a consequence of an intra-atomic exchange interaction.

Magnetic Order

In most cases the magnetic moments of the atoms are not – or only weakly – coupled. Thermal agitation causes spins to point in random directions in the absence of an applied magnetic field. When applying an external magnetic field the spins tend to align, although their orientation is still randomised by the effect of temperature. This leads to a paramagnetic response of the material. This model, known as the Langevin-model [16], requires localised magnetic moments. This is not the case in metals where the Pauli paramagnetism model [17] needs to be considered. For simplicity, I will first consider localised moments only: In order for ferromagnetism to arise, the inter-atomic exchange interaction needs to align neighbouring spins. Consequently, magnetic moments are aligned in the same direction at zero applied magnetic field. Neighbouring spins can also couple in a different way leading to other forms of magnetic order: In antiferromagnets adjacent magnetic moments point in opposite directions leading to zero net magnetic moment. When the two antiferromagnetically coupled sublattices have moments of different magnitude the material exhibits a net magnetic moment and is called ferrimagnetic. Finally, neighbouring spins can be orientated at an angle leading to helimagnetism. In macroscopic measurements helimagnets and antiferromagnets cannot be distinguished from paramagnets while ferrimagnets can be mistaken for ferromagnets. As mentioned at the beginning of this Chapter, the randomising effect of temperature destroys magnetic order above a transition temperature known as the Curie temperature T_C for ferromagnets and Néel temperature T_N for antiferromagnets. Above this temperature materials are paramagnetic [11, 18, 19].

Micromagnetism

Depending on the dimensions that are considered, ferromagnets can be described by different theoretical models [20]. Macroscopic hysteresis curves and elementary magnetic moments on the atomic level have already been introduced. In this Thesis magnetic materials are considered on a length scale from a few nm to several tens of μm. The theory that is most suited for describing magnetic properties at this level is Micromagnetism [21]. The approach of Micromagnetism is to describe the magnetic microstructure of ordered materials in a continuum approximation that ignores the atomic nature of matter [22]: As the magnitude of $\overrightarrow{M}$ is

uniform in a homogeneous specimen its value is taken as the saturation magnetisation M_S. The direction of $\overrightarrow{M}$ on the other hand is known experimentally to vary spatially and is therefore approximated as a continuous function of position $\overrightarrow{r}$. The local orientation of the magnetisation is then calculated similarly to the approach taken in Domain Theory [8,23], i.e. by minimising the total energy:

$$E_{tot}(\overrightarrow{M}(\overrightarrow{r}), H_{ext}) = \int_V \left(e_{ex}(\overrightarrow{r}) + e_h(\overrightarrow{r}) + e_a(\overrightarrow{r})\right) d\overrightarrow{r} + \int_V \int_{V'} \left(e_{ms}(\overrightarrow{r}, \overrightarrow{r}')+\right) d\overrightarrow{r}\,\overrightarrow{r}', \quad (2.4)$$

using variational calculus. The first contribution is the exchange energy density e_{ex} that tends to keep neighbouring spins parallel. The Zeeman energy density e_h describes the energy cost for misaligning the magnetisation with the external magnetic field H_{ext}. The magnetostatic energy density e_{ms} is a consequence of the dipole–dipole interaction between magnetic moments and is the only non-local energy contribution. It thus cannot be calculated in a simple integration as it depends on the distribution of magnetic moments. Finally, the anisotropy energy density e_a describes the preference of the magnetisation to lie along certain directions in the sample [19].

Alternatively, the energy minimum can be calculated by requiring that in thermodynamic equilibrium the magnetisation is oriented in a way such that the torque:

$$\overrightarrow{L} = \overrightarrow{M} \times \overrightarrow{H_{eff}} \quad (2.5)$$

on each moment is zero. The different energy contributions then need to be expressed in terms of a magnetic field and summed to yield the effective field $\overrightarrow{H_{eff}}$. Tracing the dissipative process that leads to thermodynamic equilibrium allows for the determination of magnetisation dynamics [21]. In the following Sections, I introduce the various energy contributions and the equation that determines magnetisation dynamics. I will then show how the energy contributions lead to the formation of domains and domain walls and how they affect magnetisation reversal, i.e. the shape of the hysteresis curve.

2.1 Exchange Energy

In materials, ferromagnetism originates from the short range exchange interaction. It causes parallel magnetic moments to be energetically more favourable than spins with opposite orientation. Two – mutually exclusive – phenomenological models of exchange are successful in explaining the origin and effect of exchange in solids: The localised moment model and the band model [9–11, 19]. In the former, electrons remain mainly localised around the atom and there is only a small overlap with the wave function of electrons from neighbouring atoms. This model is described by the Heisenberg Hamiltonian [24], and exchange is, as for intra-atomic exchange, a consequence of the antisymmetric electron wave function and minimisation of the Coulomb energy. The band model of ferromagnetism [25, 26] explains exchange in metals, where electrons from many atoms share common bands. Additionally, other models of exchange exist that are more appropriate for specific ferromagnetic material classes: They include the RKKY interaction, superexchange, and double exchange [27].

2.1.1 Heisenberg Hamiltonian

In the Heisenberg model of ferromagnetism the electronic magnetic moments are mainly localised around their respective atoms. A small overlap of the electronic wave functions is necessary for the Pauli exclusion principle to apply. As a result, there is a correlation between the spin of the electrons which in turn leads to a magnetically ordered state. When considering only interactions between nearest neighbours, the exchange energy is described by the Heisenberg Hamiltonian [24]:

$$H = -J \sum_{i<j} \overrightarrow{S}_i \cdot \overrightarrow{S}_j, \tag{2.6}$$

where the exchange integral J between total atomic moments (atomic spins) $\overrightarrow{S}_i$ is taken to be identical for all next-neighbour pairs [11, 19]. While the model provides a relatively simple model for exchange it is, unfortunately, not very realistic. In many cases, such as in the magnetic 3d transition metals (Fe, Co, Ni), the electrons that contribute to the magnetic moment are relatively free to move. Moreover, if the electrons were fully localised around the atoms, the atomic magnetic moments should be integer multiples of the Bohr magneton μ_B (cf. Equation 2.3), which is not the case. They are 2.2 μ_B for Fe, 1.7 μ_B for Co and 0.6 μ_B for Ni [19].

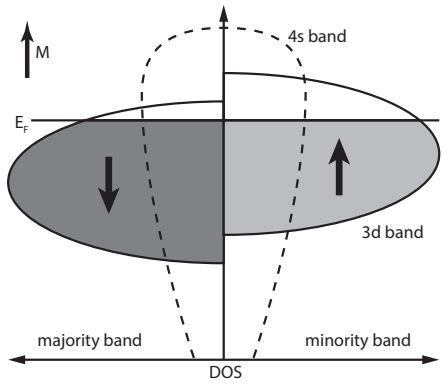

Figure 2.2. Sketch of the spin-split 3d and unsplit 4s density of states (DOS) in the first row transition metals according to the band model of ferromagnetism: Electron states are filled up to the Fermi energy E_F (grey shading). The band containing the larger amount of electrons is called majority band while the minority band is filled with less electrons. In this example the majority band is filled with spin down electrons and the magnetisation thus points up [13].

2.1.2 Band Model of Ferromagnetism

To explain ferromagnetism in metals a band theory of ferromagnetism [25, 26] is needed. I will concentrate on the magnetic 3d transition metals that are characterised by unequally filled spin-split 3d bands and unsplit 4s bands. While the 4s electrons are mainly de-localised and form a broad s-band of relatively free electrons, the 3d electrons form a more localised, narrow and high density of states (DOS) d-band [13, 19]. The 3d electrons thus "spend more time" close to the ion core and are subjected to the intra-atomic exchange interaction favouring parallel spins. The electron's magnetic moment is mostly due to its spin, while orbital moments contribute only a limited amount. In order for spins to align parallel, band states cannot be filled equally with up and down spins any more and the electron band is spin-split as sketched in Figure 2.2. As a result of the exchange interaction, the minority band with spin-up electrons is shifted up in energy relative to the majority band containing spin-down electrons. Consequently, electrons from the minority band need to be transferred to band states of higher energy, since band states with the same energy are already occupied in the majority band. This increase in band energy opposes the exchange interaction and their competition determines the magnitude of the band splitting. If both the exchange energy and the DOS at the Fermi level (E_F) are large enough (this can be formulated quantitatively as the Stoner criterion), the resulting spin imbalance leads to a net magnetic moment. As can be easily seen, the resulting net magnetic moment is generally not an integer multiple of the Bohr magneton

μ_B [11, 13, 19]. The model also explains why some metals are ferromagnetic while others are not: For Fe, Co and Ni, E_F lies in the 3d band, while e.g. in Cu it lies above the 3d band [10].

2.1.3 Exchange Stiffness

Although the band model is successful in explaining the origin of ferromagnetism in metals, it has the major drawback of not being able to deal with spatial variations in the magnetisation. Despite not describing the underlying physics correctly, the Heisenberg Hamiltonian is hence more suited for calculating the exchange energy of a magnetisation configuration. In order to be able to use it in Micromagnetism a continuum approximation is made. The Heisenberg Hamiltonian (Equation 2.6) is isotropic, i.e. if we view the spins as classical vectors it only depends on the angle between spins. It can therefore be rewritten as [8]:

$$H = -J \sum_{i<j} S^2 cos\psi_{ij}, \tag{2.7}$$

where ψ_{ij} is the angle between adjacent spins $\overrightarrow{S}_i$ and $\overrightarrow{S}_j$. Making the reasonable assumption that the angle between neighbouring spins is small, a Taylor expansion eventually yields:

$$e_{ex} = A(\nabla \overrightarrow{m})^2, \tag{2.8}$$

where $\overrightarrow{m} = \overrightarrow{M}/M_S$ is the reduced magnetisation (i.e. its unit vector) and A is the exchange stiffness that can be determined experimentally. Equation 2.8 quantifies the energy penalty associated with variations in the magnetisation direction imposed by the exchange interaction [8, 14, 20].

2.2 Zeeman Energy

The requirement of zero torque (cf. Equation 2.5) forces magnetic moments to align parallel to an externally applied magnetic field $\overrightarrow{H}$ [11]. The corresponding energy – called the Zeeman energy – can be derived in a classical picture as follows: In analogy to classical electrostatics the magnetic dipole $\overrightarrow{m} = p\,\overrightarrow{d}$ is viewed as composed of a positive magnetic charge (+p) and negative magnetic charge (−p) separated by a distance d as shown in Figure 2.3. These charges do not actually exist, but they will prove to be a very useful concept later on. The magnetic field $\overrightarrow{H}$ exerts

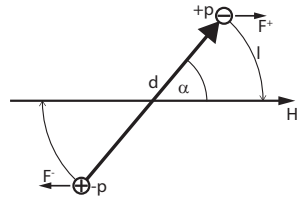

Figure 2.3. A magnetic dipole $m = p\,d$ at an angle α with an applied magnetic field H minimises its energy by turning towards the field direction because of the forces $F^{\pm}$ on the (virtual) magnetic charges $\pm$q, while the net force is zero [13].

forces $\overrightarrow{F^+} = +p\overrightarrow{H}$ and $\overrightarrow{F^-} = -p\overrightarrow{H}$ on the positive and negative charge, respectively. On average the forces cancel out, i.e. the magnetic dipole does not move, but it is pushed to align with the magnetic field. Using the definitions given in Figure 2.3 the Zeeman energy is derived as:

$$E = 2\,\mu_0\,p \int \overrightarrow{H} \cdot d\,\overrightarrow{l} = \mu_0\,p\,d\,H \int cos\,\alpha\,d\alpha = -\mu_0\,\overrightarrow{m} \cdot \overrightarrow{H}. \tag{2.9}$$

For a uniformly magnetised sample the Zeeman energy density can thus be written as:

$$e_h = -\mu_0\,M_S\,H\,cos(\theta - \phi), \tag{2.10}$$

where $(\theta - \phi) = \alpha$. The definitions of θ and ϕ are given in Section 2.7 [13].

2.3 Magnetostatic Energy

Besides an externally applied field, a magnetic sample is affected by the magnetic field created by its own magnetisation. The classical dipole–dipole interaction between magnetic moments is at the origin of this magnetostatic energy. It is the only energy that is non-local and cannot be written as a simple integral over an energy density. It is instructive to start by defining the scalar potential U via the equation:

$$\overrightarrow{H} = -\nabla U \tag{2.11}$$

which is the most general solution to the Maxwell equation $\nabla \times \overrightarrow{H} = 0$. With the boundary conditions appropriate for a finite ferromagnetic material, the solution to Equation 2.11 is given by:

$$U\,(\overrightarrow{r}) = \frac{1}{4\pi\mu_0}\left(-\int \frac{\nabla \cdot \overrightarrow{M}(\overrightarrow{r\prime})}{\mid \overrightarrow{r} - \overrightarrow{r\prime} \mid} dV\prime + \int \frac{\overrightarrow{n} \cdot \overrightarrow{M}(\overrightarrow{r\prime})}{\mid \overrightarrow{r} - \overrightarrow{r\prime} \mid} dS\prime\right), \tag{2.12}$$

where the first integral is over the volume and the second integral over the surface of the ferromagnetic sample. $\overrightarrow{n}$ is the outward normal to the sample surface. The form of the magnetostatic potential resembles the electrostatic potential. The first integral can be interpreted as representing a reduced volume charge density :

$$\rho = -\nabla \overrightarrow{m}, \tag{2.13}$$

while the second integral can be viewed as the potential of a reduced surface charge density:

$$\sigma = \overrightarrow{n} \cdot \overrightarrow{m}, \tag{2.14}$$

where $\overrightarrow{m} = \overrightarrow{M}/M_S$ is again the reduced magnetisation. Substituting these charge densities into Equation 2.12 and integrating then yields the magnetostatic energy

$$E_{ms} = \frac{M_S}{2}\left(\int \rho(\overrightarrow{r})U(\overrightarrow{r})dV + \int \sigma(\overrightarrow{r})U(\overrightarrow{r})dS\right), \tag{2.15}$$

associated with a given magnetic charge distribution. These charges are of course virtual. "However, it is never necessary for any *useful* mathematical tool to have a physical meaning. There is no real physical charge, but the mathematical identity between these integrals and those which involve a charge makes it possible to use the knowledge about a real charge to guess the qualitative properties of the magnetostatic potential" [28]. The positive and negative magnetic charges act as sources and sinks of the magnetostatic field. Magnetic charges accumulate on the surface of a body when it has a magnetisation component pointing perpendicular to its surface. An extreme example would be a homogeneously magnetised sample as shown for instance in Figure 2.4 (on Page 17). The charges create a field outside the sample known as the stray field. They also generate the demagnetisation field that passes through the body and opposes the magnetisation that is at their origin.

The magnetostatic potential falls off as $1/r$, meaning that the dipole–dipole interaction acts over a relatively long range. Conversely, the exchange interaction introduced in Section 2.1 acts only over a very short length scale. It is however much stronger than the magnetostatic energy. When the exchange energy is expressed as an effective molecular field [29, 30], it is seen to be larger by about 4 orders of magnitude than the magnetostatic field created by the magnetic moments of a ferromag-

netic material [8]. Exchange thus determines the properties of ferromagnets on a short length scale while the magnetostatic energy dominates on a long length scale [19, 20, 28].

2.4 Anisotropy Energy

It is an experimental fact that the magnetisation has a tendency to be oriented along one or several directions in a ferromagnet. These directions are called axes of easy magnetisation, or easy axes. The directions along which it is the most difficult to orient the magnetisation are called hard axes. By definition, the magnetic anisotropy energy is needed to reorient the magnetisation from the easy to the hard axis. Without the existence of magnetic anisotropy, 2-dimensional samples, i.e. thin films, could not order ferromagnetically [31] and 3-dimensional objects would not exhibit a macroscopic magnetisation despite the presence of the exchange interaction [28]. Magnetic anisotropy can have different origins, such as the magnetostatic energy that results in a dependence on the shape of the sample. In a crystal the combined effect of the crystal field and the spin–orbit coupling leads to magnetocrystalline anisotropy. The magnetoelastic anisotropy relates the anisotropy to strain. The broken symmetry at the surface of a ferromagnet or at the interface between materials leads to surface and interface anisotropies. Finally, the exchange interaction between an antiferromagnetic and a ferromagnetic layer can lead to exchange anisotropy. The related exchange bias is not strictly speaking an anisotropy but will also be introduced here. Since "the ability to reduce everything to simple fundamental laws does not imply the ability to start from those laws and reconstruct the universe" [32] it is usually not possible to determine the anisotropy energy from first principles. I will therefore first introduce the phenomenological energy expressions commonly used before giving an explanation of their origin [8, 13, 33].

Uniaxial Anisotropy

The form of the anisotropy must follow the symmetry of the mechanisms that cause it. Series expansions in terms of spherical harmonics are used. As anisotropies define easy and hard axes of magnetisation, only terms that are invariant when the magnetisation is inverted are included. If only one anisotropy axis is present, the uniaxial anisotropy energy density

is given by [8]:

$$e_u = \sum_n K_n \, sin^{2n}\phi, \tag{2.16}$$

with anisotropy constants K_n and ϕ the angle between the anisotropy axis and the magnetisation. It is often sufficient to include only the first term of the expansion in Equation 2.16 and, in order to avoid confusion later on, the first anisotropy constant is here renamed $K_1 = K_u$. $K_u > 0$ describes a uniaxial anisotropy with energy minima at $\phi = 0$ and $\phi = \pi$. In the case where K_u is negative, the uniaxial anisotropy axis is a hard axis with a perpendicular easy plane [13, 14, 20].

Cubic Anisotropy

If the magnetic anisotropy is cubic, the anisotropy energy density in terms of the directional cosines m_i of the reduced magnetisation is given by [8]:

$$e_c = K_1(m_x^2 m_y^2 + m_y^2 m_z^2 + m_z^2 m_y^2) + K_2 m_x^2 m_y^2 m_z^2, \tag{2.17}$$

where only the first two terms that are not constant have been included. In two dimensions this expression can be simplified as [V]:

$$e_c = K_c sin^2\left(2\psi\right), \tag{2.18}$$

where K_c is the cubic anisotropy constant and ψ is the angle between the magnetisation and one of the anisotropy axes (the other one is perpendicular to it) [28].

2.4.1 Shape Anisotropy

The magnetostatic energy described in Section 2.3 introduces an anisotropy that depends on the shape of a ferromagnetic sample. The examples given here can actually be solved analytically, but the shape anisotropy can be understood intuitively using the concept of magnetic charges. I first consider a ferromagnetic ellipsoid that is uniformly magnetised. This is the case for a small enough particle. Magnetic charges accumulate on the surface of the ellipsoid as illustrated in Figure 2.4 (a) & (b) for configurations where the magnetisation is pointing along the principal axes of the ellipsoid. In both cases, the charge density is the same, but when the magnetisation lies along the short axis (Figure 2.4(a)) the charge is spread over a larger area than when the magnetisation lies along the long axis of the ellipsoid (Figure 2.4(b)). The latter is therefore

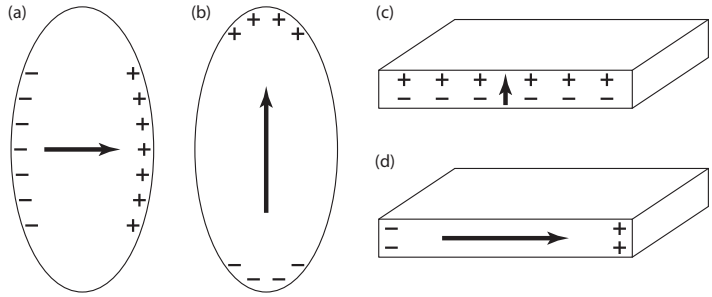

Figure 2.4. Examples of shape anisotropy illustrated with virtual magnetic charges: The magnetostatic energy of an ellipsoid uniformly magnetised along its short axis (a) is higher than if magnetised along its long axis (b). Similarly, a thin film magnetised perpendicular to its plane (c) has a higher energy than one magnetised in-plane (d).

energetically favourable and the long axis constitutes an easy anisotropy direction. The same argument can be used when considering a uniformly magnetised thin film: If the magnetisation was to point out of the film plane (Figure 2.4(c)) the magnetic charges would be spread over a much larger area than if the magnetisation would lie in the film plane (Figure 2.4(d)). In the extreme case of an infinite film[1], the magnetostatic energy can be expressed as:

$$e_{ms} = 2\pi(\overrightarrow{n} \cdot \overrightarrow{M})^2 = 2\pi M_s^2 cos^2\chi, \tag{2.19}$$

where the magnetisation makes an angle χ with the film normal $\overrightarrow{n}$. Accordingly, the magnetisation of thin films usually lies in the film plane. Similarly, magnetic nanowires are characterised by a uniaxial anisotropy along the wire axis. In Micromagnetism the shape anisotropy is not explicitly introduced, as it is a consequence of the magnetostatic energy [28, 33].

2.4.2 Magnetocrystalline Anisotropy

In bulk materials, the magnetocrystalline anisotropy that couples the direction of magnetisation to the crystal axes generally dominates. This anisotropy is due to crystalline electric fields and the spin–orbit coupling. In an atom an electron is subjected to a spherically symmetric potential that determines the orbital motion of the electron as described in the introduction to this Chapter. The electron spin will thus point along any direction with the same probability. When the atom is embedded in the

[1]This is a good approximation when the thickness of the film is orders of magnitude smaller than the lateral dimensions.

crystal lattice of a metal, the electrostatic potential felt by the electron is different: The ions of the lattice create an inhomogeneous potential. The orbital angular momentum of the electron is therefore not free to orient in any direction any more. Although the magnitude of the orbital angular momentum is greatly reduced (quenched) in metals – only approximately 5% of the magnetisation of Iron (Fe) is of orbital origin – gradients in the electrostatic crystalline potential will give rise to a spin–orbit coupling [14]. As it is energetically favourable for the orbital angular momentum to be oriented along certain axes of the crystal, the spin of the electrons will also exhibit this preferential orientation. In order for a metal to exhibit magnetocrystalline anisotropy it is thus necessary for the magnetisation to "feel" the asymmetric crystal field through the action of the spin–orbit interaction. The magnetocrystalline anisotropy energy therefore depends on the symmetry of the crystal and on the relative orientation of the crystal axes and the magnetisation. It should be noted that the location of the Fermi level in the spin-split band structure (cf. Section 2.1.2) is crucial for the symmetry of the crystalline anisotropy and for the sign and magnitude of the anisotropy constants. In the magnetic 3d transition metals the magnetocrystalline anisotropy manifests itself as follows: Both BCC Iron (Fe) and FCC Nickel (Ni) exhibit cubic anisotropy. For Fe the easy axes are oriented along the $[100]$ directions of the crystal while the $[111]$ diagonals are the hard axes. For Ni the roles of the axes are inverted. Hexagonal Cobalt (Co) exhibits a uniaxial anisotropy with the easy direction along the c-axis. Polycrystalline ferromagnets exhibit no – or only small – net magnetocrystalline anisotropy as the contributions from randomly oriented grains cancel out [8, 14, 19, 33–35].

2.4.3 Bond Orientation Anisotropy

Amorphous materials do not have a crystalline lattice nor do they exhibit an associated magnetocrystalline anisotropy. However, it is an experimental fact that amorphous ferromagnets display anisotropy. It has been demonstrated that for thin films, oblique deposition or the simultaneous application of a magnetic field during growth can lead to significant uniaxial anisotropies. The most frequently suggested mechanism for this phenomenon is bond orientation anisotropy. It refers to a distribution in the orientation of nearest neighbour atomic bonds that can be spatially anisotropic. It explains how amorphous thin films can exhibit a magnetic anisotropy [36–40].

2.4.4 Magnetoelastic Anisotropy

Magnetostriction describes the phenomenon that macroscopically a ferromagnet usually exerts a stress on its surroundings when the orientation of the magnetisation is changed. If the material is not constrained it will thus change its physical dimensions. Microscopically this fact is due to a change in the crystal lattice [41, 42]. The converse effect – i.e. a change in the orientation of the magnetisation due to an applied stress – forms the basis of magnetoelastic anisotropy. It can be shown that "the effect of ... stress is to introduce an additional term to the anisotropy energy superimposed on the normal crystal energy" [41]. In crystalline materials the magnetoelastic anisotropy is closely related to the magnetocrystalline anisotropy. As seen in Section 2.4.2, the magnetisation is coupled to the lattice via spin–orbit coupling and the crystal field. Stress alters the distance between ions and therefore their electric potential and the overlap in wave function between them. The bond orientation anisotropy introduced in the previous Section accounts for magnetoelastic anisotropy in amorphous ferromagnets as the orientation and length of bonds clearly changes when a materials is compressed or elongated [33, 36, 43].

Magnetostriction Constants

The magnetostriction $\lambda = dl/l$ is defined as the fractional change in length l associated with a change in magnetisation from a demagnetised state to a fully saturated state. λ is a dimensionless material parameter and generally depends on the sample direction. For cubic materials two magnetostriction constants, λ_{100} and λ_{111} are defined along the crystal axes and diagonals, respectively. In case of an anisotropic medium the saturation magnetostriction λ_S can be defined. For polycrystalline materials with randomly oriented grains it is given by [11, 44, 45]:

$$\lambda_S = \frac{2}{5}\lambda_{100} + \frac{3}{5}\lambda_{111}. \tag{2.20}$$

Magnetoelastic Coupling

I will now introduce a phenomenological approach to the magnetoelastic anisotropy energy [8, 41]: Starting from a cubic crystal the anisotropy energy density can be expanded in powers of the strain ϵ_{ij}:

$$e = e_c^0 + \sum_{i \geq j} \frac{\partial e_c}{\partial \epsilon_{ij}} \epsilon_{ij} + \cdots = e_c^0 + e_{me}. \tag{2.21}$$

Considering only the two lowest order terms and under some symmetry considerations we define:

$$\frac{\partial e_c}{\partial \epsilon_{ii}} = B_1 m_i^2 \qquad \text{and} \qquad \frac{\partial e_c}{\partial \epsilon_{ij}} = B_2 m_i m_j, \tag{2.22}$$

where B_1 and B_2 are the magnetoelastic coupling constants and m_i are again the direction cosines of the magnetisation with respect to the cubic axes. The magnetoelastic anisotropy is rewritten as:

$$e_{me} = B_1 \left(m_x^2 \epsilon_{xx} + m_y^2 \epsilon_{yy} + m_z^2 \epsilon_{zz} \right) + B_2 \left(m_x m_y \epsilon_{xy} + m_y m_z \epsilon_{yz} + m_z m_y \epsilon_{zy} \right). \tag{2.23}$$

The magnetoelastic coupling constants and the magnetostriction constants are related via the elastic stiffness tensor c_{ijkl}:

$$\lambda_{100} = -\frac{2}{3} \frac{B_1}{(c_{1111} - c_{1122})} \qquad \text{and} \qquad \lambda_{111} = -\frac{1}{3} \frac{B_2}{c_{2323}}. \tag{2.24}$$

In isotropic materials – such as randomly oriented polycrystalline or amorphous films – under uniaxial strain ϵ the magnetoelastic anisotropy takes the form of a uniaxial anisotropy with anisotropy constant [20]:

$$K_{me} = \frac{3 Y \epsilon \lambda_S}{2} \tag{2.25}$$

where Y is the Young's modulus of the material [8, 33, 41, 44].

2.4.5 Surface and Interface Anisotropy

The broken translational symmetry at the surface of a ferromagnetic material or at the interface with another material gives rise to a surface or interface anisotropy [46]. For simplicity I will just call it the interface anisotropy[2]. Its strength and symmetry are again determined by the spin–orbit coupling between the electron spin and the crystal field that is altered at the interface. In a phenomenological approach the interface anisotropy can be represented as a uniaxial anisotropy:

$$e_i = \frac{K_i}{t} sin^2 \chi, \tag{2.26}$$

where K_i is the interface anisotropy constant, t is the film thickness and χ is the angle between the surface normal and the magnetisation. A positive K_i favours an out-of-plane magnetisation direction, for example

[2] From a certain point of view the surface is also an interface between the ferromagnet and vacuum/air.

at the Co/Pt interface [47]. In very thin films, the interface anisotropy can contribute significantly and overcome the effect of bulk anisotropies and the magnetostatic energy to create a net Perpendicular Magnetic Anisotropy (PMA). As the thickness of the film increases a Spin Reorientation Transition (SRT) eventually occurs, where the magnetisation rotates into the film plane due to the reduced relative contribution of the interface anisotropy [14, 28, 33].
The interface anisotropy favours an in-plane magnetisation for $K_i < 0$, as observed for example at the Ni/Cu interface. Interestingly, a perpendicular magnetic anisotropy is imposed on the multilayer as a result of the strain that develops between the Ni and Cu layers. Hence, with increasing film thickness a first SRT from in-plane to out-of-plane is observed. A second SRT back into the film plane is driven by strain relaxation and the effect of the magnetostatic energy [48–50].

2.4.6 Exchange Bias

Exchange bias is the result of the exchange interaction that occurs at the interface between a ferromagnetic (FM) and an antiferromagnetic (AFM) material [51,52]. At the interface the AFM exhibits uncompensated spins. If the sample is heated above the Neél temperature of the AFM but below the Curie temperature of the FM ($T_N < T < T_C$) in an applied external magnetic setting field, the FM spins align with the field while the AFM is paramagnetic. When cooling through the Néel temperature, the uncompensated AFM spins align with the FM spins due to the exchange interaction. These uncompensated spins then remain pinned in the direction determined by the setting field if the AFM anisotropy is large enough. The net AFM moment at the interface exerts a torque on the FM spins: It will be easier for an external magnetic field to align the FM magnetisation in the direction of the net AFM moment than in the opposite direction. This leads to a shift in the hysteresis curve by H_{EB} as indicated schematically in Figure 2.5. Since the exchange bias is an interface effect, the bias field:

$$H_{EB} \propto \frac{1}{t}, \tag{2.27}$$

where t is again the thickness of the FM layer. The exchange bias also depends on the thickness of the AFM layer but that dependence is more complicated.
In case the anisotropy of the AFM is not strong enough to pin the un-

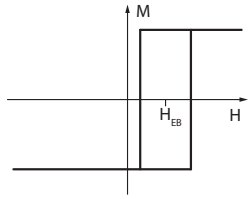

Figure 2.5. The exchange bias between an antiferromagnet and a ferromagnet leads to a shift in the ferromagnetic hysteresis curve by H_{EB}.

compensated spins, they will flip in an applied magnetic field leading to a uniaxial exchange anisotropy. The switching field is increased as AFM spins need to be dragged along by the magnetic moments of the ferromagnet [53–55].

2.5 Torque Equations

Energy minimisation is not the only approach that can be taken in order to calculate the equilibrium magnetisation distribution. As stated in the introduction to this Chapter, it can also be determined by requiring the torque $\overrightarrow{L}$ on the magnetisation to be zero. The equation of motion is given by:

$$\frac{d\overrightarrow{M}}{dt} = \gamma \left(\overrightarrow{M} \times \overrightarrow{H} \right) = \gamma \overrightarrow{L}, \tag{2.28}$$

where $\gamma < 0$ is the gyromagnetic ratio of the electron [13, 21].

Effective Fields

In order for Equation 2.28 to describe the motion of magnetic moments in a ferromagnetic solid, the effect of all the energy contributions previously discussed need to be included. It is therefore necessary to define an effective magnetic field:

$$\overrightarrow{H_{eff}} = \overrightarrow{H_h} + \overrightarrow{H_{ms}} + \overrightarrow{H_{ex}} + \overrightarrow{H_{an}}. \tag{2.29}$$

The first two contributions are the externally applied magnetic field and the field created by the magnetisation itself. The exchange energy can be represented as a an effective field $\overrightarrow{H_{ex}}$ in a mean field approach [29, 30] as mentioned previously. The effective anisotropy field for a uniaxial anisotropy can be written as:

$$H_{an} = \frac{2K_u}{\mu_0 M_s}, \tag{2.30}$$

where the field points along the uniaxial anisotropy axis [13, 14, 21].

The Landau Lifshitz Gilbert Equation

Equation 2.28 describes the precession of the magnetisation in a magnetic field, with a constant angle θ between them. In reality the magnetisation follows a damped precession and eventually aligns with the direction of the effective field. The damping is caused by a loss of energy due to coupling to, for example, lattice vibrations and can be expressed as an additional phenomenological torque. The damping is quantified by the damping constant α and the dynamics of the magnetisation is given by the Landau-Lifshitz-Gilbert (LLG) equation:

$$\frac{d\vec{M}}{dt} = \gamma\left(\vec{M} \times \vec{H}\right) + \frac{\alpha}{M_S}\left(\vec{M} \times \frac{d\vec{M}}{dt}\right). \tag{2.31}$$

It not only allows determination of the equilibrium magnetisation but also magnetisation dynamics [13, 21, 56].

2.6 Magnetic Domains and Domain Walls

Generally, the total energy of a ferromagnetic sample can be minimised by the formation of magnetic domains. While the magnetisation within a domain is largely uniform, its orientation changes from one domain to the next. The magnetostatic energy is the reason for the existence of magnetic domains as can be understood by considering a large enough ellipsoid as a simple example. The total surface charge of an ellipsoid magnetised along its long axis (Figure 2.6(a)) is the same as in the case where the magnetisation has been subdivided into two anti-parallel domains (Figure 2.6(b)). Yet, the subdivision into two domains leads to a reduction in energy because opposite charges attract each other. A similar argument can be used to explain the formation of domains in samples of any finite shape. The

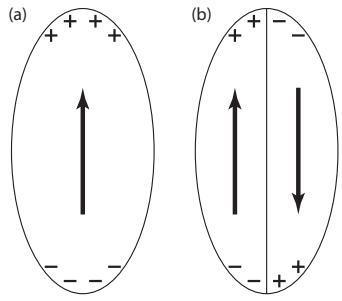

Figure 2.6. The magnetostatic energy of a uniformly magnetised body (a) is larger than if the magnetisation is divided into magnetic domains (b).

subdivision into further domains continues as long as it is energetically favourable. The gain in energy from the creation of an additional domain is countered by the energy cost of forming the boundary between domains, the domain wall. Within the domain wall the magnetisation rotates gradually in order to minimise the exchange energy at the cost of an increased anisotropy energy. The formation of magnetic domains is therefore the result of a competition of the long-range magnetostatic energy favouring anti-parallel magnetisation alignments, the short-range exchange energy favouring a parallel magnetisation, and the anisotropy energy favouring a collinear arrangement of the magnetisation. In very small samples the exchange interaction dominates, while in a hypothetical infinite sample the absence of surfaces means that the magnetostatic energy does not contribute. In both cases the magnetisation is uniform, but in any other case domains form [8, 19, 28, 57].

2.6.1 Domain Patterns

Due to the symmetries of the energy contributions, domains are usually not of random shape and orientation but form patterns such as stripes and more complicated structures. In small rectangular thin film elements the magnetisation usually forms domains with a magnetisation angle of 90° between them due to the effect of the shape anisotropy [20].

Anisotropy Modulations

The shape and orientation of magnetic domains can also be set by local anisotropy modulations. This can be done for example by local ion-irradiation that changes the structural properties of thin films [58–63]. Using a substrate that exhibits a modulation between a single crystalline and a polycrystalline substrate surface can lead to selective epitaxial growth of a thin magnetic film [64]. These methods have been used in order to create regions that alternate between in-plane and out-of-plane magnetisation [58, 64], or to rotate an in-plane anisotropy [59, 61] or exchange bias [60] by applying a magnetic bias field during ion-irradiation.

2.6.2 Domain Walls

As stated above, magnetic domains are separated by relatively thin transition regions – magnetic domain walls – in which the magnetisation direction changes continuously. The finite extent of domain walls is due to the fact that a gradual magnetisation rotation has a lower exchange

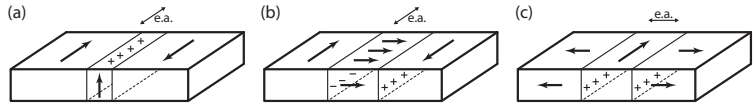

Figure 2.7. Sketch of domain walls in ferromagnetic thin films: Bloch walls (a) create charges at the film surfaces while Néel walls (b & c) exhibit volume charges within the film. In uncharged domain walls (b) the charges create a dipole and cancel on average while in charged domain walls (c) they do not.

energy than if the magnetisation was to switch abruptly. However, the resulting misalignment of the magnetisation with the anisotropy axes leads to an increase in energy. The width of the domain wall is therefore, in the simplest case, the result of a competition between the exchange and anisotropy energies [14, 20, 28, 57].

180° Domain Walls

The simplest case for a domain wall is in an infinite medium with uniaxial anisotropy exhibiting two domains. To avoid the accumulation of magnetic charges the wall is defined along a plane that is parallel to the anisotropy axis. The magnetostatic energy is moreover minimised – zero to be exact – when the magnetisation rotates parallel to the wall plane. This wall is called a Bloch wall and its width can be calculated analytically to be:

$$\delta_{Bloch} = \pi l_{ex}, \tag{2.32}$$

where the exchange length:

$$l_{ex} = \sqrt{\frac{A}{K_u}} \tag{2.33}$$

gives a measure of the dimensions over which the exchange energy dominates. The Bloch wall for the case of a magnetic film is sketched in Figure 2.7(a).

In thin films, magnetic charges are created at the top and bottom of the Bloch wall. For thin enough films the domain wall therefore minimises its magnetostatic energy by having the magnetisation rotate in the film plane. This is called a Néel wall and is shown schematically in Figure 2.7(b). It is energetically favourable for films with a thickness comparable to the Bloch wall width or below. While the Néel wall does not exhibit surface charges, volume charges accumulate in the core of the wall, thus forming a magnetic dipole. As a result, the Néel wall exhibits a core where the magnetisation rotates rather abruptly and two tails that are much more extended [65]. In the following I will call this type of Néel wall an uncharged domain wall because it does not exhibit a net magnetic

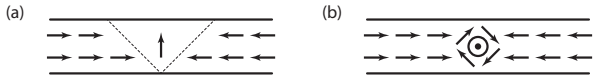

Figure 2.8. Examples of a transverse wall (a) and a vortex wall (b) in a magnetic nanowire. In the transverse wall the magnetisation at the centre can point up or down while the vortex wall can have two chiralities and the magnetisation at its centre can point into the plane or out of it. Moreover, both types of domain wall can be the result of a head-to-head or tail-to-tail magnetisation orientation in the domains.

charge. In case the Néel wall is perpendicular to the uniaxial anisotropy the charges that accumulate on both sides of it have the same sign (Figure 2.7(c)), and a net magnetic charge is associated with the domain wall. The charges lead to a dependence of the domain wall width on film thickness t, which can be approximated as [66]:

$$\delta_{c,Neel} \approx \frac{\pi \mu_0 M_s^2 t}{4K_u}. \tag{2.34}$$

There is no reason for the occurrence of charged domain walls in thin films, but the situation is different in magnetic nanowires where the shape anisotropy induces a uniaxial anisotropy along the wire axis. In that case more complicated domain walls form in order to reduce the magnetostatic energy. Depending on the nanowire's cross-sectional dimensions transverse walls (Figure 2.8(a)) or vortex walls (Figure 2.8(b)) are formed [13, 14, 19, 20, 67, 68].

90° Domain Walls

Ferromagnets with a cubic anisotropy can also exhibit domain walls where the magnetisation rotates by an angle of 90°. The magnetostatic energy then contributes to the profile of the 90° domain wall. This type of domain wall can also occur when domain patterns (cf. Section 2.6.1) are present: In small rectangular thin film elements domains are separated by 90° domain walls as well as in many anisotropy modulated films. Ignoring the magnetostatic energy, the width of a 90° Néel wall is given by:

$$\delta_{90} = \pi \sqrt{\frac{A}{2K_u}}, \tag{2.35}$$

which is obtained by adapting the case of a 180° domain wall to a wall of reduced angle [19, 20, 64].

Domain Wall Widths

It is useful to define the domain wall width over which the magnetisation rotates. This can be done as a function of the slope of the magnetisation angle ϕ at the centre of the domain wall [69]. While it yields the correct

result for the Bloch wall, it fails for most other walls, e.g. for Néel walls, because their extended tails are ignored. A more suitable definition uses an integral over the wall profile [70]. The width is then also defined for asymmetric walls and arbitrary spin rotations if it is taken as [IV]:

$$\delta = \int_{-\infty}^{+\infty} cos(\phi\prime)^2 dx, \tag{2.36}$$

where $\phi\prime$ is the reduced magnetisation angle:

$$\phi\prime = \left(\phi - \frac{\mid \phi_1 + \phi_2 \mid}{2}\right) \cdot \frac{180}{\mid \phi_1 - \phi_2 \mid}, \tag{2.37}$$

with magnetisation angles ϕ_{i} in the neighbouring domains [19, 20].

Magnetic Field Driven Domain Wall Motion

Once a domain wall has been nucleated in a ferromagnetic film it can be moved by a magnetic field that favours the magnetisation in one of the adjacent domains. For small magnetic fields, the motion of the domain wall is a thermally activated process influenced by domain wall pinning at imperfections, known as creep. At larger fields the pinning is too weak to affect the domain wall motion and the velocity v increases linearly with the applied field [71]. The domain wall mobility $\mu = dv/dH$ is then a positive constant that is limited by intrinsic damping [72]. Above the so-called Walker field $\mathrm{H_W}$ the domain wall motion changes from a steady to a precessional mode of propagation where the domain wall periodically alternates between the Bloch and the Néel type [73, 74]. As a result of this Walker breakdown, the velocity drops abruptly. With increasing external field the domain wall motion undergoes a region of negative mobility. Eventually the increase in wall velocity becomes linear again, but with reduced wall mobility.

Domain wall motion is also observed in magnetic nanowires [75, 76]. The process can be controlled by attaching a larger pad to the nanowire [77]. In this nucleation pad the switching field is reduced (cf. Section 2.7) and a domain wall is thus nucleated there before propagating into the nanowire. Similarly to the case of a continuous film, the domain wall velocity as a function of field shows two linear regimes separated by a region of negative wall mobility due to the Walker breakdown [78]. In the intermediate regime the domain wall oscillates and can show periodical transformations between a transverse and a vortex wall [74, 79]. Experimentally, domain wall speeds of the order of 1000 m/s have been obtained in magnetic fields of a few tens of mT [80, 81].

Current Driven Domain Wall Motion

In the case of magnetic field driven motion, adjacent domain walls will move in opposite directions as the domains that are bound by them shrink or grow [82]. Current driven domain wall motion can move several domain walls in the same direction [83]. Another advantage is that the magnetic field needed to move a domain wall does not scale with the size of the nanowire, while the current – and therefore the power – needed to move a domain wall is reduced in smaller wires because the domain wall motion depends on current density [82, 84]. Two main mechanisms allow for current driven domain wall motion: Spin Transfer Torque [85–87] and Momentum Transfer [88]. For relatively wide walls the Spin Transfer Torque dominates: In a ferromagnet the electric current is always associated with a spin polarised current. In order to align their magnetic moment with the local magnetisation direction the electrons crossing the domain wall have their net spin reversed and as a result of angular momentum conservation this creates a torque onto the wall, hence moving it. In the rare case of a very thin domain wall, Momentum Transfer due to the reflection of electrons dominates. This effect is proportional to the charge current. While the domain wall velocities obtained were initially rather low [89, 90], speeds of the order of 100 m/s have been achieved [82]. Recently a velocity of 750 m/s was demonstrated in antiferromagnetically coupled nanowires [91]. Unfortunately, the current densities required for magnetic domain wall motion are of the order of at least 10^{10} A/m^2 [89, 92–95] and reach 10^{12} A/m^2 for high velocities [82, 91]. As a result, domain wall motion is affected by Joule heating that can even lead to the temperature of the nanowire exceeding the Curie temperature [57, 84, 94, 96].

An alternative driving mechanism was demonstrated recently in multilayers that consist of a thin ferromagnetic metal sandwiched between an oxide and a heavy metal where the Spin Hall Effect (SHE) drives magnetic domain wall motion [97]. In order for all domains to move in the same direction their chirality needs to be fixed, which can be attained by use of Dzyaloshinskii–Moriya interactions [98, 99].

Domain Wall Pinning

Domain walls move in a potential landscape created by pinning sites caused by chemical or microstructural imperfections such as the roughness of nanowire edges [14, 100]. These pinning sites impede domain wall dynamics and lead to stochastic motion known as Barkhausen jumps

[101] in the field driven case. A comparable behaviour is observed in the current driven situation [93]. Imperfections can also be created artificially as point defects [102] or, more commonly, as protrusions, constrictions, and bends in the nanowire geometry [95, 100, 103–107]. This allows controlled pinning of domain walls at lithographically defined locations. The geometrical variations create potential barriers or wells depending on their shape and the type and chirality of the domain wall. The strength of the pinning decreases with increasing wire width.

A ratchet for domain wall motion can be devised when asymmetric triangular notches are used [108–110]: The total energy of the domain wall is proportional to its area which increases gradually when the wall moves in one direction but abruptly in the other. This creates a sawtooth potential for domain walls and it is easier for them to move in the direction along which the inclination of the notch is lower. Using a series of triangular notches, unidirectional motion of domain walls is possible in sequential alternating magnetic fields without the use of electric currents. The required sawtooth potential can also be obtained by anisotropy modulations through ion beam irradiation [62].

In the absence of geometric variations, domain walls can also be pinned by the stray field created by a domain wall in an adjacent nanowire [111] or by a magnetic nanopillar grown onto the nanowire [112]. In the latter case it was demonstrated that the pinning in a nanowire exhibiting perpendicular magnetic anisotropy depends on the pillar height and on whether its magnetisation points up or down. Finally, an interesting way to pin domain walls is to use anisotropy modulations. A domain wall can be pinned at the anisotropy boundary between two regions of different anisotropy strength and/or orientation [63, 64]. The domain wall may be termed an "anisotropy constrained magnetic wall" [64].

Domain Wall Tuning

The width and type of domain walls does not only depend on intrinsic material parameters but also on the geometry and dimensions of the body containing them [103, 113, 114]. As previously mentioned, the domain wall can be of Néel or Bloch type depending on the thickness of a thin film and the width of Néel walls generally decreases when the lateral dimensions of the ferromagnet are reduced, for example in nanowires. Recently another way to tune magnetic domain walls has been demonstrated in multilayers where the Dzyaloshinskii–Moriya interaction contributes significantly [115, 116]. Néel walls of chosen chirality, Bloch walls, or a mix-

ture of both can be stabilised by including spacer layers or adding uniaxial strain during multilayer growth. However, these approaches allow only for a limited active tuning of domain wall properties once the magnetic sample has been fabricated. A significant part of the results presented in this Thesis (Chapter 6) are devoted to the active tuning of magnetic domain walls.

Domain Wall Devices

The use of controlled domain wall motion in devices for memory or logic applications holds the fascinating promise of reliable and low power technological solutions. The reliability is due to the fact that no mechanical motion is needed (such as in Hard Disc Drives) and leakage currents do not play a role (as in Solid State Memory). Low power devices are envisaged due to the low intrinsic power requirement for domain wall motion [20].

A complete magnetic logic has been devised [117], where logical operations such as NOT and AND gates, signal fan-out and crossover elements, and a way to write and delete data are integrated using planar magnetic nanowires. The different elements are implemented through a specific device geometry. A rotating magnetic field plays the role of power supply and clock for the circuit. The required magnetic field is also the main drawback of the design because its generation requires bulky solutions with high power consumption.

An alternative is of course the use of the Spin Transfer Torque for domain wall propagation. As mentioned before, it allows for a series of domain walls to be controllably and reversibly moved in the same direction [83]. This has led to the proposal of the Racetrack Memory [4–6], a concept that uses domain walls in a shift register driven by spin polarised currents. It has the advantage that the current required for domain wall motion scales with the size of the device. An obstacle to the scaling is stray field coupling between adjacent nanowires but this problem has been overcome in racetracks formed by antiferromagnetically coupled nanowires that do not exhibit a net magnetisation [6, 91].

A third application is based on the use of the oscillation of a pinned magnetic wall as a tunable source of microwaves. The oscillation of the domain wall can of course be driven by a microwave current with the resonance frequency set by an applied magnetic field [103]. It is also possible to obtain an oscillation with a low dc current [118, 119]. In this case, the nanowire geometry and material parameters need to be chosen in a way

that there is only a small energy difference between the Bloch and the Néel wall. If the applied current is larger than the one needed for Walker breakdown behaviour – but lower than the depinning current – oscillations between both wall types can be induced.

2.7 The Stoner–Wohlfarth Model

In samples where a uniaxial anisotropy dominates, a simple and instructive model can be used to describe the shape of hysteresis curves. Known as the Stoner–Wohlfarth model [120], it assumes a homogeneous magnetisation, i.e. the exchange energy can be ignored and the magnetostatic energy is not taken into account. This situation is encountered in small enough ellipsoids (cf. Section 2.4.1) and the model was mainly developed for that situation. Still, the original publication already mentions that the model is applicable to any kind of uniaxial anisotropy. For the situation just described, the energy density is given by:

$$e_{sw} = K_u \, sin^2\phi, -\mu_0 \, M_S \, H \, cos(\theta - \phi), \tag{2.38}$$

where ϕ is the angle between the uniaxial anisotropy axis and the magnetisation and θ the angle between the anisotropy axis and the applied magnetic field. The model has a simple analytical solution for fields applied along the easy ($\theta = 0$) and hard ($\theta = 90°$) axis. The magnetisation direction that minimises the energy density in Equation 2.38 can easily be found using its first and second derivative with respect to ϕ:

$$\frac{\partial e_{sw}}{\partial \phi} = 2K_u \, sin(\phi)cos(\phi) - \mu_0 \, M_S \, H \, sin(\theta - \phi) = 0, \tag{2.39}$$

$$\frac{\partial^2 e_{sw}}{\partial \phi^2} = 2K_u \, cos(2\phi) + \mu_0 \, M_S \, H \, cos(\theta - \phi) > 0. \tag{2.40}$$

It is useful to define the reduced magnetic field $h = H/H_{an}$ using the anisotropy field from Equation 2.30 and to use the reduced magnetisation $m = M/M_S$.

In case of an easy axis field two energy minima at $m = \pm 1$ (i.e. $\phi \in [0, \pi]$) can be found at remanence. These solutions continue to be local minima for $-1 < h < 1$, while for $h < -1$ only $m = -1$ is a minimum and for $h > 1$ the only solution is found at $m = 1$. This results in a square hysteresis curve with abrupt magnetisation switching as sketched in Figure 2.9(a).

For fields applied along the hard axis the same minima as in the easy

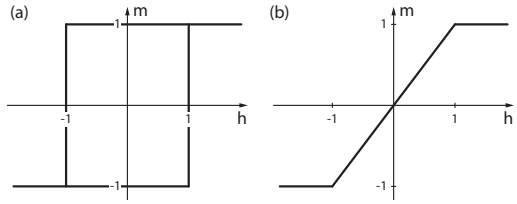

Figure 2.9. Illustration of an easy axis hysteresis curve (a) and a hard axis hysteresis curve (b) for a uniaxial anisotropy according to the Stoner–Wohlfarth model.

axis case are found for $h < -1$ and $h > 1$. For $-1 < h < 1$ the magnetisation increases linearly as a function of magnetic field as shown in Figure 2.9(b). The hard axis hysteresis curve can be used to determine the uniaxial anisotropy strength by measuring its slope.

The Stoner–Wohlfarth model can also be used to determine the shape of hysteresis curves for arbitrary angles θ but a numerical solution is then necessary. Nonetheless, the angular dependence of the coercive field, the switching field, and the remanent magnetisation can be determined analytically. The reduced coercive field is given by:

$$h_c = cos|\theta|, \tag{2.41}$$

and equals the anisotropy field in the easy axis case and is zero in the hard axis case as just discussed. The switching field where the magnetisation rotates abruptly is not always the same as the coercive field. It can be determined from the condition that one of the two minima found at remanence disappears in an applied magnetic field. This happens when both first and second derivative of the energy are zero, and the angular dependence of the reduced switching field is given by:

$$h_{sw} = \frac{1}{\left(sin^{2/3}\theta + cos^{2/3}\theta\right)^{3/2}}. \tag{2.42}$$

Plotting the switching field in polar coordinates (Figure 2.10(a)) yields the so-called Stoner–Wohlfarth asteroid.

In practice the magnetisation is not uniform throughout the reversal process. The nucleation and motion of magnetic domain walls play a significant role. The magnitude of the coercive and switching fields are therefore determined by the pinning of domain walls and their thermally activated depinning. Since domain nucleation happens in the easy axis case while coherent rotation prevails in the hard axis curve, the switching field will in practice not have the fourfold symmetry seen in Figure 2.10(a). The

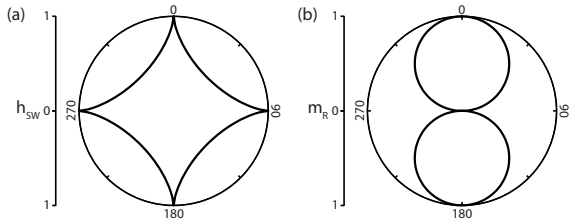

Figure 2.10. Angular dependence of the reduced switching fields $h_{SW} = H_{SW}/H_{an}$ (a) and the reduced remanent magnetisation $m_R = M_R/M_S$ (b) according to the Stoner–Wohlfarth model.

values determined from the Stoner–Wohlfarth model are therefore only an upper limit for the coercive and switching fields. In order to accurately determine the orientation of a uniaxial anisotropy the remanent magnetisation can be plotted as a function of angle (Figure 2.10(b)). Its reduced value:

$$m_R = |cos\theta| \tag{2.43}$$

is simply given by the projection of the magnetisation vector onto the easy axis [13, 14, 19, 55].

Cubic Anisotropy

The Stoner–Wohlfarth model can be modified in order to accommodate a cubic instead of a uniaxial anisotropy. This case is more complex than the uniaxial one, but it can be determined that for many field angles the magnetisation exhibits two switching events characterised by two switching fields as plotted in Figure 2.11(a). The value of the remanent magnetisation is again given by the projection of the magnetisation vector onto the closest anisotropy axis and is sketched in Figure 2.11(b) [28],[III].

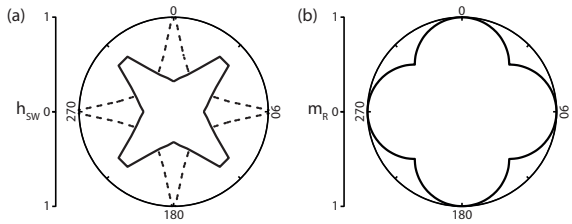

Figure 2.11. (a) Angular dependence of the reduced switching fields $h_{SW} = H_{SW}/H_{an}$ in case of a cubic anisotropy. For many field angles two switching events are observed. (b) Corresponding reduced remanent magnetisation $m_R = M_R/M_S$.

3. Ferroelectricity

You know nothing, John Snow.

George R.R. Martin

In dielectric materials an applied electric field E [V/m] induces an electric polarisation P [C/m^2] proportional to the susceptibility χ. In analogy to ferromagnetism, ferroelectric materials are defined as insulators exhibiting a spontaneous electric polarisation that can be switched by an electric field. The switching process can be characterised by a ferroelectric hysteresis curve. Similarly to the ferromagnetic equivalent (cf. Figure 2.1), the saturation polarisation P_S, remanent polarisation P_R, saturating field E_S, and coercive field E_C may be defined. At the ferroelectric Curie temperature T_C a transition to a paraelectric phase occurs. Just like ferromagnets, ferroelectric crystals usually exhibit domains [10, 121–124].
While the occurrence of ferromagnetism is ultimately based on the electron's angular momenta and the exchange interaction, ferroelectric order is more difficult to explain, because it can be the result of several distinct mechanisms. Moreover, these mechanisms are usually not well understood. Unlike magnetism, the occurrence of ferroelectricity is closely linked to the symmetry of the crystal. The high-temperature paraelectric phase is characterised by a symmetry **G** associated with one of the 32 point groups. It is called the parent or prototype phase. The transition to the low-temperature ferroelectric phase can be reconstructive or distortive in nature. I will not discuss the former case where the transition includes a breaking of chemical bonds and a complete change of the atomic arrangement. At a distortive transition the parent phase distorts into a phase of lower symmetry **F**. This phase can be viewed as a slightly altered structure due to a shift in crystal atom positions. The symmetry operations of group **F** are contained in **G**. The breaking of certain spatial symmetries at the phase transition is a prerequisite for the

development of a spontaneous polarisation. The polarisation is caused by the arrangement of ions in the crystal. Of course the separation of positive and negative charges causing the electric polarisation comes at a cost in electrostatic energy and a mechanism that favours this separation has to exist. Unfortunately, it is generally unclear how this mechanism works [27, 121, 123–127].

Ferroelectric materials are also pyroelectric, i.e. they exhibit a change in spontaneous polarisation as a function of temperature. Materials may be pyroelectric but not ferroelectric if their polarisation is not switchable by an external field. All ferroelectrics are piezoelectric, i.e. a volatile change of their polarisation is induced when strain is applied. As a result of the induced polarisation, charges are created at the surfaces of a piezoelectric and a voltage can be measured across it. When an electric field is applied to a piezoelectric the converse effect leads to the development of strain. Since most ferroelectrics exhibit a polarisation that is associated with a spontaneous lattice elongation or contraction they are usually also ferroelastic. This means that they exhibit a spontaneous strain that can be hysteretically switched with an applied stress [121, 123, 128].

The piezoelectric properties of ferroelectrics can be used to convert electrical signals to a mechanical response in transducers. The inverse effect can be used in sensors. The spontaneous polarisation could be used for information storage, but in order to determine the polarisation state it is generally necessary to switch the polarisation. This destructive readout has the disadvantage of increasing the problem of a limited number of reliable switching events due to mechanical fatigue. Ferroelectrics could also replace the gate dielectric in non-volatile field effect transistors (FET).

It should be noted that correctly measuring the hysteresis curve of a ferroelectric material is much more demanding than for its ferromagnetic counterpart. Application of an electric field requires the deposition of electrodes so that a device for hysteresis measurement is fabricated. The hysteresis curve will then depend on the components of the measurement system. The materials used for electrodes have been shown to have a strong influence and mechanical clamping also changes the response. The experimental and theoretical difficulties encountered when studying ferroelectrics combined with the limited prospect for applications have led to them being studied less than ferromagnets[1] [121, 124, 127, 131].

[1] It may also be due to the fact that while ferroelectricity was experimentally demonstrated in 1920 [129], ferromagnetism has been known for millennia, with the first review published in 1600 [130].

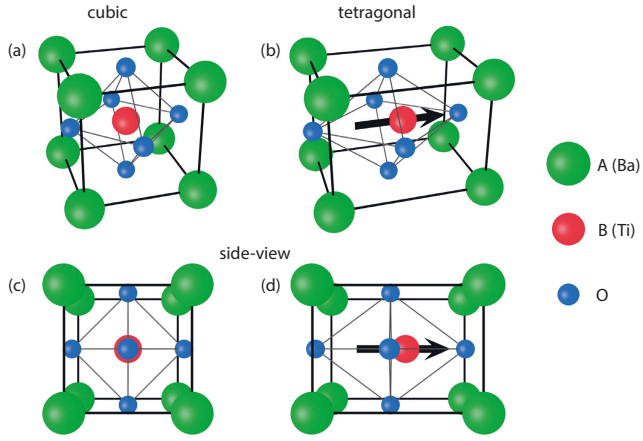

Figure 3.1. (a) Centrosymmetric cubic perovskite ABO_3 (for example $BaTiO_3$) structure. Large A (Ba) cations are located at the unit-cell corners while the body centre is occupied by a small B (Ti) cation. Oxygen anions occupy the face centres. (b) Distorted tetragonal ferroelectric lattice. The polarisation is indicated by the arrow. (c) and (d) show the side views of the cubic and tetragonal lattice, respectively, emphasising the shift of the B cation and the oxygen anions.

3.1 Perovskite Ferroelectrics

Perovskite oxides are the most studied ferroelectrics. The typical cubic ABO_3 parent phase sketched in Figure 3.1(a) has space group $Pm3m$. It consists of an oxygen octahedron with a small cation (B) at its centre and large cations (A) at the corners of the unit cell. Depending on their composition the perovskites show a large variety of physical properties: they can be insulating, metallic, ferromagnetic or ferroelectric. Examples of ferroelectric perovskites include $BaTiO_3$ and $PbTiO_3$. The latter has a Curie temperature of 490°C, below which its structure is tetragonally distorted as shown schematically in Figure 3.1(b). The elongated axis is called c-axis while the other two are called a-axes. At room temperature it exhibits one of the largest polarisation ($P_S = 0.75$ C/m^2) and lattice elongation (6.5%) [132]. $BaTiO_3$ is the first perovskite ferroelectric to be identified with Ba^{2+} as A and Ti^{4+} as B. Unlike $PbTiO_3$ it exhibits several ferroelectric phases when cooling down from the paraelectric parent phase. The first phase transition to a tetragonal structure ($P4mm$) occurs at 120°C. Further transitions to an orthorhombic ($Amm2$) and a rhombohedral ($R3m$) symmetry occur at 5°C and −90°C, respectively. In this Thesis only the tetragonal phase at room temperature needs to be considered where the length of the a-axis is 3.992 Å while it is 4.036 Å for the c-axis. The resulting lattice elongation of 1.1% [121] is associated with a polarisation of 0.26 C/m^2 as found experimentally [121, 133] and theoret-

ically [134, 135]. Since $BaTiO_3$ is insulating it has a high resistivity ρ, of the order of 10^8 Ωm [9, 10, 123, 124, 127, 131, 136–143].

Each of the phase transitions is characterised by a small distortion of the crystal lattice. It can be viewed as an elongation along an edge ($[001]$) in the tetragonal phase, along a face diagonal ($[011]$) in the orthorhombic phase and along a body diagonal ($[111]$) in the rhombohedral phase. Each distortion is associated with a shift in the position of the ions. In the tetragonal phase the Ti ion is shifted relative to the Ba ions in one direction (right in Figure 3.1(d)), while the oxygen ions are shifted in the other (left in this case). The electric polarisation is thus a consequence of the shift of the positively charged Ti ion relative to the negatively charged oxygen octahedron and points in the same direction as the lattice elongation. The distortion leads to an increase in energy due to the Coulomb interaction, but a decrease in energy is obtained due to hybridisation between the empty d states of the Ti ion and the 2p states of one of the oxygen ions. This means that the oxygen octahedron is distorted because not all oxygen ions shift by the same amount. More importantly, the presence of an ion in a d^0 state seems to be a prerequisite for the occurrence of ferroelectricity in many oxides [9, 10, 124, 127, 141, 143–146].

Due to the mechanism that causes an electric polarisation in the unit cell the ferroelectric properties are highly anisotropic and depend on the symmetry of the crystal. In the tetragonal phase the lattice can be elongated along 3 different directions leading to 6 possible orientations of the polarisation. In the rhombohedral phase the polarisation can point into 8 equivalent directions. From purely electrostatic considerations one would expect the polarisation in neighbouring unit cells to be aligned antiparallel. This situation is encountered in antiferroelectric materials. In ferroelectrics the long-range effect of strain associated with the polarisation via the lattice elongation is the major contribution that leads to a parallel orientation of the polarisation. This mechanism fully explains ferroelectricity in $PbTiO_3$ but not in $BaTiO_3$. It seems that in the latter case, the long-range Coulomb interaction actually contributes to the ferroelectric alignment [135, 146–149].

3.2 Ferroelectric Domains and Domain Walls

For the remainder of this Chapter, I will focus on the tetragonal lattice encountered in $BaTiO_3$ at room temperature. As mentioned before, when the ferroelectric crystal is cooled from the paraelectric high-temperature phase through its Curie temperature there are 6 – in principle energetically equivalent – orientations for the polarisation. Ferroelectrics therefore generally divide into domains of uniformly polarised regions. As for ferromagnets, the formation of domains is generally caused by the finite size of the ferroelectric sample. There is a major difference, though: The spontaneous deformation of the crystal lattice is two orders of magnitude larger than the one due to magnetostriction in ferromagnets [8, 150]. Strain relaxation thus plays a more important role than the depolarising effects of the electrostatic energy. The latter can be minimised by the ferroelectric splitting into domains with oppositely oriented polarisation. The strain present in the material is due to its ferroelastic properties and leads to the formation of domains with perpendicular orientations of the polarisation. These domains are strongly affected by crystal impurities, the way the sample was grown, strain imposed by a substrate, and even the mere presence of the sample surface [151–153].
In plate-like crystals and thin films with a (001) orientation of the surface, a nomenclature according to Merz is used for domains of different polarisation orientation [154]: Domains with the polarisation normal to the surface are called c-domains while a-domains exhibit an in-plane polarisation. The latter can be further subdivided into a_1-domains with the polarisation along $[100]$ and a_2-domains with the polarisation along $[010]$ [121, 127, 140, 146, 155–158].

Domain Walls

In the tetragonal phase, two types of domain walls are possible[2]. 180° domain walls separate domains of opposite polarisation orientation. These domain walls are not ferroelastic and in order to remain electrically neutral they are parallel to the ferroelectric polarisation in the domains, i.e. they are oriented along a lattice edge. Domains with perpendicular polarisation and lattice elongation are separated by 90° domain walls. As the elongated lattice needs to be matched on both sides of the domain wall the wall is oriented along one of the edge diagonals of the lattice. A fur-

[2] In the rhombohedral phase three types of domain walls can be found: 180°, 109° and 71° [155].

ther consequence is that the angle between the polarisation in adjacent domains deviates from 90° by the canting angle $\alpha = 2\,arctan(a/c)$. While this angle is rather small for $BaTiO_3$ ($\alpha \approx 0.5°$) it is large for $PbTiO_3$ ($\alpha \approx 3.5°$) [127, 142, 154, 155, 159–163].

Ferroelectric and ferroelastic domain walls differ significantly from their ferromagnetic counterpart. Their typical width is less than 10 nm, while ferromagnetic domain walls can range from at least 10 nm in width up to the μm scale. Furthermore, while a magnetisation of fixed magnitude rotates in the ferromagnetic domain wall, the change in polarisation in the ferroelectric domain wall procedes by a reduction of the local atomic displacement and its associated polarisation, i.e. no gradual rotation of the polarisation vector takes place. The different behaviours can be understood by considering the energies that contribute to the shape and width of the domain walls. In ferromagnets, the magnetic moments are quantised and do not change their magnitude. The only way to change the direction of the magnetisation is then by rotation. The exchange coupling favouring a wide domain wall is strong while the anisotropy energy favouring narrow domain walls is due to weak spin–orbit coupling. In ferroelectric materials, analogies to the exchange and anisotropy energies can be made. The "anisotropy energy" in ferroelectrics is strong because the polarisation direction is directly linked to the crystal symmetry and can only lie in certain directions. At the same time the magnitude of the polarisation is not quantised and can vary in magnitude more easily. This explains why ferroelectric domain walls do not exhibit a rotation of the polarisation. The energy difference between a ferroelectric and antiferroelectric arrangement of the polarisation in neighbouring unit cells can be viewed as an "exchange energy". Its strength is comparable to that of the ferroelectric anisotropy energy. Ferroelectric domain boundaries are therefore narrower than ferromagnetic domain walls.

Historically it has been very difficult to determine the width of ferroelectric domain walls. The intrinsic width is generally overestimated for various reasons: Residual strain, defects, and surfaces lead to a broadening of the domain wall and thermal fluctuations affect measurements. Moreover, the limited resolution of measurement techniques makes it difficult to measure such narrow domain walls. Combining experimental and theoretical results it is now generally accepted that 180° domain walls are one or two lattice constants wide, while 90° domain walls in $BaTiO_3$ have a width of a few nm [122, 127, 139, 154, 159, 160, 164–168].

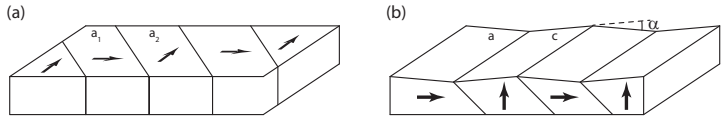

Figure 3.2. 90° domain patterns found in tetragonal $BaTiO_3$: (a) a_1–a_2 domains and (b) a–c domain patterns. In the latter case, the crystal surface exhibits an angle α between domains.

3.2.1 Stripe Domains

As already mentioned in Section 2.6.1 for the case of ferromagnetism, striped domain patterns can be observed for a large variety of systems [169]. Ferroelectricity is no exception. In the case of purely ferroelectric domains, 180° domain patterns are usually observed where prolonged domains with one polarisation direction are surrounded by domains of the opposite polarity. These domains can also be highly ordered and form regular stripe domains [170, 171].

Periodic stripe domains are generally encountered when the domains are separated by 90° domain walls. The domain walls are straight because a deviation would be associated with a large cost in elastic energy. The 90° domain patterns encountered in tetragonal $BaTiO_3$ with a (001) orientation of the surface are illustrated in Figure 3.2. In crystals exhibiting a–c domain patterns the aforementioned canting angle leads to an undulation of the sample surface as illustrated in Figure 3.2(b). Unfortunately, the research on 90° domain patterns has been limited because the presence of ferroelastic domain walls has usually only been investigated when they affect the measurement of other properties [127, 142, 158, 163, 172–174].

3.3 Ferroelectric Switching

By definition, the ferroelectric polarisation can be reversed in an applied electric field. In order to apply the electric field, electrodes need to be deposited. In some cases, fields are also applied using tips (e.g. of a Piezo-Force Microscope). Starting from a uniformly polarised plate-like crystal or a thin film the switching usually occurs in a three step process. In the first step, reverse domains nucleate inhomogeneously at the interfaces with the electrodes. At the interface the threshold for switching (the coercive field E_C) is reduced due to the broken symmetry, strain or the presence of built-in electric fields and charges. The second step consists of the rapid forward growth of needle-shaped domains normal to the film

surface until the opposite surface is reached. Finally, the domains grow by sideways motion of domain walls until the whole ferroelectric is switched. When domain walls are present in the crystal, their motion can be induced by applying an electric field that favours the polarisation direction in one of the domains [127, 139, 154, 156, 175–181].
In general, ferroelectric crystals do not possess a well-defined coercive field. Applying a field for a longer time increases the switching probability. E_C therefore increases with the frequency of the applied electric field. This also means that switching is possible in very low fields, although the process may take considerable time. Furthermore, ferroelectric domain boundaries can be pinned by imperfections. These will be discussed below but they generally lead to an increase of E_C with the number of switching cycles [127, 128, 154, 177, 182].

3.3.1 Motion of 180° Domain Walls

The forward growth of domain boundaries is much faster than the sideways motion but has attracted only limited interest [183, 184]. Since 180° domain walls are only a few lattice constants thick, they will have an equilibrium position in the crystal lattice. The energy needed to move them sideways is therefore higher than for their magnetic counterpart where the rotation of the order parameter is spread out [154]. The sideways motion of the ferroelectric domain boundaries most likely occurs via the nucleation of reversed steps along the previously existing wall. The velocity v is then given by the nucleation rate as $v \propto exp(-\delta/E)$ (with applied electric field E and activation field δ), a dependence that fits experimental observations [185–189]. The velocity of domain walls is ultimately limited by the speed of sound of the crystal and is of the order of 10^3 m/s [125,182]. When driven above the speed of sound the crystal would be destroyed by the sonic boom [155]. In practice, observed velocities are of the order of 1 m/s [180, 190] but speeds of the order of up to 10^2 m/s [191] and even 10^3 m/s have been achieved experimentally [188, 192] or predicted theoretically [193].

Ferroelectric Fatigue

The phenomenon of ferroelectric fatigue is a process in which the switchable remanent polarisation is reduced as a function of the number of applied field cycles. It is generally due to a reduction in the mobility of domain walls because of an increase in the amount and strength of pin-

ning sites. This can be caused by cracking in crystals with a large lattice distortion. Another mechanism is linked to oxygen vacancies. These have been shown to migrate towards domain walls and thus create ordered planes of oxygen vacancies that pin domain walls more efficiently. This effect can be reduced by using conducting oxide materials as electrodes [121, 139, 194–198].

3.3.2 Motion of 90° Domain Walls

Research on the motion of ferroelectric 90° domain walls is extremely limited. Movement of these domain walls leads to a change of both the direction of the polarisation and the associated strain. As a result, these domain walls are strongly affected by crystal imperfections. Moreover, the velocity of domain walls decreases as a function of the boundary distance from its equilibrium position due to the presence of an elastic restoring force [175]. Nonetheless, the intrinsic pinning should be lower than in the case of narrower 180° domain walls and it was shown theoretically that 90° walls are more mobile in $PbTiO_3$ [166]. Due to their ferroelastic nature, 90° domain walls can be driven not only by electric fields, but also via the application of stress. It should be noted that great care needs to be taken to avoid mechanical clamping when investigating ferroelastic domain wall motion. Any kind of clamping will affect domain wall motion and can lead to cracking of the crystal [127, 160, 162, 173, 199–202].

3.4 Domain Wall Devices

In analogy to the ferromagnetic case (cf. Section 2.6.2), technologies can be imagined where mobile ferroelectric domain boundaries are used. This prospect is especially exciting because ferroelectric domain boundaries can exhibit properties that are not present in the bulk, such as electrical conduction [203]. While ferroelectric domain walls usually exhibit lower velocities, the scaling known as Kittel–Mitsui–Furuichi law (analogous to the Kittel law in ferromagnetism) works to its advantage [127, 204, 205]. This law states that the domain periodicity scales as the square root of the film thickness, which is a significant advantage for device miniaturization. Since ferroelectric domain boundaries are narrower by at least one order of magnitude when compared with ferromagnetic domain walls

their packing can be much denser. Experimentally, domain periodicities down to a few nm have been observed in thin ferroelectric films [151, 171, 172, 206]. Such domain scaling has also been reported in nanocolumns of ferroelectric crystals [207, 208].

Controlled domain wall injection has been demonstrated using regions of lowered coercivity. This can be achieved by reducing the thickness of the ferroelectric [209] or by producing spots of locally enhanced field strength in focused ion beam (FIB) milled hole defects [210]. Such holes can also lead to a reduction of the local field and thus act as controlled pinning sites [210]. Pinning by local field reduction in ferroelectric nanowires can also be achieved by patterning protrusions while notches seem to increase local fields and therefore assist domain wall motion [211, 212].

A considerable obstacle to the development of a ferroelectric shift register is the fact that neighbouring domain boundaries move in opposite directions in an electric field. However, as in the case of magnetic field driven domain wall motion (see Page 29), unidirectional motion has been demonstrated. One approach uses a nanowire electrode contacted at one end [213]. Via the use of a complicated sequence of voltage pulses it was shown that several domain boundaries can be moved in the same direction. In addition, Whyte et al. used a diode effect associated with a modulation in the physical profile of a ferroelectric lamella [209]. They fabricated a sawtooth surface where domain walls move more easily up the shallow inclination than the steep one in the opposite direction. In an alternating field, domain walls thus effectively move in the same direction.

4. Multiferroics and the Magnetoelectric Effects

> We used to think that if we knew one, we knew two, because one and one are two. We are finding that we must learn a great deal more about 'and'.
>
> Arthur Eddington

In the most narrow definition, multiferroics are materials that simultaneously exhibit two or all three of the ferroic properties – ferromagnetism, ferroelectricity and ferroelasticity – in the same phase [214]. This means that, being also ferroelastic, most ferroelectric materials would be classified as multiferroic, but in practice they are not. Moreover, the definition has been broadened to include antiferroics, especially antiferromagnetism. While the coexistence of more than one ferroic order in a material constitutes a fascinating physical phenomenon from a fundamental point of view, it does not imply coupling between the order parameters. The induction of an electric polarisation by a magnetic field is known as the direct magnetoelectric effect, whereas converse magnetoelectricity describes the induction of a magnetisation by an electric field. In magnetoelectric multiferroics the order parameters are therefore coupled [7, 18, 27, 122, 215–217].

The interest in magnetoelectric and multiferroic materials is not limited to fundamental research on the complex mechanisms for their origin. These materials hold promise for devices with considerably improved performance when compared to current technologies. As the direct magnetoelectric effect allows transformation of a magnetic field into an electric voltage it could be used to replace existing magnetic field sensors that tend to have either low sensitivity (e.g. Hall sensors) or be bulky and expensive to operate (cf. SQUIDS). Using multiferroics exhibiting the converse magnetoelectric effect, technologies can be envisaged where data is

written electrically and read magnetically in non-volatile memories. Writing of information would therefore only require a low-power-dissipating voltage. This would constitute a significant advantage over magnetic field or current induced effects on magnetisation, and a reduction in power consumption by several orders of magnitude is expected [7, 218]. Magnetic reading of the stored data would alleviate the problems associated with fatigue in the destructive readout of ferroelectric memories. Unfortunately, deterministic and repeatable electric field induced magnetisation switching by 180° at room temperature remains elusive [216, 219–222].
Although ferroelectric and ferromagnetic materials exhibit many parallels, there are also significant differences. Whereas ferroelectricity in perovskites is linked to atomic displacements via the hybridisation of empty d states, ferromagnetism requires partially filled orbitals. In order for both order parameters to coexist and couple, a distinct mechanism needs to be present. As a consequence, single phase magnetoelectric multiferroics tend to show only weak coupling and mostly at low temperatures. These disadvantages can be circumvented by using heterostructures where different phases are artificially assembled. In this Thesis, I focus on electric field effects on the magnetisation and will therefore refer to magnetoelectric heterostructures as those that exhibit a converse magnetoelectric effect. Strictly speaking a multiferroic heterostructure could consist of a ferroelectric and a ferromagnetic film that are not coupled. As this is neither surprising nor interesting, I will assume that they also exhibit some form of correlation between order parameters. The coupling in heterostructures can be mediated via different mechanisms including strain transfer, charge modulation, and exchange coupling. The constituents of the heterostructures can be independently optimised to obtain optimal performance at room temperature [9, 27, 125, 216, 223].

4.1 Single Phase Multiferroics

On a fundamental level it can be noted that while ferroelectricity breaks space inversion symmetry, magnetism breaks time reversal symmetry. Magnetoelectrics therefore require the breaking of both symmetries. This condition is fulfilled by 58 of the 122 Shubnikov point groups. Multiferroics furthermore require the existence of a spontaneous electric polarisation and a spontaneous magnetisation which reduces the number of allowed point groups to 13. While this constitutes a considerable reduc-

tion in allowed symmetries it leaves a sufficient number of crystal structures that in principle allow for multiferroicity. Nonetheless, single phase multiferroics are rare. Although ferroelectricity is not possible in metallic ferromagnets there are plenty of magnetic insulators that are usually antiferromagnetic or ferrimagnets. The rarity of single phase multiferroics is hence difficult to account for. The most popular explanation is related to the empty d states of the small B ions that seem to be a requirement for the existence of ferroelectricity in many perovskite oxides (cf. Section 3.1). The hybridisation of these states with the 2p states of oxygen ions leads to the atomic displacements that cause ferroelectricity. Ferromagnetism on the other hand requires partially filled orbitals (cf. Hund's rules in Chapter 2) in order to create atomic moments that can then couple to form any type of magnetic order. It seems, however, that if the d shell of the B ions is partially occupied, the covalent bonding with the oxygen states is broken. This destroys the mechanism that results in an off-centring of the B ions and therefore eliminates the remanent polarisation [9, 10, 27, 125, 126, 215].

Type I Multiferroics

Ferromagnetism and ferroelectricity originate from different mechanisms in so-called type I multiferroics. The order parameters are usually associated with different subsystems of the sample. One example is $YMnO_3$ which is ferroelectric due to a rotation of MnO polyhedra up to a temperature of $T_C \approx 900$ K and antiferromagnetic below $T_N \approx 90$ K [224–227]. Since there are different origins for ferromagnetism and ferroelectricity, coupling is generally weak and the transition temperatures for both orders do not coincide. In general, the ferroelectric transition temperature is higher, while magnetic order – usually antiferromagnetism or helimagnetism – occurs only at cryogenic temperatures. A rare exception is $BiFeO_3$ [7, 228] which is probably the most heavily investigated single phase multiferroic. It exhibits both ferroelectricity and antiferromagnetism at room temperature with a Curie temperature $T_C \approx 1100$ K and Néel temperature $T_N \approx 640$ K. Although the ferroelectric polarisation of 0.9 C/m^2 is the result of charge ordering, it is associated with a rhombohedraly distorted perovskite lattice. The antiferromagnetic order is driven by a super-exchange interaction between Fe ions and mediated by oxygen ions to form a long-range spin-cycloid. The order parameters are coupled via the Dzyaloshinskii–Moriya interaction. $BiFeO_3$ is a complex multiferroic and is still being investigated [18, 229].

Type II Multiferroics

In type II multiferroics, ferroelectricity is a consequence of magnetic ordering into a helical phase due to a frustrated spin system. In this case, the ordering temperatures coincide and the magnetoelectric coupling is strong. The ferroelectric polarisation on the other hand is generally small. Moreover the ordering temperature is usually low. Examples of these materials include $MnWO_4$ [230, 231] and $DyMO_3$ [232]. The ordering of the spins into spirals such as screws, cycloids, and longitudinal or transverse cones breaks the spatial inversion symmetry and therefore allows for ferroelectricity to develop. The electric polarisation is thus a consequence of the magnetic order which can be classified into three types: Spin dependent p-d hybridisation occurs e.g. in $RbFe(MoO_4)_2$ [233]. Exchange striction is a symmetric spin exchange interaction that is the driving mechanism in, for example, $TbMn_2O_5$ [234]. Finally, the spin current model is an antisymmetric exchange interaction (that can be found e.g. in $TbMnO_3$ [18]), that is also known as the inverse Dzyaloshinskii–Moriya interaction. An extensive and instructive review by Tokura et al. [235] was published in 2014.

4.2 Heterostructures

Single phase multiferroics are rare, often difficult to synthesise, and show generally only weak coupling of small order parameters below room temperature. While research on these materials is still intense, composites have been shown to exhibit giant magnetoelectric couplings and large order parameters at and above room temperature. They are thus more likely to be integrated into devices. In such composites, the time and space reversal symmetries are broken at the interface between dissimilar components. The properties of the constituents and the interactions at their interface determine the properties of the composite [125, 215–217, 221, 236].

An electric field effect can be achieved by direct control of the magnetic properties via charge modulation. This effect can be made non-volatile when using a ferroelectric material as the origin of the electric field. Hybridisation between the constituents leads to a similar response. This effect is limited by the screening length in the ferromagnet and therefore extends only over 1 or 2 unit cells in metals or a few nm in dilute magnetic semiconductors. Alternatively, coupling can be mediated via a third

order parameter. When using a multiferroic such as $BiFeO_3$ or $YMnO_3$ that is simultaneously ferroelectric and antiferromagnetic, exchange coupling with a ferromagnetic film can be engineered. Again, the effect is limited to a layer at the interface that is a few nm thin. Finally, elastic interactions between a ferroelastic ferroelectric or a piezoelectric material and a magnetostrictive film are of much longer range and can operate at length scales over 100 nm [27, 125, 144, 237, 238].

Multiferroic and magnetoelectric composites can be engineered in different forms. In particulate composites, magnetic particles are diluted in a ferroelectric matrix [239–241], while in vertical composites nanorods of one phase are embedded in a matrix of the other phase [242, 243]. Both approaches rely on self-assembly, which considerably limits the choice of materials and complicates fabrication. Moreover, these composites tend to be poor insulators which limits the strength of electric fields that can be applied. Due to a lattice mismatch and different expansion coefficients of the constituents, cracks and dislocations can lead to poor coupling and a deterioration of properties with electric field or thermal cycling. Finally, as one phase is embedded in another phase, the coupling at opposite interfaces can compensate leading to a small overall coupling. Most of these disadvantages can be avoided by using layered heterostructures. The coupling tends to be large, and significant electric field strengths can be applied. Furthermore, the fabrication tends to be relatively simple as films of one phase can be deposited onto films of the other phase using various deposition techniques. An even simpler method consists of cementing both constituents together using an epoxy [27, 216, 217, 236, 238].

4.2.1 Strain Transfer

Magnetoelectric coupling may be achieved by imposing strain on a magnetic thin film. The strain can be generated by a piezoelectric substrate or thin film. The piezoelectricity of most ferroelectric materials can also be used to impose volatile strains [220, 244, 245]. Ferroelectric-ferroelastic materials also exhibit domains and different strain states at remanence. For example, in the tetragonal phase of $BaTiO_3$ the lattice elongation can point out-of-plane in c-domains and in two orthogonal in-plane directions in a_1- and a_2-domains. Three different remanent states can therefore be obtained leading to a non-volatile (bi-stable) strain [246, 247].

The application of an electric field changes the strain state of a ferromagnetic film in contact with the piezoelectric or ferroelectric component

of a heterostructure [220, 238]. The deformation of the ferromagnet can lead to magnetic phase transitions, changes in the saturation magnetisation, the Curie temperature, and the coercive field. Most importantly, the symmetry, orientation, or strength of the magnetic anisotropy can be changed. In order for this converse magnetoelectric effect to work, the electric field induced strain must be larger than the strain that can be created by the ferromagnetic component. As calculated in Publication II, the strain imposed by most ferromagnetic films is orders of magnitude smaller than the strain associated with a ferroelectric lattice elongation [27, 220, 245, 248, 249].

Piezoelectric Substrates

Commonly used piezoelectric materials are PMN-PT [237, 249–254] or PZN-PT [255]. The volatile strain they impose traces a "butterfly" curve as a function of applied voltage and, depending on the material and the crystal orientation, the strain in the surface plane of the piezoelectric can be uniaxial [237, 248–251, 255–260], or biaxial [252–254, 261]. Depending on the polarity of the electric field, strains are compressive or tensile [238]. For the strain imposed on the ferromagnetic component of the heterostructure to have an effect, the stress inside the film needs to be intimately coupled to the magnetic properties. This is realised using materials exhibiting large magnetoelastic effects. The strain imposed on the ferromagnet can most notably change the in-plane anisotropy of the magnetic thin film via inverse magnetostriction (cf. Section 2.4.4). In order for this mechanism to be effective, the strain induced anisotropy must dominate the intrinsic anisotropies in the ferromagnet. This is most easily achieved using polycrystalline or amorphous materials where intrinsic anisotropy contributions are usually weak. This allows, for example, reversible tuning of the strength of a uniaxial anisotropy in Fe_3O_4 or CoFeB using piezoelectric actuators [249, 255]. Strain effects can also be used to tune the strength of perpendicular magnetic anisotropy with electric fields [261, 262].

More importantly, it is possible to rotate the anisotropy axis of the material. Since the anisotropy creates an axis of preferred magnetisation orientation (instead of a vector), only magnetisation rotations of up to 90° are possible [220, 248]. Using piezoelectric actuators the volatile rotation of an in-plane uniaxial anisotropy axis by up to 90° has been demonstrated for a plethora of ferromagnets such as NiMnSb, CoFeB, Fe_3O_4, or Ni [250, 257, 258, 260, 263, 264]. It is also possible to drive a strain in-

duced Spin Reorientation Transition between out-of-plane and in-plane anisotropy as described theoretically by Pertsev [265, 266] and shown experimentally [267].

Concepts exist to reorient the magnetisation by more than 90° up to 180°, although the final orientation of the magnetisation depends on history, and not only on the direction of the applied electric field. The application of a cycle of electric field induced uniaxial strains to a film with cubic magnetocrystalline anisotropy can make the magnetisation rotate between the four possible cubic anisotropy directions if the induced uniaxial anisotropy is collinear with neither of the cubic anisotropy axes [268]. The cubic anisotropy can also be induced using the shape anisotropy of flower-shaped single domain nanomagnets [269] or square nanomagnets [270] that are more easy to pattern. Alternatively, strain induced precession of the magnetisation can dynamically lead to full magnetisation reversal [268]. Such a reversal was demonstrated locally in out-of-plane magnetised Ni/$BaTiO_3$ heterostructures [271]. Here, polycrystalline $BaTiO_3$ is used as a piezoelectric. Applying an electric field, the perpendicular magnetic anisotropy is reduced and the magnetisation starts rotating in-plane through precessional motion. By removing the electric field at the correct moment the perpendicular anisotropy can be reintroduced when the magnetisation has crossed the equatorial plane, and the magnetisation is forced back out-of-plane but reversed with respect to its initial orientation. Such a behaviour without the concurrent use of magnetic fields has also been demonstrated using phase-field simulations [272].

The resonance frequency of the magnetisation of a material depends on the effective field it experiences. This effective field includes a contribution from the magnetic anisotropy. A change of the anisotropy with strain can therefore be used to tune the Ferromagnetic Resonance Frequency (FMR) of a magnetic film in a magnetoelectric heterostructure with electric fields. This was demonstrated for various films such as NiMnSb [257], Fe_3O_4 [249, 264], CoFeB [255, 273], FeGaB [273, 274], FeCoTa [275], and insulating yttrium Iron garnet (YIG) [276].

Electric field control of magnetisation in strain-coupled heterostructures furthermore allows for electrical control of magnetic phases. For example, it was demonstrated around room temperature, that superparamagnetic Ni nano-particles can be reversibly turned into single-domain ferromagnets through an electric field induced shift of the blocking temperature by 40 K [251].

A mechanism distinct from inverse magnetostriction can lead to strain induced modifications of magnetic properties in rare earth manganites ($Re_{1-x}A_xMnO_3$, where Re is a rare earth and A an alkaline metal), such as $La_{1-x}Sr_xMnO_3$, where ferromagnetism originates from the double-exchange interaction between Mn ions. Strain can strongly affect magnetic properties by changing the orbital occupation of Mn and therefore the anisotropy of the system, or by tuning the length and angle of the Mn-O-Mn bond. In the latter case, electronic properties are affected [220, 237, 244,245,254,277]. The application of strains using piezoelectric materials can tune both the remanent and saturation magnetisation [252, 254], the resistivity [244], and the Curie temperature [254, 278] using an electric field.

In dilute magnetic semiconductors such as (Ga,Mn)As, spin polarised holes mediate the ferromagnetic coupling between Mn atoms resulting in strong spin–orbit coupling and thus a sensitivity of the magnetic anisotropy to strains [256, 279, 280]. Volatile and reversible rotation of the anisotropy axis has consequently been demonstrated in these materials, too [256,259, 279]. Unfortunately, the Curie temperature of these materials is generally well below room temperature.

Ferroelectric Substrates

The changes in the magnetic properties can be made non-volatile by using a ferroelectric such as $BaTiO_3$ to impose strains. Although a rotation of the anisotropy axis is not always explicitly demonstrated in most publications, it is the only logical explanation for the effects observed macroscopically [246, 281, 282].

In early investigations, using strain associated with the structural phase transitions of $BaTiO_3$ has been a popular method to induce changes in the magnetic anisotropies of adjacent ferromagnetic thin films [27, 220]. The changes are usually measured as abrupt jumps in the coercivity or magnetisation as a function of temperature in magnetic films such as FeCo [283], Ni [283], Fe [281, 284], $CoFe_2O_4$ [285], Fe_3O_4 [286, 287], or Sr_2CrReO_6 [288]. In epitaxial Fe/$BaTiO_3$ heterostructures, switching was demonstrated between cubic anisotropy associated with the tetragonal phase and uniaxial anisotropy induced in the orthorhombic phase [289, 290]. In Fe_3O_4, uniaxial anisotropy that is induced at the ferroelectric phase transition can induce a Spin Reorientation Transition [291]. Finally, the phase transitions of $BaTiO_3$ have also been used to tune the properties of rare earth manganites [244, 292].

The application of an electric field to ferromagnetic/ferroelectric heterostructures allows for the non-volatile transformation of magnetic properties. For example, non-volatile switching between an in-plane anisotropy and perpendicular magnetic anisotropy was demonstrated, but only locally, using Ni films on $BaTiO_3$ [293]. Using a ferroelectric substrate poled in-plane and out-of-plane, reversible switching between two distinct remanent states with e.g. different Curie temperatures is also possible in rare earth manganites [277].

Domain Pattern Transfer

Many of the macroscopic results on electric field control of magnetisation in $BaTiO_3$-based heterostructures can only be rationalised when assuming that different ferroelectric domains affect the magnetisation differently on a microscopic scale. This is in contrast with the uniform strain imposed by piezoelectric substrates. The magnetoelastic anisotropy in a ferromagnetic thin film is modulated by the ferroelastic domains of $BaTiO_3$ via interfacial strain transfer and inverse magnetostriction. Transfer of strain from the tetragonal lattice of a $BaTiO_3$ substrate can occur during thin film growth [294–298],[III], during cooling down through the paraelectric-to-ferroelectric phase transition [299–301],[VII], or after the application of an electric field [301]. If the strain induced anisotropy dominates over the magnetocrystalline anisotropy, and the exchange and magnetostatic interactions between domains, domain correlations can be obtained.

Simultaneous imaging of ferroelectric and ferromagnetic domains, and therefore definitive proof of the correlation between the domains was first demonstrated by Lahtinen et al. [294, 295]: Both types of domains were

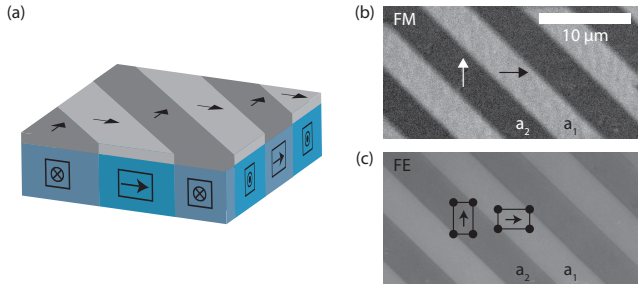

Figure 4.1. (a) Sketch of a multiferroic CoFe/$BaTiO_3$ heterostructure exhibiting domain pattern transfer. The lattice elongation associated with the a_1–a_2 stripe domain pattern is imprinted into the ferromagnetic film via interfacial strain transfer and inverse magnetostriction. Magnetic stripe domains with alternating perpendicular uniaxial in-plane anisotropies are obtained. Full pattern transfer is demonstrated by imaging both ferromagnetic (b) and ferroelectric (c) contrast at the same location in a MOKE Microscope.

imaged at the same time in a Magneto-Optical Kerr Effect (MOKE) Microscope as shown in Figure 4.1. MOKE is used to resolve ferromagnetic domains while birefringent contrast is used for imaging ferroelectric domains. It is revealed that the magnetisation direction in CoFe films on a $BaTiO_3$ substrate exhibiting a_1–a_2 stripe domains rotates by 90° between ferromagnetic domains on a length scale of a few μm. These results were later confirmed by phase-field simulations [302–304]. Meanwhile, domain pattern transfer has been observed with the same method for Fe [III] and CoFeB [299],[VII] thin films and Cu/Ni multilayers [VI] deposited onto $BaTiO_3$ substrates.

Correspondence between the orientation of the electric polarisation and magnetic moment has also been obtained using $BaTiO_3$ substrates and films of $LaSrMnO_3$ [297], Ni [293, 301], $CoFe_2O_4$ and $NiFe_2O_4$ [296], and NiFe [300]. These studies combine Piezoresponse Force Microscopy (PFM) and X-ray Linear or Circular Dichroism based Photo-Electron Emission Microscopy (XPEEM) to image the electric and magnetic domains separately.

In earlier studies, electric field induced changes of the magnetic state in $Ni/BaTiO_3$ [246] and $Fe_3O_4/BaTiO_3$ [247] heterostructures were explained by the presence of differently strained regions depending on the underlying ferroelectric-ferroelastic domains. X-ray diffraction on a $LaSrMnO_3$/ $BaTiO_3$ heterostructure confirms the presence of 90° domains whose relative population can be altered with an applied electric field [305]. These results do not however demonstrate a one-to-one correlation of domains in different ferroic phases.

In epitaxial $FeRh/BaTiO_3$ heterostructures the spatially modulated strains imposed by the substrate can lead to domains with different magnetic phases. Depending on the underlying ferroelectric-ferroelastic domain, the transition temperature between the ferromagnetic and antiferromagnetic phase is shifted by 25 K. Consequently, when the temperature is kept constant, electric field induced changes of the magnetic phase are possible [298, 306].

4.2.2 Charge Modulation and Hybridisation

Magnetic properties are intimately connected to the motion of charges (electrons or holes), e.g. in metallic ferromagnets (cf. Section 2.1.2), dilute magnetic semiconductors [279,280,307,308], or manganites [220,245, 277]. It can therefore be expected that a change in the charge carrier den-

sity induced to screen an external electric field will affect the magnetic properties of the ferromagnet. Of course this direct electric field effect will only extend over the screening length of the material, which is one or two unit cells for metallic films and a few nm for semiconducting ferromagnets. Nonetheless, it can be used to electrically control ferromagnetic films that are thicker than the screening length, typically a few nm. In order to enhance the field effect, a gate dielectric can be used, as the induced charges scale with the dielectric constant [309]. A large bistable electric field can also be created by using a ferroelectric material as the dielectric [139, 156]. As a result, a magnetoelectric effect is present even in the absence of an external electric field. Moreover, an electric field effect due to chemical bonding at the interface between the ferroelectric and the ferromagnetic component will generally be present. In multiferroic heterostructures based on the depletion or accumulation of charges, electric fields can induce changes in the magnetic moment, the anisotropy, and the exchange interaction [125, 144, 220].

In metallic ferromagnets the screening of electric fields by charge accumulation or depletion shifts the Fermi level in the spin-split electron bands (cf. Section 2.1.2). The screening is therefore spin dependent and will affect the magnitude of the magnetic moment. Theoretical calculations have shown effects in free-standing films of the ferromagnetic 3d transition metals [310] and in half-metals [311]. As it is difficult (or impossible) to produce such free-standing films the electric field is often applied across a dielectric, which also enhances the field-effect, e.g in a Fe/MgO heterostructure [309]. When a ferroelectric dielectric is used, e.g. in a Fe/$BaTiO_3$ multilayer [312], a change in the hybridisation between Ti, Fe, and oxygen orbitals upon polarisation reversal is caused due to the displacement of Ti ions. This change in chemical bonding is superimposed to the direct field effect. The hybridisation can also lead to the induction of a ferromagnetic moment in $BaTiO_3$ turning the ferroelectric into a multiferroic at the interface [313].

The change of occupancy of band states does not only affect the magnitude of the magnetisation, but also the quenched orbital momenta of the electrons. A direct electric field effect on the magnetocrystalline anisotropy can therefore be expected. The surface anisotropy is especially affected leading to a modulation of a perpendicular magnetic anisotropy [309, 310, 314, 315]. A switching of the easy axis between in-plane and out-of-plane is also possible [316]. Electric field tuning of the competition between in-

plane and perpendicular anisotropy in (Ga,Mn)As/(Ga,Mn)(As,P) bilayers can be used to rotate the direction of the magnetisation [317, 318].

In dilute magnetic semiconductors such as (Ga,Mn)As, (In,Mn)As, or (Zn,Mn)Te, ferromagnetic coupling between Mn ions is mediated by spin polarised holes [280, 307, 319]. A modulation of the charge carrier density will hence affect the exchange interaction. Experimentally this effect is measured as a change in the Curie temperature or the coercive field [320–322].

In rare earth manganites, ferromagnetism originates in the double-exchange interaction between Mn ions, involving the hopping of electrons. Moreover, the manganites exhibit a rich phase diagram [323]. Tuning of the charge carrier density is expected to affect the strength of the exchange interaction and the phase of the magnetic material. For example, the phase of $La_{0.8}Sr_{0.2}MnO_3$ or $La_{0.85}Ba_{0.15}MnO_3$ in a manganite/PZT heterostructure can be altered between ferromagnetic and antiferromagnetic depending on the polarisation of the ferroelectric [324–326].

Dynamic switching of the anisotropy axis between out-of-plane and in-plane via charge effects has also been used in order to switch the magnetisation by 180° by using nanosecond voltage pulses [327]. The mechanism by which this is obtained relies on the same precessional motion as was discussed above in the context of strain coupling.

When ferroelectric layers are used in a heterostructure, both charge and strain effects can be present. It has been demonstrated that for thin magnetic films the effect of charge accumulation dominates, while above a certain material-dependent thickness strain transfer dictates the properties of the heterostructure [328, 329]. For an intermediate film thickness both mechanisms can coexist [330].

4.2.3 Exchange Coupling

The third mechanism by which the magnetisation can be electrically controlled in heterostructures takes advantage of single phase multiferroics (e.g. $YMnO_3$, $LuMnO_3$, $BiFeO_3$) and magnetoelectrics (e.g. Cr_2O_3) exhibiting coupling of electric order to antiferromagnetism. The exchange bias effect (see Section 2.4.6) can then be used to couple the antiferromagnetic moments to a ferromagnetic layer. Naturally this coupling extends over only a few nm at the interface [27, 144].

The first demonstrations of electric field control of exchange bias were performed on (Co/Pt)/Cr_2O_3 multilayers that exhibit perpendicular exchange

bias. During cooling through the antiferromagnetic Néel temperature, the direction of the exchange bias can be set by choosing the direction of an applied electric field parallel or anti-parallel to the simultaneously applied magnetic field [331,332]. Later it was shown that the exchange bias field could be switched isothermally by applying a constant magnetic field and reversing an electric field [333].

The application of an electric field to a NiFe/$YMnO_3$ heterostructure can suppress the existing exchange bias [224]. In NiFe/$LuMnO_3$ the exchange bias can be switched with an electric field [334]. Both effects have been attributed to the coupling and decoupling of antiferromagnetic and ferromagnetic domain walls across the interface.

Most heterostructures taking advantage of exchange bias rely on $BiFeO_3$ as the antiferromagnetic ferroelectric [7]. Here, antiferromagnetic domains are coupled to their ferroelectric counterparts and can be controlled using electric fields [335]. The exchange bias effect depends on the ferroelectric domain wall configuration in $BiFeO_3$. Uncompensated spins in 180° [170] and 109° [336,337] domain walls lead to the observation of an exchange bias, while the presence of 71° domain walls [336,338] results in an enhancement of the coercive field, but no shift of the hysteresis curve. The latter effect originates in the coupling of the ferromagnetic film to the canted moment of $BiFeO_3$ caused by the Dzyaloshinskii–Moriya interaction. Exchange bias has also been demonstrated in $La_{1-x}Sr_xMnO_3$/$BiFeO_3$ heterostructures [339, 340]. However, such a heterostructure has been used to demonstrate that the coupling between $BiFeO_3$ and a ferromagnetic layer is not necessarily mediated by exchange coupling. You et al. [341] demonstrated that the insertion of a non-magnetic $SrTiO_3$ layer between the components of their heterostructure does not alter the coupling, although exchange bias between the layers is not possible any more. In this case the coupling is mediated by strain transfer, since $BiFeO_3$ also exhibits a lattice elongation associated with the polarisation.

Domain Pattern Transfer

In $BiFeO_3$, the antiferromagnetic domains have been shown to be coupled to their ferroelectric counterparts allowing for their control with electric fields [335]. Coupling of the antiferromagnetic domains to an adjacent ferromagnetic CoFe film leads to an imprinting of the ferroelectric domain structure [338,342]. The magnetisation direction rotates by 90° between domains that are only a few hundred nm wide. The orientation of the magnetisation can be reversibly switched by 90° between two states us-

ing an electric field only. Again, resolving ferromagnetic and ferroelectric domains was done separately using PFM and XPEEM, by imaging first magnetic domains and then the ferroelectric ones after removal of the magnetic thin film. Simultaneous high resolution imaging was eventually obtained using Spin Polarised Scanning Electron Microscopy (SEMPA) to image the magnetic domains and Back-Scattered Electron contrast to image ferroelectric domains in the same microscope [343]. As mentioned above, strain can also allow for coupling in these heterostructures and lead to imprinting of ferroelectric stripe domains from a $BiFeO_3$ substrate into a $LaSrMnO_3$ thin film [341].

As in strain-coupled heterostructures, the results presented above for $BiFeO_3$ based heterostructures have demonstrated magnetisation switching by only up to 90°. The 71° switching in domains of $BiFeO_3$ is perceived as a 90° in-plane rotation of the electric polarisation. It was suggested that, because the rotation of polarisation can occur in opposite directions – therefore leading to a full reversal of the macroscopic polarisation – the net magnetisation of an exchange coupled ferromagnetic film could also be rotated by 180° [338].

Microscopic deterministic reversal of the magnetisation with an electric field was recently demonstrated at room temperature within coupled domains of CoFe/$BiFeO_3$ heterostructures [344]. Unfortunately the coupling between adjacent domains, and the fact that irreversible oxidation of the CoFe film limits the number of switching events to 3, hampers the use of these results in practical applications.

4.2.4 Electric Field Induced Ion Migration

Electric field induced ion migration – usually of oxygen ions – has recently attracted interest due to the ability to demonstrate strong magnetoelectric coupling. In metal/oxide heterostructures an applied voltage can induce the migration of oxygen to or away from the interface and even drive the oxidation of the ferromagnet. Interestingly, this effect can be reversible and non-volatile, and may exhibit very large magnetoelectric coupling effects [345–348].

As Couet et al. [349] have demonstrated in Fe/$BaTiO_3$ and Fe/$LiNbO_3$ heterostructures, the ferromagnetic metal will usually be oxidised at the interface already in the as-deposited state and when large enough fields are applied the thickness of the oxidation layer will increase irreversibly. This will generally have a deleterious effect on the magnetoelectric coupling, as

for example in the exchange coupled CoFe/$BiFeO_3$ heterostructures mentioned in the previous Section.

4.3 Coupling of Ferroic Domain Walls

As explained above, coupling between ferroelectric and antiferroelectric domain walls has been observed in single phase multiferroics such as $YMnO_3$ [215, 350, 351] and $BiFeO_3$ [335]. The coupling, and decoupling, of these domain walls is crucial for the switching of the exchange bias with an electric field [334]. In Fe_3O_4 below the Verwey transition strong coupling between ferroelectric and 90° ferrimagnetic domain walls is mediated via strain [352, 353].

In type-II multiferroics (cf. Section 4.1) an electric polarisation can originate from the spatial inversion symmetry breaking of the magnetic order. Such symmetry breaking is also present in Néel walls and their magnetoelectric and multiferroic properties have been predicted theoretically [354, 355] and demonstrated experimentally [356–358] in insulating Iron garnet films. The emergence of an electric dipole for both Néel and Bloch walls in rare earth Iron garnets was recently predicted [359].

Electric Field Control of Magnetic Domain Wall Motion

The presence of a polarisation in Néel walls can be used to stabilise their chirality with an electric field and thus delay the onset of the Walker breakdown [360]. However, most demonstrations of an electric field effect on the motion of magnetic domain walls take advantage of the effect of anisotropy modulations on their propagation velocity.

For small wall velocities the motion is governed by domain wall creep that proceeds via thermally activated depinning from disorder induced pinning barriers. The pinning strength scales with the strength of the anisotropy which can be tuned electrically [361, 362]. Volatile and reversible electric field tuning of magnetic field driven domain wall motion was demonstrated in perpendicularly magnetised CoFeB [262] and Pt/Co/Pt [363] films in contact with a piezoelectric transducer. The tuning of the current-driven domain wall motion in a perpendicular magnetised GaMnAs/GaAs ferromagnetic semiconductor was attributed to the piezoelectrically controlled anisotropy tuning the internal structure of magnetic domain walls [364].

The perpendicular anisotropy can also be altered in a field effect device, leading to tuning of the propagation velocity of magnetic domain walls [361,365]. With patterned gate electrodes, volatile and reversible pinning sites for magnetic domain walls can be created in order to control magnetic field or electric current driven motion [366]. Charging and the oxidation of the interface between a gate dielectric and the magnetic film can both lead to the tuning of the domain wall velocity and to pinning [367]. Finally, strong voltage control of domain wall motion and pinning has been demonstrated by Bauer et al. [362, 368, 369] in Pt/Co/GdO_x heterostructures, where perpendicular magnetic anisotropy is caused by interfacial Co oxidation. GdO_x exhibits high ionic mobility which can be used to reversibly change the oxidation state at the interface with Co. Large electric fields lead to switchable remanent oxidation states, but the effect becomes irreversible when the applied voltages are too large. The velocity of magnetic field or electric current driven magnetic domain walls can thus be tuned by electric fields and tunable pinning is possible. However, as the mechanism relies on the tuning of the anisotropy strength in the creep regime it becomes ineffective at higher velocities. Moreover, domain wall motion is driven by magnetic fields or electric currents which are associated with a large power dissipation.

Electric Field Driven Domain Wall Motion

In order to envisage domain wall devices with ultra-low power consumption, magnetic domain walls need to be driven controllably with an electric field. The aforementioned Néel domain walls in Iron garnet films that are associated with an electric polarisation can be displaced in an electric field gradient [356–358]. In order to achieve the field gradient, a voltage is applied to a tip in contact with the film. Domain walls can then be moved reversibly until they reach an equilibrium position corresponding to the applied field. This mechanism is independent of the chirality of the domain wall, but the direction of motion depends on the polarity of the electric field. The constraints imposed by the requirement of applying inhomogeneous fields, and the volatility of the motion do however seriously limit the potential of this mechanism for practical applications. In the experiments that were performed, domain walls were only manipulated locally, in the vicinity of the charged tip.

The most common route to induce magnetic domain wall motion with electric fields is the use of the competition of a strain induced anisotropy with magnetocrystalline or shape anisotropies. The flux closure patterns in

squares [248] or L-shaped [370] nanopatterned ferromagnetic films coupled to a piezoelectric material can be altered when an electric field induced anisotropy is created. The change of pattern involves the motion of domain walls, but this displacement is very small and only of limited relevance. In extended films the 90° switching of the magnetisation using electric fields can proceed via uncontrolled domain wall motion [371]. The motion of pre-existing domain walls can also be induced, but while 90° domain walls are affected by the electric field induced anisotropy, 180° domain walls are not [372]. Similarly, reversible local curving, bending, and branching of pre-existing stripe-domain patterns in a Ni/PZT heterostructure was demonstrated to proceed via domain wall motion when in-plane strains develop as a result of the application of an electric field [373]. The demonstrated control of domain walls is not only volatile but occurs only in certain random locations.

An interesting approach to electric field induced domain wall motion utilises the formation of an "onion" magnetisation state in ferromagnetic ring structures where two 180° domain walls are initialised on opposite sides [374, 375]. Via a piezoelectric, two orthogonal uniaxial magnetic anisotropies can be imposed on the ferromagnet depending on the polarity of the electric field. Energy minimisation dictates that the domain walls align with this anisotropy and the domain walls are moved by changing their position in the ring by 90°.

All of the approaches presented thus far are only of little interest for implementation in practical devices because the demonstrated magnetic domain wall motion is either local, small, irreversible or volatile. These disadvantages could be overcome if localised strains from a piezoelectric film were imposed on a ferromagnetic nanowire [376]. Simulations show that by using a series of electrical contacts, a potential well for a magnetic domain wall can be created and propagated along the nanowire. The domain wall would then follow this potential that moves like a wave through the nanowire. This mechanism has thus been described as the "surfing" of a domain wall on a "wave" created by the moving potential gradient. While this approach would allow moving several domain walls in the same direction in a magnetoelectric shift register, it requires too many nanoscale electrical contacts to be of practical interest.

As will be demonstrated in Chapter 6, magnetic domain walls are strongly coupled to ferroelectric domain boundaries when the ferroelectric stripe domain pattern in $BaTiO_3$ is imprinted into a ferromagnetic thin film

(Figure 4.1). For $BaTiO_3$ substrates exhibiting an a_1–a_2 domain pattern, phase field simulations show that the application of an in-plane field along the polarisation in one of the domains leads to the motion of ferroelectric domain boundaries, and of the magnetic domain walls coupled to them [304]. Unfortunately, the application of in-plane electric fields of significant magnitude is challenging, especially when a metallic ferromagnet is used. In Chapter 6, I will demonstrate how reversible electric field driven magnetic domain wall motion can be achieved experimentally in a multiferroic heterostructure. The electric field is applied across a $BaTiO_3$ substrate exhibiting an a–c stripe domain pattern and drives magnetic domain walls that are pinned onto their ferroelectric counterpart. This novel driving mechanism functions without the concurrent use of spin polarised currents or magnetic fields. The induced motion is fully controlled and reversible, and the velocity of domain walls increases exponentially as a function of electric field.

5. Methods

A process I found troublesome
and excessively tedious.

John Kerr

The results presented in Chapter 6 are obtained on multiferroic heterostructures consisting of a $BaTiO_3$ substrate and various ferromagnetic 3d transition metal films. Depending on the material used, the films are grown at either room temperature or elevated temperatures using Magnetron Sputtering, Electron Beam Evaporation, or Molecular Beam Epitaxy. Characterisation is accomplished by Magneto-Optical Kerr Effect (MOKE) microscopy and Scanning Electron Microscopy with Polarisation Analysis (SEMPA). Numerical and analytical Micromagnetic modelling supports and expands upon the experimental results.

5.1 DC Magnetron Sputtering

In Physical Vapor Deposition (PVD) processes material is vaporised from a liquid or solid source or target in the form of single atoms or small clusters of atoms. These atoms transit a vacuum – or low pressure – chamber, and impinge on the substrate where they condense to form a film. In Sputter Deposition (usually referred to as Sputtering) the target is bombarded by energetic particles that lead to the ejection of target material due to momentum transfer. The particles are usually ions of a noble gas in a plasma that are accelerated by an electric field towards the target. The larger the mass of the bombarding particle, the higher the energy and momentum transfer. Frequently, relatively affordable Argon (Ar) is used as the inert gas. The impact of gas ions onto the target transfers momentum to the surface or near-surface atoms and this leads to a cascade of atom collisions deeper into the material. During the displacement of the atoms,

particles can rebound and some surface atoms may obtain enough energy and momentum to overcome the surface binding energy and be ejected from the target.

Noble gas ions are created in a plasma generated by applying a voltage between an anode (usually the grounded substrate or chamber walls) and a cathode (normally the negatively biased target). The plasma is conducting and the potential drop is therefore confined to the vicinity of the electrical contacts. Ions are accelerated towards the target (cathode), leading to Sputtering. Emission of secondary electrons from the cathode due to the ion bombardment leads to additional ionization of gas atoms and thus helps sustain the plasma. In a basic DC sputtering setup the electrons are accelerated away from the cathode and their ability to sustain the plasma is limited. In a Magnetron Sputtering system, magnetic fields (usually from permanent magnets) are used to alter the trajectory of the electrons and confine them to a region close to the target. This localisation yields a path length of the electrons in the plasma that is several orders of magnitude higher. Consequently, a higher plasma density can be obtained at lower gas pressures, thus increasing the deposition rates. However, the confinement of the plasma leads to a non-uniform utilization of the target and the magnets need to be water cooled.

The energy of the impinging ions is in the range from 10 to 1000 eV with a peak in distribution around $10-50$ eV. As a result of these large energies high deposition rates (of the order of nm/s) of virtually all metals are possible. Unlike Electron Beam Evaporation (Section 5.2) and Molecular Beam Evaporation (Section 5.3), Sputtering can easily be used to deposit not only elemental materials but also alloys from a single target. As material is removed from the target in a layer-by-layer process, the composition of the target and the sputtered thin film are generally very close.

In Sputtering, the distance between the target and the substrate is short and it is generally difficult to use thickness monitors such as quartz crystals within the deposition chamber. However, the deposition rate is constant with time and can easily be calibrated. This is done by growing a film for a set time and measuring its thickness using small angle X-ray Diffraction. The deposition time can be controlled accurately using a mechanical shutter. Moreover, the shutter can be kept closed in the beginning of the sputtering process in order to remove contaminations such as oxide layers from the target [33, 377–379].

5.2 Electron Beam Evaporation

Electron Beam Evaporation is a vacuum deposition technique where material is evaporated from a crucible by heating it with an electron beam. Heating with an electron beam is preferred over resistive heating for evaporation at high temperatures ($> 1500°C$), which is required e.g. for metals. The electrons are extracted from a filament biased at the electron acceleration potential. The filament is placed underneath the crucible and the electrons are deflected and focused onto the target material by a combination of magnets. Heating to the vapour pressure of the target material leads to its melting and evaporation from the source. Deposition onto a substrate is then obtained by placing it in direct line-of-sight of the evaporation source. As the material in the source is molten, the crucible is positioned below the substrate which is mounted upside-down. In order to reduce radiative heating of the substrate, the distance to the source needs to be significant, thus reducing the material yield.

As different materials in an alloy have different temperature vs. vapour pressure phase diagrams, evaporation from alloy sources is difficult. The material with the lower melting point or higher vapour pressure will be deposited first, leading to a gradient in the film composition over time. Alloys can be obtained through co-evaporation from several sources or in a less controlled way by considering that the composition of a composite evaporated from a single source will be proportional to the relative vapour pressures of the constituents, at least when none of the components are exhausted.

Electron Beam Evaporation is a non-equilibrium process and the deposition rate can be adjusted by the electron beam emission current. Calibrating the deposition rate is virtually impossible and flux monitors are used to determine the obtained film thickness. The most common monitors rely on piezoelectric quartz crystals. Their resonance frequency changes when mass (the deposited material) is added which allows determination of the deposition rate in real time. Ideally, the rate monitor is placed on the same height as the substrate. Otherwise, a correction by the Tooling factor is made to account for the different deposition rates at various distances to the source [377, 378, 380].

5.3 Molecular Beam Epitaxy

"In essence, MBE [Molecular Beam Epitaxy] is little more than a UHV [Ultra High Vacuum]-based evaporation method. In practice, it is a material deposition technique capable of predictably and reproducibly yielding material ... with unprecedented control over ... the composition and doping of the structure .... Some of these attributes are intrinsic to the MBE process, e.g., slow growth rates and low deposition temperatures. Others, such as material quality and purity, rely on the technology employed" [380]. MBE relies on the thermal creation of low energy atomic beams for each material that is deposited. The use of a resistively heated Knudsen cell as a source results in a highly controlled growth from a target material that is in thermodynamic equilibrium between the liquid and the vapour phase [381, 382]. Combined with mechanical shutters this results in an unrivalled control of epitaxial thin film growth of high purity. Multilayers can be grown with atomically sharp interfaces. This of course requires extremely good vacuum conditions of the order of 10^{-10} mbar. For materials that require higher deposition temperatures, electron beam heated evaporation cells are used. The quality of the deposition is also guaranteed by in-situ monitoring of the growth with thickness monitors and a variety of electron-based characterisation methods such as Reflection High Energy Electron Diffraction (RHEED). Although MBE was initially developed for the growth of semiconductors it has been adapted for metals such as Fe [282,284,289,290],[III,V] or Ni/Cu multilayers [VI] that are of interest in this Thesis. The quality of MBE grown films can be excellent, but requires significant optimisation when compared with other deposition techniques and the prerequisites for its use (e.g. material requirements and ultra high vacuum components) result in an expensive deposition technique. Moreover, an optimal generic MBE system does not exist and the configuration needs to be tailored for a limited range of source materials [33, 157, 245, 378, 380, 382].

5.4 MOKE Microscopy

Imaging of ferromagnetic and ferroelectric domains with an information depth of the order of a few tens of nm can be obtained using a MOKE Microscope. It takes advantage of the birefringent properties of ferroelectrics to image their domains while the Magneto-Optical Kerr Effect (MOKE) is used to image ferromagnetic domains. As polarised light travels through a material (the microscope lens) in a magnetic field, the Faraday effect also needs to be taken into account. All these effects will be discussed below.

The microscope used for the measurements presented in this Thesis is based on an optical reflection microscope from Zeiss modified by Evico Magnetics for MOKE measurements. The light can be made to travel through a slit in order for it to impinge on the sample surface at an angle. Polarisers are inserted into the light beam path before and after the sample. The latter is referred to as the analyser. A CCD camera records the resulting images of the sample surface. Interchangeable electromagnets allow for the application of in-plane and out-of-plane magnetic fields, and a special sample holder was designed in order to apply out-of-plane electric fields to the sample under investigation. A detailed discussion of MOKE microscopes in the context of magnetic domain imaging is given in the book by Hubert and Schäfer [20] and in a recent review article [383], in which a vast amount of applications of MOKE microscopy is described.

5.4.1 The Magneto-Optical Kerr and Faraday Effects

The Kerr effect [384, 385] changes the polarisation or intensity of light that is reflected from a magnetic material. Both the longitudinal and polar effect yield a rotation and ellipticity of linearly polarised light. The Faraday effect describes the corresponding situation for light transmitted through the material. The transverse Kerr effect results in a change of the intensity and does not have an equivalent Faraday effect.

The longitudinal Kerr effect is sketched in Figure 5.1(a) and requires the light impinging on the sample at an angle. The change in polarisation is proportional to the projection of the in-plane magnetisation component onto the optical axis ω, that is defined as the intersection of the plane of incidence (spanned by the incoming light vector and the surface normal) and the sample surface. The transverse Kerr effect yields a change in the intensity of light that is proportional to the magnetisation component

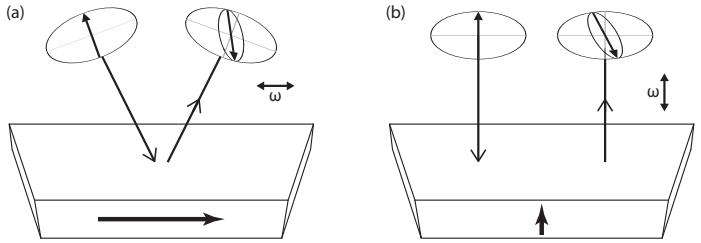

Figure 5.1. Longitudinal and polar Magneto-Optical Kerr Effect: (a) The longitudinal Kerr effect yields a change of the polarisation proportional to the magnetisation component along the optical axis ω, that is defined as the intersection of the plane of incidence (spanned by the incoming light vector and the surface normal) and the sample surface. (b) The change of polarisation in the polar Kerr effect is proportional to the out-of-plane magnetisation component.

that is perpendicular to the optical axis. The polar Kerr effect (Figure 5.1(b)) results in a change of the polarisation proportional to the out-of-plane component of the magnetisation.

Macroscopically, both the Kerr effects and the Faraday effect can be described by two different complex indices of refraction for right-handed and left-handed circularly polarised light [386]. Linearly polarised light is then described as a superposition of circularly polarised components. An equivalent description is obtained using a refractive tensor with off-diagonal elements.

Microscopically, the magnetooptical effects originate in the coupling of the net electron spin of a ferromagnet to the electric field of light via spin–orbit coupling. The effect can also be described qualitatively in a simple classical picture: As the light beam propagates through the medium, its oscillating electric field induces the oscillation of electrons. In a non-magnetic medium, circularly polarised light of opposite handedness will drive circular electron motion with the same radius but opposite sense of rotation. In a magnetic field (applied externally or created by the material itself) applied along the propagation direction of the light, an additional Lorentz force acts on the electron motion. It points towards the centre of motion or away from it, depending on the sense of rotation, and increases or decreases the radius of the motion. The secondary waves that result from these different motions are thus different for circularly left and right polarised light, giving rise to a rotation and ellipticity of linearly polarised light.

While the Kerr effect relies on reflection from the surface of a ferromagnetic material, the Faraday effect occurs in transparent media. The latter needs to be considered in the present measurements because the microscope lens is positioned inside the externally applied field. The change

of the polarisation that is thus measured is proportional to the magnetic field intensity and can easily be corrected for: When a ferromagnetic hysteresis curve is measured in the MOKE microscope, the linear component from the Faraday effect is determined from the high field parts of the curve where the magnetisation is saturated and the curve without the Faraday effect would be flat.

The modulation of the polarisation due to the Kerr effect can be transformed into a change of intensity by placing an analyser in extinction with the polariser (that created the polarisation of the light) after the light is reflected from the sample surface. In order to determine the sense of rotation, the analyser is set at a small skew angle α from extinction. As an optical technique, the spatial resolution of MOKE microscopy is diffraction limited by the optical wavelength to – at best – 250 nm. The information depth is approximately half the penetration length of light into the material, i.e. a few tens of nm [387, 388].

When polariser and analyser are nearly crossed, an image of the sample surface is still measured. The magnetic domain image is thus compromised by non-magnetic contrast that can be removed using a background subtraction method as follows: A background image is obtained by averaging 16 images of the sample that are taken in a large enough applied AC magnetic field at the frequency of a few Hz. During this process the magnetisation oscillates between positive and negative saturation. The magnetic contrast is thus averaged out and the background image contains only non-magnetic information. Subtracting the background image from subsequent measurements, images containing purely magnetic contrast are obtained. Of course the stability of the imaging process needs to be good enough to allow for this. Further improvements of the image quality can be obtained by averaging over several (usually 4) magnetic images.

MOKE microscopy allows for imaging of the spatial magnetisation distribution in thin films both at remanence and in applied magnetic fields. Moreover, local hysteresis curves can be extracted from measurements during magnetic field sweeps. Concurrent application of electric fields is possible with a dedicated sample holder. [20, 383, 386, 388–390].

5.4.2 Birefringence

A MOKE microscope can also be used to image ferroelectric-ferroelastic domains using birefringent contrast. Birefringence leads to an angular dependence of the extinction direction depending on the crystallographic direction. In the case of a_1–a_2 stripe domains in $BaTiO_3$, it leads to a difference in light intensity that is obtained after the analyser because of the 90° angle between the lattice elongations of the domains. In multiferroic heterostructures, ferromagnetic and 90° ferroelectric domains can be imaged in the same microscope if the ferromagnetic film is thin enough (a few tens of nm) to be semitransparent. This is the case for the example given in Figure 4.1. As the lattice elongation in 180° ferroelectric domains is oriented in the same direction, these domains cannot be imaged using polarised light [127, 150, 175, 391].

5.5 Scanning Electron Microscopy with Polarisation Analysis

Imaging of the magnetisation in thin and ultra-thin films with high spatial resolution – down to a few nm – is possible using a Scanning Electron Microscope with Polarisation Analysis (SEMPA), also known as spin-SEM. In a Scanning Electron Microscope (SEM), the surface of a sample is scanned by a highly focused electron beam and the secondary or backscattered electrons emanating from the sample are collected to image the surface topography, or determine the composition of the sample. When imaging a metallic ferromagnet, the secondary electrons are spin polarised. This spin polarisation (which is a vector) reflects the net spin density in the material, which is anti-parallel with the magnetisation. An analyser is used to determine the spin polarisation of the electrons: Electrons of opposing polarisation are scattered into opposite angles. Using an analyser with four detector quadrants – and scattering into orthogonal directions – two perpendicular spin components can be determined independently. Taking the difference between opposing quadrants, a 2-dimensional vector map of the magnetisation in the sample surface is obtained. Using a colour wheel, where each angular direction is assigned a colour, the magnetisation can be displayed in a colour image. Summing over all quadrants allows to simultaneously image the topography of the sample. Unfortunately, spin detectors are highly inefficient which considerably increases the time needed to obtain images. Moreover, secondary electrons

are emitted from a region near to the surface, limiting the imaging depth to approximately 1 nm. The resulting surface sensitivity of the technique may be an advantage, but it requires ultra-high vacuum conditions to guarantee ultra-clean surfaces. Generally, samples inserted into the microscope need to be cleaned from contamination – such as oxide layers – by ion milling. Finally, the spin polarisation of the secondary electrons is sensitive to magnetic fields. Images can thus only be taken at remanence. Recently, the correlation between ferromagnetic and ferroelectric domains in multiferroic heterostructures was demonstrated at high spatial resolution using SEMPA for magnetic contrast and backscattered electrons for ferroelectric contrast in exchange coupled CoFe/$BiFeO_3$ [343, 392] and strain coupled Fe/$BaTiO_3$ [392] heterostructures [393–397].

5.6 Micromagnetic Modelling

The experimental results presented in this Thesis are complemented with Micromagnetic modelling (cf. the Paragraph on Micromagnetism on Page 8). Using experimentally determined parameters, the temporal and spatial distribution of the magnetisation can be calculated by minimising the energy given in Equation 2.4 or solving the LLG equation (Equation 2.31) under the correct boundary conditions. In rare cases analytical solutions of the energy minimisation may be found. An example is the Stoner–Wohlfarth Model (Section 2.7) where the magnetostatic and exchange energies can be ignored. Another example is given by ferromagnetic films that exhibit regular anisotropy modulations (cf. Pages 24 and 53). In that case the remanent magnetisation distribution can be calculated in a 1-dimensional model if the magnetostatic energy can be ignored [398],[IV]. In general, the magnetisation distribution cannot be calculated analytically and numerical simulations are used. Micromagnetic simulation packages are readily available, and the results presented in this Thesis have been obtained using OOMMF [399] and MuMax3 [400,401]. For simulations, the continuous magnetisation postulated in Micromagnetism is discretised into finite elements, usually cuboids. The magnetisation is taken to be uniform within one element which thus need to be smaller than the exchange length (Equation 2.33) in order to accurately model the variations in magnetisation direction. Moreover, care needs to be taken when initialising the simulations, because Micromagnetism relies on small angles between the orientation of the magnetisation in neigh-

bouring cells (cf. Section 2.1.3).

Here, OOMMF is used to calculate the magnetisation by energy minimisation[1]. As only a finite system can be simulated, 2-dimensional boundary conditions [402] have been implemented in order to calculate the magnetostatic energy – associated with long range stray fields – correctly. The long range nature of the magnetostatic energy leads to time consuming calculations that require a large amount of computer memory. A considerable speed-up of calculations is obtained when using GPUs, instead of CPUs, to calculate the magnetostatic potential due to superior performance of GPUs in parallel calculations [403]. MuMax3 is based on the use of GPUs and was used to calculate magnetisation dynamics by solving the LLG equation [14, 21–23].

[1]Calculating the magnetisation dynamics by solving the LLG equation is also possible, albeit slower due to the increase in computations needed.

6. Results and Discussion

I'm looking for the unexpected.
I'm looking for things I've never seen before.

Robert Mapplethorpe

In the first Section of this Chapter I review how domain pattern transfer in multiferroic heterostructures leads to strong pinning of ferromagnetic domain walls onto their ferroelectric counterparts. Pinning is discussed in Publications I, II and V, and leads to the creation and tuning of two types of magnetic domain walls: charged and uncharged ones [II,VII]. Size scaling of domain pattern transfer is discussed in general using micromagnetic modelling [IV] and demonstrated experimentally in a CoFeB/$BaTiO_3$ heterostructure [IV, VII]. Electric field control of ferromagnetic domain patterns is presented for in-plane [I] and out-of-plane [VI] magnetised thin films on $BaTiO_3$. Finally, results from Publication V demonstrate reversible electric field driven magnetic domain wall motion in epitaxial Fe/$BaTiO_3$ heterostructures [III].

6.1 Magnetic Domain Wall Pinning

As mentioned on Page 53, correlations between domains in ferromagnetic thin films and ferroelectric/ferroelastic domains in $BaTiO_3$ substrates can be obtained via interfacial strain transfer and inverse magnetostriction. The $BaTiO_3$ substrates considered here exhibit a_1–a_2 stripe domains (cf. Section 3.2.1) with a width of approximately 5 μm. The polarisation is associated with a lattice elongation of 1.1% that rotates in-plane by 90° between domains. In multiferroic heterostructures, this lattice elongation is partially transferred to an overlaying ferromagnetic thin film leading to a uniaxial anisotropy via inverse magnetostriction (cf. Section 2.4.4).

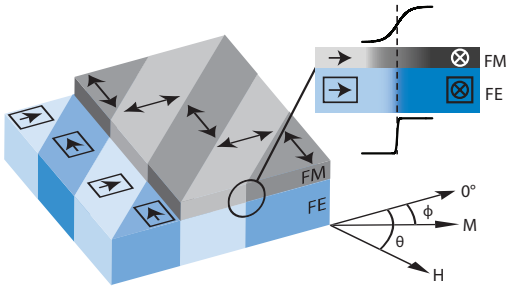

Figure 6.1. Schematic illustration of a ferromagnetic/ferroelectric heterostructure consisting of a magnetostrictive film and a $BaTiO_3$ substrate exhibiting an a_1–a_2 stripe domain structure. Angles are defined on the bottom right. In the inset on the top right the pinning of broad ferromagnetic domain walls onto narrow ferroelectric domain walls is sketched.

As a result, the ferromagnetic film exhibits a uniaxial anisotropy that rotates by 90° between stripe domains as shown schematically in Figure 6.1. In this Section two samples with different ferromagnetic films are considered: A 15 nm thick $Co_{60}Fe_{40}$ (CoFe) film deposited at room temperature by Electron Beam Evaporation, and a 20 nm thick $Co_{40}Fe_{40}B_{20}$ (CoFeB) film deposited via Magnetron Sputtering at 300°C. In the latter case, strain transfer occurs when the $BaTiO_3$ substrate is cooled through the ferroelectric phase transition ($T_C = 120°C$) after thin film deposition. Qualitatively, the behaviour of both heterostructures is the same, while the quantitative results differ slightly[1]. In both cases the saturation magnetostriction is positive and the induced uniaxial anisotropies are collinear with the lattice elongation, and thus the ferroelectric polarisation. No other significant anisotropy contributions are observed.

Domain pattern transfer is confirmed in both cases by MOKE microscopy and the ferromagnetic domains have been imaged using SEMPA for the CoFeB/$BaTiO_3$ heterostructure. The latter results are presented in Figure 6.2. Here, two images with magnetisation contrast in two perpendicular in-plane directions are combined to form a colour image that presents the magnetisation directions in the sample. Figure 6.3 presents the angular dependence of the remanent magnetisation determined separately for a_1- and a_2-domains using MOKE microscopy. A comparison with Figure 2.10(b) confirms the presence of two perpendicular uniaxial anisotropy axes that are oriented as sketched in Figure 6.1. The anisotropy constant

[1]The saturation magnetostriction $\lambda_{CoFe} = 6.8 \times 10^{-5}$ [404] of CoFe is slightly larger than that of CoFeB ($\lambda_{CoFeB} = 2 \times 10^{-5}$ [405]). The saturation magnetisations are $M_{S,CoFe} = 1.7 \times 10^6$ A/m and $M_{S,CoFeB} = 1.2 \times 10^6$ A/m [405], while the Young's moduli are $Y_{CoFe} = 2.5 \times 10^{11}$ [406] and $Y_{CoFeB} = 1.6 \times 10^{11}$ [261]. The exchange stiffness in both cases is taken as $A = 2.1 \times 10^{-11}$ J/m. These parameters are used in the Micromagnetic simulations whose results are presented here.

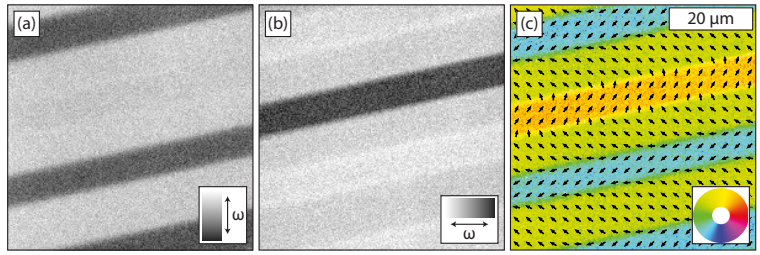

Figure 6.2. Contrast in two perpendicular directions (a) & (b) can be obtained simultaneously using SEMPA and combined into a colour and vector image of the magnetisation direction in a $Co_{40}Fe_{40}B_{20}$ film on top of a $BaTiO_3$ substrate exhibiting an a_1–a_2 stripe domain structure.

as determined from hard axis magnetisation curves (cf. Section 2.7) is $K_{me} = 1.7 \times 10^4$ J/m^3. Coincidentally, the same result is obtained for the CoFe film. The observed anisotropy strengths vary from sample to sample and are generally between $K_{me} = 1 \times 10^4$ J/m^3 and $K_{me} = 3 \times 10^4$ J/m^3. Considering full strain transfer, the theoretical maximum for the strain induced anisotropy strength is calculated using Equation 2.25 to be $K_{me} = 0.5 \times 10^5$ J/m^3 and $K_{me} = 2.8 \times 10^5$ J/m^3 for the CoFeB and CoFe films, respectively. This means that less than 10% of the strain is transferred to the CoFe film in the as-deposited sample. Strain transfer to the CoFeB film is more efficient. This can be attributed to the fact that the strain is transferred during the ferroelectric phase transition after thin film deposition at elevated temperature, while the CoFe film was deposited at room temperature (see above).

Domain images of the CoFe film in an external magnetic field perpendicular to the stripe domains (Figure 6.4) are measured at different stages of the magnetisation reversal process. Pattern transfer is observed over a large range of applied magnetic fields and only erased by large fields that fully saturate the magnetisation. Starting from saturation, the magnetisation in neighbouring domains rotates in opposite directions with decreasing field strength and aligns with the respective anisotropy axes

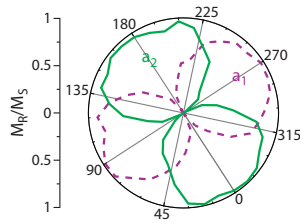

Figure 6.3. The angular dependence of the remanent magnetisation of the $Co_{40}Fe_{40}B_{20}$ film in a_1- and a_2-domains obtained using MOKE microscopy confirms the orthogonal alignment of the uniaxial magnetic easy axes. The orientation of the polar plot corresponds to the images in Figure 6.2.

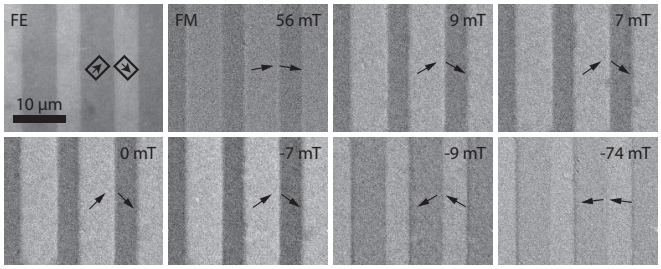

Figure 6.4. MOKE microscopy images of ferroelectric (FE) and ferromagnetic (FM) domain patterns in the $Co_{60}Fe_{40}/BaTiO_3$ heterostructure during magnetisation reversal. The field is applied perpendicular to, and the optical axis parallel to the stripe domains.

at remanence, creating 90° domain walls. In a reverse magnetic field the magnetisation in the domains switches independently, while the domain walls remain immobile. This is in stark contrast with more conventional magnetisation reversal that is associated with magnetic domain wall motion. In ferromagnetic/ferroelectric heterostructures exhibiting domain pattern transfer, the abrupt 90° change in the anisotropy direction on top of narrow ferroelectric domain boundaries leads to strong pinning of magnetic domain walls.

Magnetically Charged and Uncharged Domain Walls

The remanent magnetic microstructure of pinned magnetic domain walls is imaged in the CoFeB film using SEMPA (Figure 6.5) after saturation in a large magnetic field applied perpendicular (a) and parallel (b) to the domain wall. In both cases the magnetisation in the domains aligns with the respective anisotropy axes leading to a 90° spin rotation across the domain wall. However, the magnetisation in the centre of the wall is aligned with the saturating field direction leading to domain walls of opposite chirality. More importantly, the width δ of the domain walls differs significantly (note the different scales in Figures 6.5(a) & (b)). The measured widths are $\delta_{uc,CoFeB} = 70 \pm 10$ nm and $\delta_{c,CoFeB} = 560 \pm 20$ nm for uncharged and charged domain walls, respectively. The results are reproduced using micromagnetic simulations yielding domain wall widths of $\delta_{uc,CoFeB} = 68$

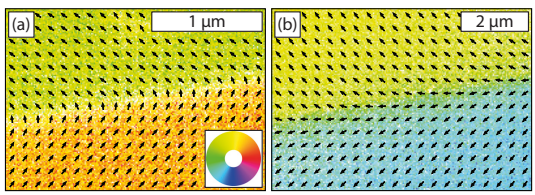

Figure 6.5. SEMPA images of (a) uncharged and (b) charged domain walls in the $Co_{40}Fe_{40}B_{20}/BaTiO_3$ heterostructure.

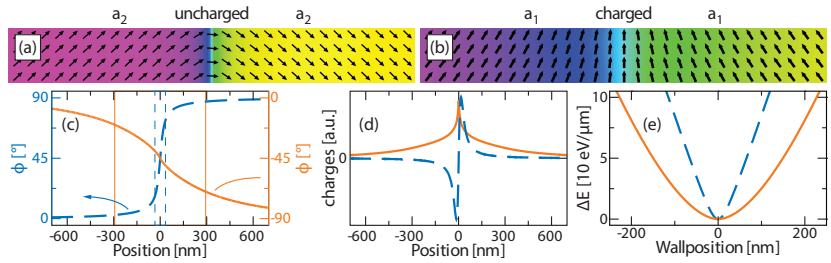

Figure 6.6. Simulated remanent microstructure of (a) uncharged and (b) charged domain walls in the $Co_{60}Fe_{40}/BaTiO_3$ heterostructure ($K_{me} = 1.7 \times 10^4$ J/m^3). (c) Corresponding magnetisation profile of uncharged (dashed line) and charged (solid line) domain walls and their associated charges (d) and pinning potential (e).

nm and $\delta_{c,CoFeB} = 581$ nm, which is in close agreement with the measured values. Images obtained using the parameters for 10nm thick CoFe films are presented in Figures 6.6(a) and (b). The corresponding domain wall profiles are shown in Figure 6.6(c). The simulated domain wall widths are $\delta_{uc,CoFe} = 68$ nm and $\delta_{c,CoFe} = 587$ nm. The large difference in wall widths of an order of magnitude can be explained by considering the effect of virtual magnetic charges (cf. Section 2.3). They are calculated using Equation 2.13 and presented in Figure 6.6(d). In case (a) of the initialising field applied perpendicular to the domain wall, the magnetisation of neighbouring domains align in a head-to-tail configuration leading to no overall magnetic charge. There is however a magnetic dipole that develops. This domain wall will be referred to as being magnetically uncharged. In case (b) the magnetisation in neighbouring domains aligns in a head-to-head or tail-to-tail configuration leading to a net magnetic charge in the domain wall. This charging leads to a much wider wall consisting of a core where the magnetisation rotates rather abruptly and two elongated tails. This is in contrast to the uncharged domain wall, where magnetisation rotation occurs more uniformly over a much shorter length scale. The domain wall widths can be compared to analytical calculations using the width given by Equation 2.35 as an estimate for the uncharged case and half the width from Equation 2.34 to approximate the charged domain wall. They yield $\delta_{uc} \approx 80$ nm and $\delta_c \approx 800$ nm for both CoFeB and CoFe films[2]. Micromagnetic simulations further reveal that the total energy associated with charged domain walls is higher than for uncharged ones.

[2]The fact that the wall widths of CoFeB and CoFe films of different thickness coincide may be surprising at first. However, the parameters that determine the width of uncharged domain walls, namely the anisotropy strength K_{me} and the exchange stiffness A are the same in the films considered here (cf. footnote on page 74). The width of charged domain walls on the other hand scales with the square of the saturation magnetisation and the thickness of the film. Coincidentally their product is the same for both films.

Pinning Potential

The potential pinning the ferromagnetic domain wall onto its – orders of magnitude narrower – ferroelectric counterpart is calculated in a first approximation by considering the energy cost associated with the lateral displacement of the rigid wall profile with respect to its equilibrium position. In this case only the magnetic anisotropy energy needs to be considered. The derivation of the analytical expression for the potential is given in the appendix of Publication V, and the potential is shown in Figure 6.6(e) for both charged and uncharged domain walls. Its shape differs because of the distinct domain wall profiles. The symmetry of the potential is a consequence of the symmetric domain wall profile and the coinciding anisotropy strengths in both a_1- and a_2-domains. When the anisotropy strengths in neighbouring domains differ – an example is shown in Figure 4(d) of Publication I – the pinning potential is asymmetric.

Magnetic Domain Wall Tuning

The properties of both charged and uncharged domain walls can be tuned continuously in an applied magnetic field. In Figure 6.7(a) the absolute value of the spin rotation $|\phi_1 - \phi_2|$ within the ferromagnetic domain wall is plotted as a function of magnetic field perpendicular to the domain wall. The experimental data (red symbols) are extracted from hysteresis curves (Publication II, Figure 2(c)) on two neighbouring domains shown in Figure 6.4. Results from numerical simulations (solid black line) reproduce the experimental data. As magnetisation reversal in neighbouring domains takes place by rotation in opposite directions, the spin rotation increases from zero at saturation to 90° at remanence. In a reverse field the spin rotation continues to increase to almost 180° just before abrupt magnetisation switching. After switching, the spin rotation is significantly lowered

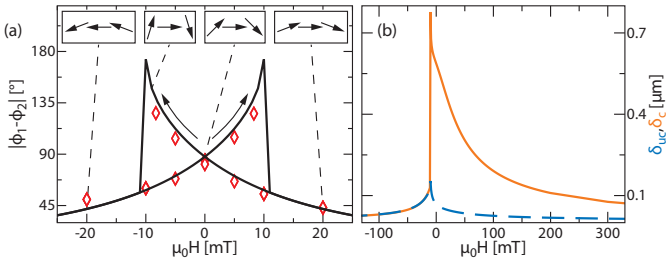

Figure 6.7. (a) Spin rotation within the magnetic domain walls as a function of applied magnetic field determined experimentally (red symbols) and numerically for $K_{me} = 1.7 \times 10^4$ J/m^3 (solid line). The arrows in the insets sketch the magnetisation direction in the domains and the centre of the domain walls for selected field strengths. (b) Field tuning of the domain wall widths of uncharged (dashed line) and charged (solid line) domain walls.

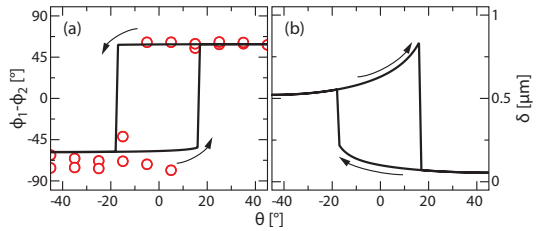

Figure 6.8. (a) Spin rotation within the domain walls as a function of field angle at a constant field strength of 10 mT as obtained from experiments (symbols) and simulations for $K_{me} = 1.7 \times 10^4$ J/m^3 (solid line). (b) Corresponding change in the domain wall width.

and continues to reduce with increasing magnetic field.

Tuning of the spin rotation in an applied magnetic field is associated with a change in the domain wall widths as plotted in Figure 6.7(b) for uncharged (dashed blue line) and charged magnetic domain walls (solid orange line). The domain wall width is tuned continuously from zero just below saturation to hundreds or even thousands of nm depending on the strength of the strain induced anisotropies and the type of magnetic domain wall.

Switching of Domain Wall Type

By rotating a sufficiently large applied magnetic field, hysteretic switching between charged and uncharged magnetic domain walls can be obtained. Abrupt switching at well-defined angles leads to a reversal of the wall chirality $\phi_1 - \phi_2$ as shown in Figure 6.8(a) using experimental (red symbols) and numerical (solid black line) data. The associated change in domain wall type leads to a large modification of the domain wall width by one order of magnitude (Figure 6.8(b)).

6.2 Scaling of Domain Pattern Transfer

As explained in Sections 4.2.1 and 4.2.3, domain pattern transfer in multiferroic heterostructures originates from magnetoelectric coupling that is mediated via strain transfer from ferroelectric domains in $BaTiO_3$, or via exchange coupling to the canted magnetic moments of multiferroic $BiFeO_3$. In this Section, I consider ferroelectric substrates where the in-plane ferroelectric polarisation (or its projection) rotates by 90° between regular stripe domains. In the overlaying ferromagnetic film, uniaxial anisotropies, that are correlated with the ferroelectric polarisation, are induced. Pattern transfer from the ferroelectric to the ferromagnetic component of the heterostructure is opposed by exchange and magnetostatic

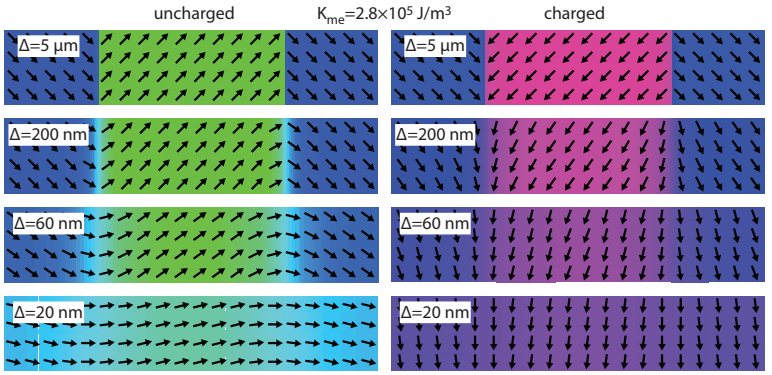

Figure 6.9. Images of the simulated remanent magnetisation in stripe domains of decreasing width for uncharged (left) and charged (right) domain walls.

interactions that compete with the induced magnetic anisotropies. Using Micromagnetic simulations and analytical modelling, I show that pattern transfer breaks down, when the widths of ferroelectric domains and pinned ferromagnetic domain walls become comparable. As both charged and uncharged domain walls can be initialised, two scaling regimes of pattern transfer are observed at remanence. The effect of charged and uncharged domain walls is observed experimentally in the switching behaviour of a $Co_{40}Fe_{40}B_{20}/BaTiO_3$ heterostructure.

6.2.1 Size Dependence of Pattern Transfer at Remanence

The dependence of pattern transfer on the width of ferroelectric stripe domains is investigated numerically using parameters for a 10 nm thick $Co_{60}Fe_{40}$ film on $BaTiO_3$ and assuming full strain transfer (K_{me} = 2.8 × 10^5 J/m^3). The domain wall widths are then δ_{uc} = 15 nm and δ_c = 62 nm. Figure 6.9 shows remanent magnetisation images for various domain widths Δ in the presence of uncharged (left column) or charged (right column) domain walls. In both cases, full pattern transfer is obtained at remanence for 5 μm wide stripe domains. The magnetisation in the domains aligns with the uniaxial anisotropies and the spin rotation in the walls is 90°. As a function of decreasing domain width, the spin rotation decreases continuously (cf. Figures 3(a) & (d) in Publication IV) and the magnetic contrast between adjacent domains is reduced, until almost parallel magnetisation alignment is obtained for small Δ, indicating the breakdown of pattern transfer. However, breakdown occurs for different Δ, depending on whether charged or uncharged domain walls are initialised. This is seen in the images of Figure 6.9 corresponding to

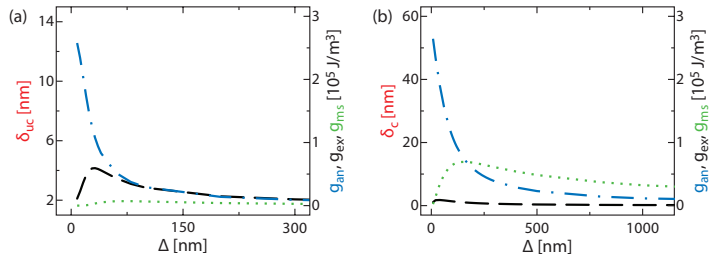

Figure 6.10. Dependence of the anisotropy (blue dash-dotted line), exchange (black dashed line), and magnetostatic energy densities (green dotted line) as a function of domain width Δ for (a) uncharged and (b) charged domain walls obtained for $K_{me} = 2.8 \times 10^5$ J/m^3.

$\Delta = 60$ nm: When uncharged domain walls are initialised, domains are clearly resolved, whereas a largely uniform magnetisation is observed in the presence of charged domain walls. The difference in scaling behaviour is explained by considering the energies that dominate in each case. The contributions from anisotropy, exchange, and magnetostatic energy densities are plotted as a function of domain width in Figure 6.10 for both uncharged and charged domain walls.

In the presence of uncharged walls, the magnetisation configuration is determined by a competition between the uniaxial anisotropy energy and the exchange energy which also determines the width of the uncharged domain wall. For charged domain walls (Figure 6.10(b)), the anisotropy and magnetostatic energies dominate. Breakdown of pattern transfer is thus dictated by a competition between the energy contributions that determine the width of charged walls. Comparing the respective domain wall widths with the dependence of the spin rotation on Δ as a function of anisotropy strength, the domain wall widths δ can be taken as good indicators for the breakdown of pattern transfer [3]: Full pattern transfer is obtained for $\Delta \gg \delta$, while parallel magnetisation alignment is obtained for $\Delta \ll \delta$. In between these two cases the spin rotation scales continuously with Δ.

1-Dimensional Model

A 1-dimensional analytical model reproduces the breakdown of domain pattern transfer for arbitrary anisotropy strengths, if the magnetostatic energy can be ignored. This is the case when uncharged domain walls are initialised and the competition between the anisotropy and exchange energy determines the properties of the magnetic thin film. Periodic boundary conditions are used to calculate the local magnetisation directions

[3] A detailed discussion is given on Page 3 of Publication IV.

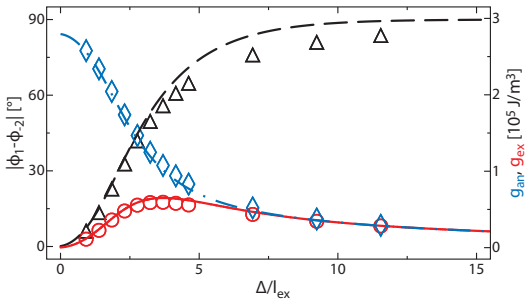

Figure 6.11. Analytically calculated spin rotation (black dashed line), anisotropy energy density (blue dash-dotted line) and exchange energy density (red solid line) as a function of reduced domain width Δ/l_{ex}. The data obtained from the 1-dimensional model are compared to results from micromagnetic simulations (symbols) obtained for $K_{me} = 2.8 \times 10^5$ J/m^3.

that minimise the total energy. The model allows to calculate both the spin rotation between adjacent domains and the anisotropy and exchange energy. It is derived in detail in the supplementary material of Publication IV and its results are plotted in Figure 6.11. A comparison of the calculated results (lines) with simulations (symbols) reveal an excellent qualitative and quantitative agreement. While the simulations have been performed for a given anisotropy strength ($K_{me} = 2.8 \times 10^5$ J/m^3), the analytical model reveals that the scaling depends only on the ratio between the domain width Δ and the exchange length, which is proportional to the domain wall width δ_{uc}. The model thus gives strong support to the interpretation that domain pattern transfer breaks down when Δ and δ become comparable.

Dependence of Scaling on Anisotropy Strength and Film Thickness

The width of magnetic domain walls does not only depend on the strength of the uniaxial anisotropies, but also on film thickness in the case of charged domain walls (cf. Equations 2.35 and 2.34). Figure 6.12(a) presents a comprehensive comparison of the breakdown of domain pattern transfer as a function of anisotropy strength and film thickness. The widths of both charged (filled symbols) and uncharged (open symbols) domain walls obtained from simulations are plotted for film thicknesses of 10 and 50 nm. Lines present the calculated domain wall widths, that prove to be in good agreement with simulations. The widths of uncharged domain walls are not expected to depend on film thickness[4]. Charged domain walls conversely broaden with increasing film thickness due to the accumulation of magnetic charges.

[4]The presence of a magnetic dipole does, however, lead to an insignificant decrease of wall width with thickness.

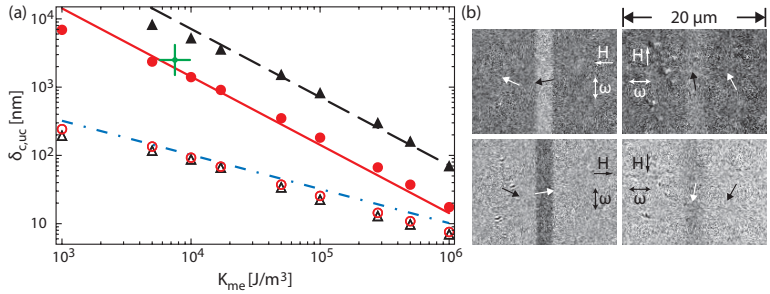

Figure 6.12. (a) Simulated uncharged (open symbols) and charged (filled symbols) domain wall widths as a function of uniaxial magnetic anisotropy strength for 10 nm (circles) and 50 nm (triangles) thick films. Lines correspond to calculated domain wall widths using Equations 2.35 and 2.34. (b) MOKE microscopy images of magnetic domains in a 50 nm thick $Co_{40}Fe_{40}B_{20}$ film on $BaTiO_3$ for a 8 mT magnetic field applied perpendicular (left) and parallel (right) to the stripe domains. The parameters (see main text) for the experimental sample imaged in (b) are marked by a green cross in (a).

The graph in Figure 6.12(a) can be seen as a phase diagram for domain pattern transfer: For a given combination of anisotropy strength, film thickness and domain wall type, pattern transfer is obtained if the parameters are above the curves, while uniform magnetisation is obtained for parameters below the curves. Because of the presence of two scaling regimes – depending on domain wall type – parameters can be chosen to lie between the phase transitions for charged and uncharged domain walls. Rotation of an applied magnetic field then leads to the successive writing and erasure of magnetic domains[5].

Experimental Verification

Since scaling of domain pattern transfer depends on anisotropy strength and thickness, choosing heterostructures with thick ferromagnetic films and low anisotropies is expected to allow for the imaging of the phenomenon of pattern transfer breakdown even with the limited spatial resolution of MOKE microscopy. Such results are obtained using a 50 nm thick CoFeB film on a $BaTiO_3$ substrate exhibiting a_1–a_2 stripe domains with a strain induced uniaxial anisotropy of $K_{me} = 7.5 \times 10^3$ J/m^3. These parameters are marked with a green cross in Figure 6.12(a), showing that for 100 nm $< \Delta <$ 10 µm, the sample is in the region between the phase transitions for uncharged and charged domain walls. The images in Figure 6.12(b) show a magnetic stripe domain of width $\Delta \approx 2.5$ µm in a magnetic field of 8 mT applied at different angles. Clear magnetic contrast is observed when the field applied perpendicular to the stripe domain creates uncharged domain walls (left). When the field is rotated

[5]This is demonstrated with simulation videos in the online supplementary material of Publication IV.

parallel to the stripe domains, wider charged domain walls are initialised and the spin rotation – and therefore the contrast between the domains – is notably reduced (right).

Another experimental example of the scaling of domain pattern transfer is given in Reference [343] for 2.5 nm thick $Co_{0.9}Fe_{0.1}$ films exchange coupled to a $BiFeO_3$ substrate. Line scans over several, 310 nm wide stripe domains using SEMPA demonstrate a reduction of the remanent spin rotation from 90° to 60° when the domains are separated by uncharged domain walls. The parameters of this heterostructure correspond to $\Delta/l_{ex} \approx 5$ which means that the reduction in spin rotation agrees well with the analytically calculated scaling behaviour presented in Figure 6.11.

6.2.2 Magnetisation Reversal

Finite size scaling of pattern transfer has a pronounced effect on magnetisation reversal. In wide domains, magnetisation reversal for fields applied parallel or perpendicular to the stripe domains proceeds via coherent spin rotation and abrupt switching. The shape of the hysteresis curve corresponds to what is expected from the Stoner–Wohlfarth model when the angle between the applied magnetic field and the uniaxial magnetic anisotropy axis is 45°. The reduced remanent magnetisation is $m_R = 1/\sqrt{2}$, as expected. For decreasing domain width the hysteresis curve is increasingly square and resembles an easy axis curve in the limit of $\Delta \ll \delta$. The remanent magnetisation thus approaches one, and no gradual rotation is observed any more [6].

In many $BaTiO_3$ substrates, a_1–a_2 stripe domains show a distribution in domain widths and generally one type of domain is wider than the other. In Publication VII such a substrate is used to grow a heterostructure with a ferromagnetic CoFeB wedge film by Magnetron Sputtering at 300°C. The average domain widths are $\Delta_1 \approx 8$ μm for a_1-domains and $\Delta_2 \approx 5$ μm for a_2 domains. The thickness of the wedge film increases linearly from t = 0 nm at one end of the substrate to t = 150 nm at the other end. The heterostructure is used to investigate the influence of scaling on the magnetisation switching as a function of both domain width and film thickness. To this end, a large set of MOKE images is collected as a function of magnetic field strength, for fields applied parallel and perpendicular to the stripe domains, at different film thicknesses. In order to simplify the visualization and analysis of the data, contour plots such as

[6] Simulation results are presented in Publication IV, Figure 2.

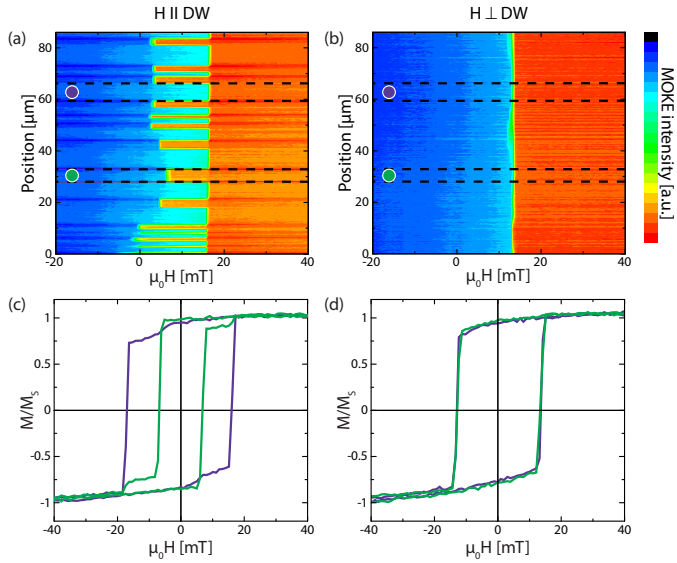

Figure 6.13. Contour plots illustrating magnetisation reversal at a film thickness of 100 nm for magnetic fields applied either parallel (a) or perpendicular (b) to the stripe domains. The colours correspond to projections of the magnetisation onto the magnetic field direction. (c) & (d) Corresponding hysteresis curves of marked a_1 (violet) and a_2 (green) stripe domains. Note that the sample area is the same for both field orientations.

those presented in Figure 6.13 are obtained from each series of magnetic field sweeps: The contrast of each image taken at a given magnetic field is averaged along the direction of the stripe domains yielding a line in the contour plot. For better visualization, the magnetisation component along the field direction is colour coded[7].

The contour plots and corresponding hysteresis curves in Figure 6.13 show a clear dependence of the magnetisation reversal process on the direction of the applied magnetic field: For magnetic fields applied perpendicular to the stripe domains, magnetisation reversal occurs simultaneously, while distinct switching fields for a_1- and a_2-domains are observed when the magnetic field is applied parallel to the domains. The difference in magnetisation reversal is explained by the presence of charged or uncharged domain walls.

The application of a magnetic field parallel to the stripe domains leads to the formation of high energy charged domain walls (Figure 6.13(a)). The larger the spin rotation, the higher the energy of the domain wall, and at some magnetic field value the energy of the system is reduced via the creation of uncharged domain walls by switching the magnetisation in every second stripe. As the magnitude of the external magnetic field increases

[7] An instructive example of how the contour plots are obtained is given in Figure 3 of Publication VII.

in the reverse direction, a second switching event reverses the magnetisation in the remaining stripe domains. Uncharged domain walls are thus converted back into charged domain walls. However, their spin rotation is small and the energy cost associated with the wall transformation is thus lower than the gain in Zeeman energy.

When the magnetic field is applied perpendicular to the stripe domains (Figure 6.13(b)), uncharged domain walls are formed and domain wall transformations would be associated with an increase in energy. Consequently, synchronised magnetisation reversal that avoids the creation of charged domain walls is observed. A similar, albeit weaker, dependence of magnetisation reversal on the applied field direction was observed in Reference [341] for exchange-coupled $LaSrMnO_3/BiFeO_3$ heterostructures. In thin films where ion-irradiation creates stripe domains with an exchange bias that alternates by 90°, the angular dependence of magnetisation reversal is also influenced by the magnetic domain wall type [60].

Scaling of Magnetisation Reversal with Domain Width

The contour plot in Figure 6.13(a) – for fields applied parallel to the domains – shows that the switching field H_{S2} of a_2-domains is reduced when their width Δ_2 decreases. Comprehensive analysis reveals that H_{S2} is inversely proportional to $-\Delta_2$ (cf. Figure 6.14). This behaviour is due to the fact that the density of charged domain walls increases with decreasing domain width. The gain in energy density associated with the switching of narrower domains is therefore higher than for wide domains. a_1-domains are wider and they do therefore not switch before a_2-domains. The switching field H_{S1} of a_1-domains is however the same regardless of their width, which is counter-intuitive, considering that switching leads to the forma-

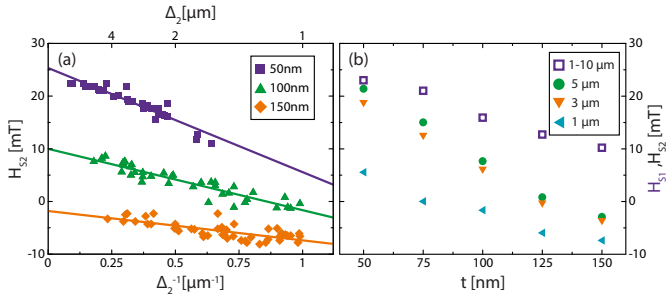

Figure 6.14. (a) Measured (symbols) switching fields of a_2-domains as a function of domain width for selected film thicknesses and corresponding linear fits. (b) Comparison of the switching fields of a_1-domains (H_{S1}, open symbols) and a_2-domains (H_{S2}, filled symbols) as a function of film thickness for various domain widths Δ_2. Note that in both cases the magnetic field is applied parallel to the stripe domains.

tion of charged walls and is thus associated with an energy penalty. With the same arguments as for the switching behaviour of a_2-domains, we would expect a dependence of H_{S1} on Δ_1. However, the spin rotation of the charged domain walls that are created during the second switching event is greatly reduced and the magnetic energy of the domain wall is thus low. Hence, energy considerations associated with the type of magnetic domain wall do not influence H_{S1} significantly. The switching field is determined by the magnetic anisotropy strength inside the domains and is thus independent of Δ_1. This argumentation is corroborated by the fact that H_{S1} nearly coincides with the uniform switching field observed when the magnetic field is applied perpendicular to the stripe domains (Figure 6.13(b)).

A similar effect of the domain width on magnetisation reversal was later reported for NiFe films patterned by focused ion-beam irradiation [407]. In alternating irradiated–unirradiated stripe domains the saturation magnetisation is locally reduced. As a result, magnetisation reversal for wide domains proceeds in a two step process. Conversely, uniform magnetisation reversal is obtained in narrow stripes. These results are also interpreted as an effect of finite size scaling.

Scaling of Magnetisation Reversal with Film Thickness

The switching behaviour depends on the energy difference between uncharged and charged domain walls, which is associated with their respective widths. While the former is independent of film thickness, the latter scales linearly with it. The reduction in H_{S2} relative to H_{S1} is therefore expected to be more pronounced in thicker films. This dependence is confirmed by the data presented in Figure 6.14(b). The thickness scaling is more pronounced in wide a_2-domains, where charged walls are not altered by interactions with their neighbours. In narrower domains, their spin rotation is reduced and the energy difference between charged and uncharged domain walls depends less on film thickness (cf. Figure 6.10 & 6.11). Consequently the scaling of H_{S2} with Δ_2 is less important in thicker films where charged domain walls are wider and higher in energy (Figure 6.14(b)).

However, for large film thicknesses and/or narrow a_2-domains, the energy gain associated with the wall transformation can be large enough to cause negative switching fields H_{S2} as seen in Figure 6.14.

6.3 Electric Field Control of Magnetic Domains

Thus far, multiferroic heterostructures have been investigated only at remanence or in applied magnetic field, revealing rich physics due to domain pattern transfer and domain wall coupling. However, these heterostructures are attracting considerable attention mainly due to their potential for electric field control of magnetism. Electric field control of ferromagnetic domains in an in-plane magnetised CoFe/$BaTiO_3$ heterostructure is discussed in Publication I. Electric field driven Spin Reorientation Transitions also proceed via electric field control of magnetic domains (Publication VI).

6.3.1 Magnetic Films with In-Plane Anisotropy

The results presented in this Section are obtained using the CoFe/$BaTiO_3$ heterostructure introduced in Section 6.1 and a heterostructure consisting of a 50 nm thick CoFeB film on a $BaTiO_3$ substrate exhibiting a_1–a_2 stripe domains. Qualitatively, the results obtained on both heterostructures match. In the CoFeB/$BaTiO_3$ heterostructure, the strain induced anisotropies have a strength of $K_{me} = 1 \times 10^4$ J/m^3. Figure 6.15(a) shows the remanent magnetisation of the CoFeB film in the as-deposited state demonstrating domain pattern transfer. Corresponding polar plots of the remanent magnetisation (Figure 6.15(c)) in two adjacent stripe domains confirms the presence of a uniaxial anisotropy that alternates by 90° between a_1- and a_2-domains.

The application of a 6 kV/cm out-of-plane electric field switches the ferroelectric polarisation out-of-plane to form a uniform c-domain. The in-plane symmetry of the $BaTiO_3$ substrate changes from tetragonal to cubic during the switching event. Consequently, the clamped CoFeB film is compressed along the direction in which it was initially elongated. As a result, the anisotropy axes of both stripe domains switch by 90° and the contrast in the image of the remanent magnetisation is inverted (Figure 6.15(b) & 6.15(d)). The domain pattern that is now observed in the ferromagnetic film exhibits the pattern of the initial a_1–a_2 domain structure although the polarisation in the ferroelectric substrate is uniform. It exhibits a memory effect of how the ferroelectric domains looked like before the application of an electric field. This effect is due to partial strain transfer in the as-deposited film, while full strain transfer is achieved during polarisation switching. The measured anisotropy strength is now $K_{me} = 3$

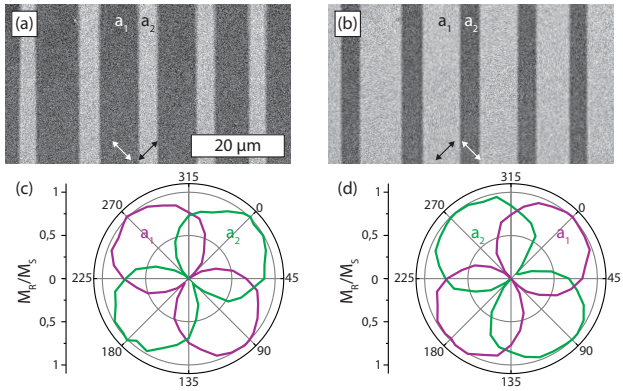

Figure 6.15. (a) MOKE microscopy image of the remanent magnetisation in a 50nm thick CoFeB film after deposition on a $BaTiO_3$ substrate exhibiting a_1–a_2 stripe domains. (b) Image of the same area with the ferroelectric polarisation switched out-of-plane (uniform c-domain) in an electric field of 6 kV/cm. (c) & (d) Normalised remanent magnetisation as a function of angle for two stripe domains. Electric field induced 90° switching of the anisotropy directions is observed.

$\times 10^4$ J/m^3, which indicates almost full strain transfer when compared to the theoretical maximum of K_{me} (cf. Page 75).

In the CoFe/$BaTiO_3$ heterostructure almost full strain transfer is obtained, too, after the application of an electric field. This means that the strength of the anisotropy increases by one order of magnitude. After removal of the electric field, the ferroelectric substrate relaxes into an a–c domain structure as shown in Figure 6.16(FE). In the ferromagnetic film (Figure 6.16(FM)), this results in a complex domain structure due to a coexistence of growth induced and electric field induced strains: On top of ferroelectric c-domains, a_1- and a_2-domains are present just as in the saturated state (cf. Figure 6.15(b)). On top of the newly formed a-domains the remanent magnetisation is uniform. However, two distinct magnetic re-

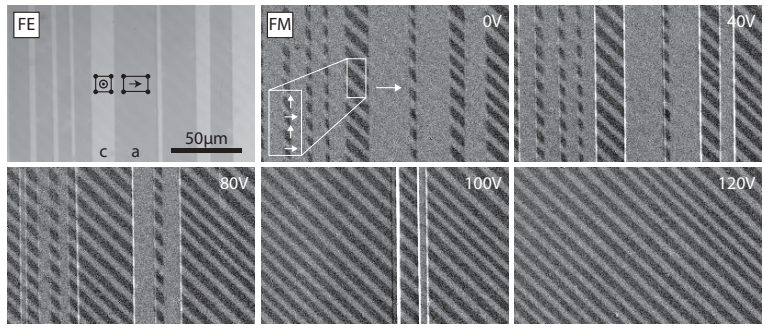

Figure 6.16. Ferroelectric (FE) and Ferromagnetic (FM) domain images after an out-of-plane electric field has been applied to the CoFe/$BaTiO_3$ heterostructure (0V). Subsequent increases of an applied voltage rewrite the observed domain pattern. Note that the images are rotated by 45° with respect to the situation depicted in Figure 6.15.

gions are present: In the parts of the film where a_1-domains were initially observed, the lattice elongation has not changed and the strain induced anisotropy is not significantly altered. The regions of the film where ferroelectric a_2-domains used to be present exhibit a lattice elongation that is perpendicular to the initial one. As a result, the anisotropy strength is increased by one order of magnitude. While both regions on top of ferroelectric a-domains cannot be distinguished at remanence, they exhibit distinct switching fields due to the different anisotropy strengths[8].
The application of an out-of-plane bias voltage grows the favourably oriented c-domains at the expense of a-domains by lateral domain boundary motion. Figure 6.16 shows images of the associated rewriting of the magnetic domain structure, which is a reversible process. These results are independently reproduced in phase-field simulations [303]. Electric field control of magnetic domains in Ni films on $BaTiO_3$ substrates exhibiting a–c domain patterns has also been demonstrated [301].

6.3.2 Magnetic Films with Out-of-Plane Anisotropy

In Cu/Ni multilayers the surface anisotropy favours an in-plane magnetisation (cf. Section 2.4.5). However, the tensile strain imposed by the Cu layers on the Ni layers because of the different lattice constants creates a perpendicular magnetoelastic anisotropy [48–50]. Thus, above a thickness of a few monolayers of Ni the magnetisation rotates from in-plane to out-of-plane. At a thickness of several tens of monolayers, a second Spin Reorientation Transition back into the film plane takes place as an effect of the magnetostatic energy and relaxation of lattice strain. Due to the magnetoelastic origin of the perpendicular anisotropy, a Spin Reorientation Transition driven by electric field induced strains was predicted (cf. Section 4.2.1). In Publication VI, a reversible electric field driven magnetisation switching from out-of-plane to in-plane is demonstrated in an epitaxial [Cu(9 nm)/Ni(2 nm)]$_5$/Cu (9 nm)/Fe (1 nm)/$BaTiO_3$ heterostructure grown by MBE. X-ray Diffraction indicates that the $BaTiO_3$ substrate exhibits mainly in-plane domains in the as-deposited state. It also confirms that the large lattice mismatch between the Ni/Cu multilayer and $BaTiO_3$ substrate is relaxed in the heterostructure after sample preparation.
In the as-deposited multilayer, macroscopic in-plane and out-of-plane hysteresis curves confirm the presence of perpendicular magnetic anisotropy.

[8] An instructive overview over growth and electric field induced anisotropies is given in Publication I, Figure 2.

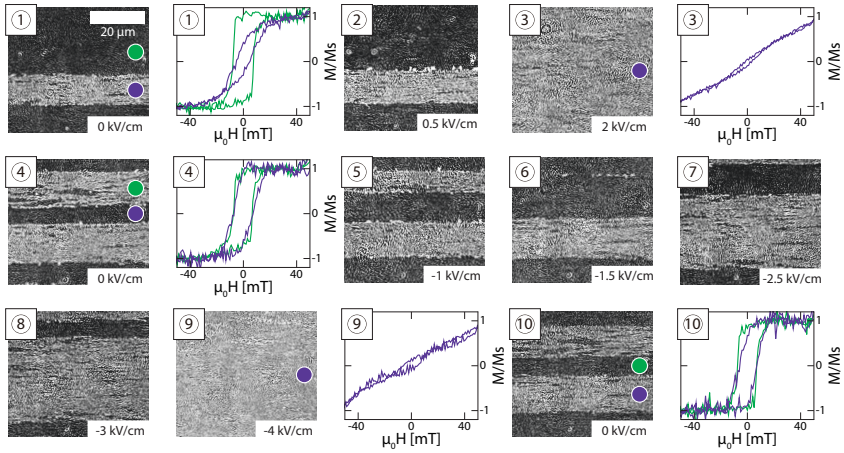

Figure 6.17. Polar MOKE microscopy images of the remanent magnetisation of a Cu/Ni/$BaTiO_3$ heterostructure at several stages of reversible electric field induced magnetisation reorientation. Local out-of-plane hysteresis curves confirm the presence of stripe domains with in-plane and out-of-plane anisotropies.

The application of a large positive or negative out-of-plane electric field ($|E| = 10$ kV/cm) drives the anisotropy direction into the film plane. The perpendicular magnetic anisotropy is restored when the electric field is removed. A series of electric field pulses demonstrates repeatable magnetisation reorientation by 90° between out-of-plane and in-plane (see Figures 2 and 5 in Publication VI).

MOKE microscopy provides images of the magnetic microstructure during the reorientation process. Figure 6.17 presents the evolution of the magnetic domains while cycling an out-of-plane electric field. In the sample, that has a history of applied electric fields, stripe domains with alternating perpendicular and in-plane anisotropy are observed (①). The application of an out-of-plane electric field switches the magnetisation fully into the plane via lateral growth of magnetic domains (②,③). Stripe domains exhibiting perpendicular magnetic anisotropy reappear when the electric field is turned off (④). However, strong domain coupling can be observed in the corresponding hysteresis curves. In a reverse electric field, magnetic domains exhibiting perpendicular anisotropy first grow (⑤,⑥) via lateral domain wall motion. The process suddenly reverses (⑦,⑧) and the subsequent growth of in-plane magnetised domains saturates the multilayer in-plane (⑨). The magnetic microstructure relaxes into a configuration exhibiting stripe domains with alternating anisotropies when the electric field is turned off (⑩).

The observed evolution of the magnetic microstructure is explained by interfacial strain transfer from ferroelectric stripe domains in the $BaTiO_3$

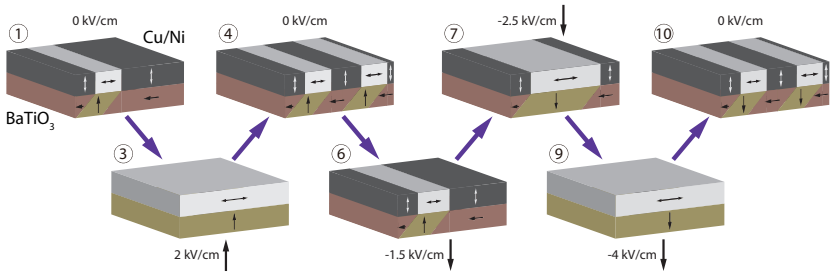

Figure 6.18. Sketch of the ferroelectric and ferromagnetic domain structures corresponding to the images of Figure 6.17.

substrate. In the as-deposited state, no strain transfer is expected and the multilayer and substrate are decoupled. After an out-of-plane electric field is applied, the substrate that was polarised mainly in-plane exhibits alternating a–c stripe domains. The associated change in lattice constant is largely transferred to the multilayer, as it is firmly clamped to the substrate. This electric field induced strain compresses the multilayer on top of c-domains and opposes the growth induced tensile strain that induces perpendicular magnetic anisotropy in the Ni layers. As a result, the magnetisation is reoriented from perpendicular to in-plane. The Ni/Cu multilayer thus exhibits perpendicular magnetic anisotropy on top of ferroelectric a-domains and in-plane anisotropy on top of ferroelectric c-domains.

Figure 6.18 illustrates the coupled ferroelectric/ferromagnetic domain configuration of the images in Figure 6.17. Initially, the $BaTiO_3$ substrate exhibits an a–c stripe domain structure with corresponding out-of-plane and in-plane magnetised domains in the Cu/Ni multilayer (①). In an electric field applied along the polarisation in the c-domains, these grow and eventually a uniform c state is obtained with an in-plane anisotropy in the Cu/Ni multilayer (③). After removal of the electric field, the substrate relaxes back into a multi-domain state (④). In an electric field applied opposite the polarisation in the c-domains, these domains shrink while a-domains grow (⑥). Eventually, the polarisation in the c-domains reverses abruptly to align with the external field direction. Subsequently, c-domains grow at the expense of a-domains (⑦) until a uniform state is again reached (⑨). Although the direction of the electric polarisation is reversed with respect to the situation in sketch (③), the anisotropy in the Cu/Ni multilayer is the same. Finally, the multilayer relaxes back into the a–c domain structure (⑩).

Due to the aforementioned relaxation of strain during growth, no do-

main coupling is expected in the as-grown heterostructure. The choice of $BaTiO_3$ substrate with an initial in-plane domain structure is thus crucial in order to obtain the electric field control of magnetic domains presented here. In publication VI, the interpretation of experimental results is corroborated by theoretical analysis.

6.4 Reversible Electric Field Driven Magnetic Domain Wall Motion

In Section 6.3 electric field control of domain patterns was presented for two distinct multiferroic heterostructures. However, due to – at best – partial strain transfer during thin film growth, electric field induced strains are superimposed onto growth induced strains. As a result, accurate control of magnetic domain wall motion could not be obtained. Here I report on deterministic and reversible electric field driven magnetic domain wall motion in an epitaxial Fe/$BaTiO_3$ heterostructure without the help of magnetic fields or spin polarised currents [V]. Full strain transfer and imprinting of ferroelectric a–c domain patterns into the Fe film are already presented in Publication III.

For this study, 20 nm thick Fe films are grown onto single-crystal $BaTiO_3$ substrates using MBE at 300°C. The deposition results in epitaxial Fe films with an in-plane Fe$[110]$ || $BaTiO_3[100]$ alignment of the cubic crystal lattices as observed commonly [284, 289, 408] and confirmed both by RHEED (not shown) and Transmission Electron Microscopy (cf. Publication III, Figure 1 (b) & (c)). Upon cooling through the ferroelectric phase transition regular a–c domains are formed in the substrate. The sketch in Figure 6.19(b) illustrates that due to full strain transfer the in-plane lattice of Fe is compressed uniformly on top of c-domains by 1.6% with respect to its bulk structure. Nonetheless, the lattice remains cubic. On top of ferroelectric a-domains, the Fe lattice experiences different compressive strains of 1.6% and 0.6% along its diagonals due to the tetragonality of the $BaTiO_3$ lattice. The Fe lattice thus exhibits a diamond shape. The heterostructure is illustrated in Figure 6.19(a). Out-of-plane electric fields are applied in the MOKE microscope during imaging by contacting the backside of the substrate with double-sided copper tape and using the Fe film (and Au capping layer) as the top electrode.

The cubic Fe lattice on top of ferroelectric c-domains is rotated by 45° with respect to the domain boundary and so are the anisotropy axes as confirmed by the polar plot in Figure 6.20(a). It also shows the presence

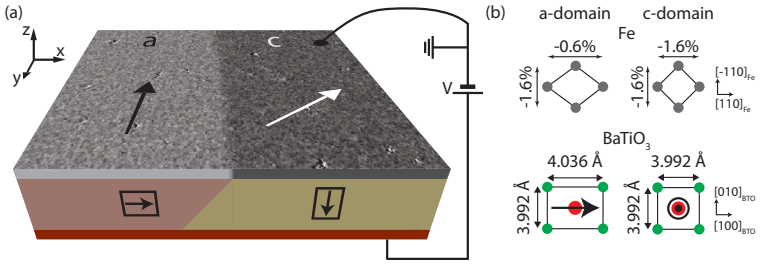

Figure 6.19. (a) Schematic illustration with MOKE microscopy image of the epitaxial Fe/$BaTiO_3$ heterostructure exhibiting ferroelectric a- and c-domains. The direction of ferroelectric polarisation and magnetisation in the substrate and film, respectively, is indicated by arrows. (b) Sketch of the in-plane lattices and ferroelectric polarisation of the Fe film and $BaTiO_3$ substrate.

of a uniaxial anisotropy on top of a-domains that is parallel to the domain boundary. This result is explained by the fact that the negative magnetostriction constant of Fe induces a magnetic easy axis perpendicular to the lattice elongation [19]. Again, the abrupt change in orientation and symmetry of the magnetic anisotropy at the position of the ferroelectric domain boundary strongly pins the magnetic domain wall onto its ferroelectric counterpart (c.f Figures 1 (c) and 2 of Publication V).

As a side note, I would like to mention that the angular dependence of the switching fields presented in Figure 6.20(b) – for the case of relatively narrow domains – shows strong coupling in applied magnetic fields. This confirms the claim from Section 2.7 that the angular dependence of the remanent magnetisation (Figure 6.20(a)) is a better measure for determining the symmetry – and presence – of magnetic anisotropies. The results presented in the following are measured in the absence of an external magnetic field and two relatively wide domains were selected.

The application of an electric field to the $BaTiO_3$ substrate moves the ferroelectric domain boundaries as discussed in Section 3.3.2. The displace-

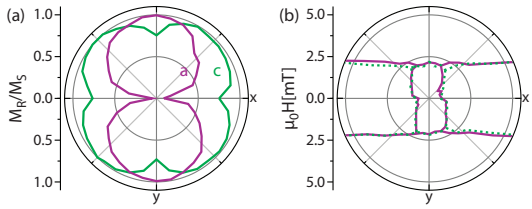

Figure 6.20. (a) Angular dependence of the remanent magnetisation on top of the a-domain (violet line) and c-domain (green line) in Figure 6.19(a). A comparison of the polar plots with the predictions of the Stoner–Wohlfarth model in Figures 2.10(b) and 2.11(b) confirms the presence and orientation of a uniaxial and cubic anisotropy in the respective domains. (b) The angular dependence of the switching fields on a- and c-domains does not fit the Stoner–Wohlfarth model in Figures 2.10(a) and 2.11(a) demonstrating strong domain coupling in applied magnetic fields.

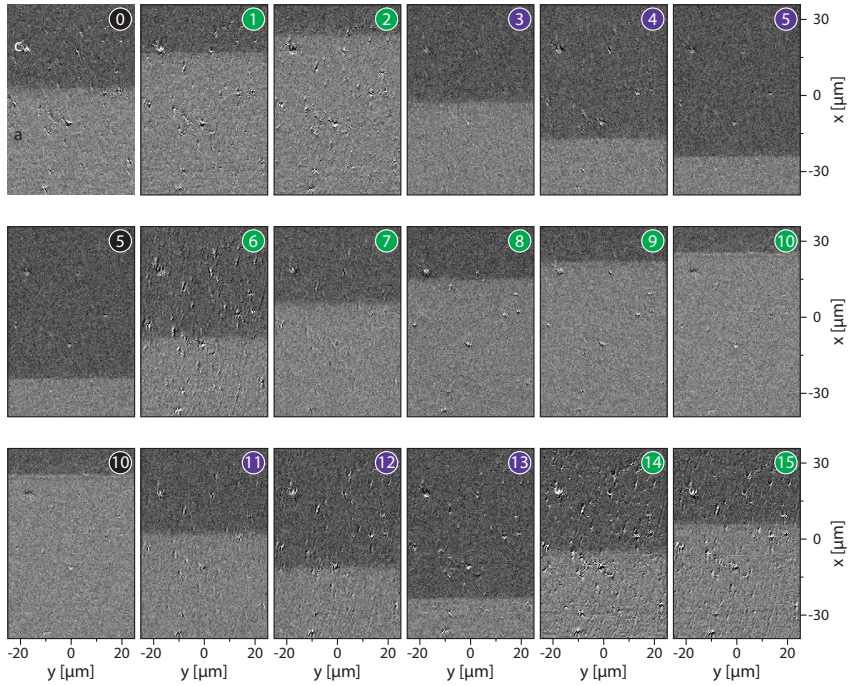

Figure 6.21. MOKE microscopy images demonstrating reversible motion of magnetic domain walls in an Fe/$BaTiO_3$ heterostructure by the application of positive (green circles) and negative (violet circles) electric field pulses ($|E| = 2$ kV/cm) across the substrate. Images where no electric field pulse was applied after the previous image are marked with black circles.

ment of the associated anisotropy boundary and the pinning potential it creates is used to drive a magnetic domain wall by a series of voltage pulses. Figure 6.21 presents images showing controlled and reversible electric field driven magnetic domain wall motion at magnetic remanence. An electric field applied along the direction of the ferroelectric polarisation in c-domains (negative polarity of the electric field) grows those domains at the expense of the adjacent a-domains via lateral domain wall motion (downwards in the images). When the electric field is applied antiparallel to the ferroelectric polarisation in c-domains (positive polarity) they shrink, again by lateral domain wall motion (upwards in the images). Strong coupling of the magnetic domain wall onto the ferroelectric domain boundary is crucial for the observed driving mechanism.

In Figure 6.22 the position of the magnetic domain wall as a function of the number of electric field pulses is shown. The domain wall velocity decreases as a function of domain wall displacement from its initial position. This behaviour is intrinsic to the motion of ferroelectric 90° domain walls as explained in Section 3.3.2. The mechanism for electric field driven magnetic domain wall motion relies on the pinning of the domain walls to

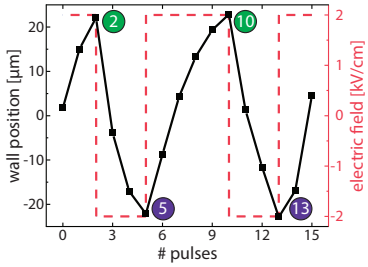

Figure 6.22. Position of the magnetic domain wall corresponding to the images in Figure 6.21 (black line and symbols). The red dashed line indicates the magnitude and polarity of the applied electric field.

their ferroelectric counterpart. The characteristics of the motion are thus fully determined by the ferroelectric subsystem.

The dependence of the average domain wall velocity on the magnitude of the applied electric field is also determined by the properties of the ferroelectric substrate. An exponential dependence of the wall velocity $v \propto exp\,[a/E]$ (with fitting parameter a) over five orders of magnitude is observed (cf. Figure 5 in Publication V). The maximum observed velocity is of the order of 10 µm/s which is orders of magnitude below the theoretically and experimentally possible maximum (see Sections 3.3.1 & 3.3.2). The main obstacle to large wall velocities is given by the thickness of 0.5 mm of the $BaTiO_3$ substrate. As a result, prohibitively large voltages need to be applied in order to obtain the electric fields required for fast domain wall motion. Replacing the thick ferroelectric substrate by a thin film could resolve this problem.

In order for the described driving mechanism of magnetic domain wall motion to be technologically interesting, it needs to function in structures of reduced dimensions, i.e. magnetic nanowires. Micromagnetic simulations are used to investigate fast electric field driven domain wall motion in 200 nm wide and 5 nm thick nanowires patterned at 45° with respect to the anisotropy boundary. The geometry that is simulated using experimentally determined input parameters is sketched in Figure 6.23. The simulations reveal that – because of the competing magnetic shape anisotropy – near to 180° transverse magnetic domain walls are stabilised at rest despite the modest 45° angle between the strain induced anisotropy directions. Fast motion of the anisotropy boundary at v = 300 m/s in either direction does not significantly alter or depin the magnetic domain wall. However, a small out-of-plane magnetisation component develops and increases linearly with the wall velocity. Eventually, the magnetisation tilting reaches a critical value and domain wall

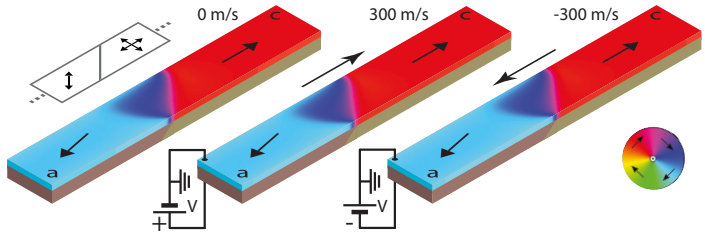

Figure 6.23. Micromagnetic simulations of a magnetic domain wall in a 200 nm wide and 5 nm thick Fe nanowire. The sketch on the upper left illustrates that the nanowire is patterned at 45° with respect to the anisotropy boundary. At rest (and magnetic remanence) a strongly pinned near to 180° domain wall is stabilised. Fast motion (± 300 m/s) of the anisotropy boundary in either direction does not significantly alter the magnetic microstructure of the domain wall.

depinning is observed. Nonetheless, fast domain wall motion is possible for a large parameter space of nanowire dimensions and strain induced anisotropies. As a general rule, magnetisation tilting is suppressed by stronger anisotropies leading to higher depinning velocities. Large strain induced anisotropy strengths are therefore a critical prerequisite for fast electric field induced magnetic domain wall motion.

Finally, I compare the power consumption of electric field and electric current driven magnetic domain wall motion. While Joule heating is the primary source of power dissipation in the current driven case, it is negligible in the field driven case due to the large resistivity of the ferroelectric substrate. The ferroelectric switching process is thus the main source of power dissipation. As a result, the power consumption associated with electric field driven domain wall motion is estimated to be several orders of magnitude lower than for the current driven case, as estimated in Publication V.

7. Conclusions and Outlook

Entscheidend ist, was hinten rauskommt.

Helmut Kohl

In ferromagnetic/ferroelectric heterostructures exhibiting domain pattern transfer, ferromagnetic domain walls are strongly pinned onto their ferroelectric counterpart. This coupling, which forms the basis for the diverse physical phenomena presented in this Thesis, originates in strain transfer from ferroelastic/ferroelectric domain patterns in $BaTiO_3$ substrates to ferromagnetic thin films (polycrystalline $Co_{60}Fe_{40}$, amorphous $Co_{40}Fe_{40}B_{20}$, or epitaxial Fe) or multilayers (epitaxial Cu/Ni). Magnetic anisotropies that differ in symmetry, orientation, and strength depending on the underlying ferroelectric domain are induced into the ferromagnetic films as a result of inverse magnetostriction. Magnetic domain walls are strongly pinned by the resulting narrow anisotropy boundaries.

At remanence, two types of domain walls – uncharged and charged – can be initialised. They have opposite chirality, and their widths differ by one order of magnitude. The application of magnetic fields tunes their properties, and hysteretic switching is demonstrated in a rotating magnetic field. This opens up the possibility of using magnetic domain walls as functional elements. Switching between both domain wall types could be used to store information and their tuning is promising for tunable microwave resonators. The energy difference between charged and uncharged domain walls could be used to implement a reconfigurable logic device utilizing magnetic stripe domains, as proposed recently [409]. In the meantime, the use of pinned domain walls in magnonic devices is already being investigated [299, 410].

Domain pattern transfer scales with the width of ferroelectric domains. When domains become narrower than the width of the magnetic domain walls, domain correlations are lost, limiting the downscaling of domain

wall based magnetic devices. However, as two types of magnetic domain walls can be initialised, two scaling regimes emerge. Again, the rotation of an external magnetic field allows switching between both regimes. At the correct combination of domain width and film thickness the repeated writing and erasing of magnetic domains is thus possible. The two types of pinned magnetic domain walls also lead to a dependence of magnetisation reversal on the direction of the applied magnetic field. In order to avoid high energy charged domain walls, switching in neighbouring stripe domains occurs either simultaneously or at different fields depending on the direction of the applied magnetic field. Even negative switching fields are observed.

The main appeal of multiferroic heterostructures is the possibility of controlling magnetic properties with electric fields. The application of an electric field across the ferroelectric substrate alters the strains imposed on the overlaying ferromagnetic film. Hence, magnetic domain patterns can be rewritten in in-plane magnetised heterostructures. In Cu/Ni multilayers, strain is at the origin of a perpendicular magnetic anisotropy. Electric field control of ferroelectric-ferroelastic domains in a $BaTiO_3$ substrate also allows for the rewriting of stripe domains that alter between an in-plane and an out-of-plane magnetisation.

Finally, reversible electric field driven domain wall motion is demonstrated. The controlled motion is fully repeatable and is also based on pinning of magnetic domain walls onto their ferroelectric counterpart. The velocity of magnetic domain walls increases exponentially as a function of out-of-plane electric field. This novel driving mechanism functions without the concurrent use of electric currents or magnetic fields. Meanwhile, investigations of the dynamics of this driving mechanism have been published [411, 412]. They show rich physics with different dynamic regimes that include the emission of spin waves and the depinning of magnetic domain walls at high velocities.

The results presented here have been obtained for a large variety of elastically coupled multiferroic heterostructures. Moreover, they have been independently confirmed for different material systems. The possibilities and limitations discussed here are thus widely applicable and have spawned further research. The various consequences of elastic domain wall coupling in ferromagnetic/ferroelectric heterostructures investigated in this Thesis hold the promise of new low power spintronic devices.

Bibliography

[1] Dennis Upper. The unsuccessful self-treatment of a case of "writer's block". *Journal of Applied Behavior Analysis*, 7:497, 1974.

[2] S.A. Wolf, D.D. Awschalom, R.A. Buhrman, J.M. Daughton, S. von Molnár, M.L. Roukes, A.Y. Chtchelkanova, and D.M. Treger. Spintronics: A Spin-Based Electronics Vision for the Future. *Science*, 294:1488–1495, 2001.

[3] C. Chappert, A. Fert, and F.N. Van Dau. The emergence of spin electronics in data storage. *Nat. Mater.*, 6:813–823, 2007.

[4] S.S.P. Parkin, M. Hayashi, and L. Thomas. Magnetic Domain-Wall Racetrack Memory. *Science*, 320:190 –194, 2008.

[5] M. Hayashi, L. Thomas, R. Moriya, C. Rettner, and S.S.P. Parkin. Current-Controlled Magnetic Domain-Wall Nanowire Shift Register. *Science*, 320:209–211, 2008.

[6] S. Parkin and S.-H. Yang. Memory on the racetrack. *Nat. Nanotechnol.*, 10:195–198, 2015.

[7] J.T. Heron, D.G. Schlom, and R. Ramesh. Electric field control of magnetism using $BiFeO_3$-based heterostructures. *Appl. Phys. Rev.*, 1:021303, 2014.

[8] C. Kittel. Physical Theory of Ferromagnetic Domains. *Rev. Mod. Phys.*, 21:541, 1949.

[9] N.A. Hill. Density Functional Studies of Multiferroic Magnetoelectrics. *Annu. Rev. Mater. Res.*, 32:1–37, 2002.

[10] N.A. Hill. Why Are There so Few Magnetic Ferroelectrics? *J. Phys. Chem. B*, 104:6694–6709, 2000.

[11] D. Jiles. *Introduction to Magnetism and Magnetic Materials*. Chapman and Hall, 1990.

[12] D. Rodbell and C. Bean. Some Properties of the Coercive Force in Soft Magnetic Materials. *Phys. Rev.*, 103:886–895, 1956.

[13] J. Stöhr and H.C. Siegmann. *Magnetism: From Fundamentals to Nanoscale Dynamics*. Springer, 2006.

[14] R. Skomski. *Simple Models of Magnetism*. Oxford Graduate Texts, 2012.

[15] F. Hund. *Linienspektren und Periodisches System der Elemente*. Springer, 1927.

[16] P. Langevin. Sur la théorie du magnétisme. *J. Phys. Théor. Appl.*, 4:678–693, 1905.

[17] W. Pauli Jr. Über Gasentartung und Paramagnetismus. *Z. Phys.*, 41:81–102, 1927.

[18] T. Kimura. Spiral Magnets as Magnetoelectrics. *Annu. Rev. Mater. Res.*, 37:387–413, 2007.

[19] R.C. O'Handley. *Modern Magnetic Materials: Principles and Applications*. Wiley, 1999.

[20] A. Hubert and R. Schäfer. *Magnetic domains: the analysis of magnetic microstructures*. Springer, 1998.

[21] W.A. Brown. *Micromagnetics*. Interscience Publishers, 1963.

[22] J. Fidler and T. Schrefl. Micromagnetic modelling - the current state of the art. *J. Phys. D: Appl. Phys.*, 33:R135, 2000.

[23] W.A. Brown. Micromagnetics : Successor to domain theory ? *J. Phys. Radium*, 20:101–104, 1959.

[24] W. Heisenberg. Zur Theorie des Ferromagnetismus. *Z. Phys.*, 49:619–636, 1928.

[25] J.C. Slater. The Ferromagnetism of Nickel. *Phys. Rev.*, 49:537–545, 1936.

[26] E.C. Stoner. Collective Electron Ferromagnetism. *Proc. R. Soc. A*, 165:372–414, 1938.

[27] C.A.F Vaz, J. Hoffman, C.H. Ahn, and R. Ramesh. Magnetoelectric Coupling Effects in Multiferroic Complex Oxide Composite Structures. *Adv. Mater.*, 22:2900–2918, 2010.

[28] A. Aharoni. *Introduction to the Theory of Ferromagnetism*. Clarendon Press, 2nd edition, 2001.

[29] P. Weiss. La variation du ferromagnétisme avec la température. *C. R. Acad. Sci.*, 143:1136–1139, 1906.

[30] P. Weiss. L'hypothèse du champ moléculaire et la propriété ferromagnétique. *J. Phys. Théor. Appl.*, 6:661–690, 1907.

[31] N.D. Mermin and H. Wagner. Absence of Ferromagnetism or Antiferromagnetism in One- or Two-Dimensional Isotropic Heisenberg Models. *Phys. Rev. Lett.*, 17:1133–1136, 1966.

[32] P.W. Anderson. More Is Different. *Science*, 177:393–396, 1972.

[33] M.T. Johnson, P.J.H. Bloemen, F.J.A. den Broeder, and J.J. de Vries. Magnetic anisotropy in metallic multilayers. *Rep. Prog. Phys.*, 59:1409–1458, 1996.

[34] H. Brooks. Ferromagnetic Anisotropy and the Itinerant Electron Model. *Phys. Rev.*, 58:909–918, 1940.

[35] J.H. van Vleck. On the Anisotropy of Cubic Ferromagnetic Crystals. *Phys. Rev.*, 52:1178–1198, 1937.

[36] Y. Suzuki, J. Haimovich, and T. Egami. Bond-orientational anisotropy in metallic glasses observed by x-ray diffraction. *Phys. Rev. B*, 35:2162–2168, 1987.

[37] X. Yan, M. Hirscher, T. Egami, and E.E. Marinero. Direct observation of anelastic bond-orientational anisotropy in amorphous $Tb_{26}Fe_{62}Co_{12}$ thin films by x-ray diffraction. *Phys. Rev. B*, 43:9300–9303, 1991.

[38] H. Fu and M. Mansuripur. Boltzmann distribution of bond orientations and perpendicular anisotropy in amorphous rare-earth–transition-metal films. *Phys. Rev. B*, 45:7188–7195, 1992.

[39] V.G. Harris, K.D. Aylesworth, B.N. Das, W.T. Elam, and N.C. Koon. Structural origins of magnetic anisotropy in sputtered amorphous Tb-Fe films. *Phys. Rev. Lett.*, 69:1939–1942, 1992.

[40] A.T. Hindmarch, A.W. Rushforth, R.P. Campion, C.H. Marrows, and B.L. Gallagher. Origin of in-plane uniaxial magnetic anisotropy in CoFeB amorphous ferromagnetic thin films. *Phys. Rev. B*, 83:212404, 2011.

[41] E.W. Lee. Magnetostriction and Magnetomechanical Effects. *Rep. Prog. Phys.*, 18:184, 1955.

[42] X.Z. Lu, X. Wu, and H.J. Xiang. General microscopic model of magnetoelastic coupling from first principles. *Phys. Rev. B*, 91:100405, 2015.

[43] M. Fähnle and T. Egami. Phenomenological theory of magnetostriction in amorphous ferromagnets. *J. Appl. Phys.*, 53:2319–2320, 1982.

[44] D. Sander. The correlation between mechanical stress and magnetic anisotropy in ultrathin films. *Rep. Prog. Phys.*, 62:809, 1999.

[45] H.B. Callen and N. Goldberg. Magnetostriction of Polycrystalline Aggregates. *J. Appl. Phys.*, 36:976–977, 1965.

[46] L. Néel. Anisotropie magnétique superficielle et surstructures d'orientation. *J. Phys. Radium*, 15:225–239, 1954.

[47] D. Weller, J.E.E. Baglin, A.J. Kellock, K.A. Hannibal, M.F. Toney, G. Kusinski, S. Lang, L. Folks, M.E. Best, and B.D. Terris. Ion induced magnetization reorientation in Co/Pt multilayers for patterned media. *J. Appl. Phys.*, 87:5768–5770, 2000.

[48] B. Schulz and K. Baberschke. Crossover from in-plane to perpendicular magnetization in ultrathin Ni/Cu(001) films. *Phys. Rev. B*, 50:13467–13471, 1994.

[49] W.L. O'Brien, T. Droubay, and B.P. Tonner. Transitions in the direction of magnetism in Ni/Cu(001) ultrathin films and the effects of capping layers. *Phys. Rev. B*, 54:9297–9303, 1996.

[50] G.Y. Guo. Strain, interdiffusion, magnetism and magnetic anisotropy in Cu/Ni/Cu(001) sandwiches. *J. Magn. Magn. Mater.*, 176:97–110, 1997.

[51] W.H. Meiklejohn and C.P. Bean. New Magnetic Anisotropy. *Phys. Rev.*, 102:1413–1414, 1956.

[52] W.H. Meiklejohn. Exchange Anisotropy – A Review. *J. Appl. Phys.*, 33:1328–1335, 1962.

[53] A.E. Berkowitz and K. Takano. Exchange anisotropy – a review. *J. Magn. Magn. Mater.*, 200:552–570, 1999.

[54] J. Nogués and I.K. Schuller. Exchange bias. *J. Magn. Magn. Mater.*, 192:203–232, 1999.

[55] F. Radu and H. Zabel. Exchange bias effect of ferro-/antiferromagnetic heterostructures. *arXiv:0705.2055 [cond-mat]*, 227:97–184, 2008.

[56] T.L. Gilbert. A phenomenological theory of damping in ferromagnetic materials. *IEEE Trans. Magn.*, 40:3443–3449, 2004.

[57] J. Shibata, G. Tatara, and H. Kohno. A brief review of field- and current-driven domain-wall motion. *J. Phys. D: Appl. Phys.*, 44:384004, 2011.

[58] C. Chappert, H. Bernas, J. Ferré, V. Kottler, J.-P. Jamet, Y. Chen, E. Cambril, T. Devolder, F. Rousseaux, V. Mathet, and H. Launois. Planar Patterned Magnetic Media Obtained by Ion Irradiation. *Science*, 280:1919–1922, 1998.

[59] J. McCord, T. Gemming, L. Schultz, J. Fassbender, M.O. Liedke, M. Frommberger, and E. Quandt. Magnetic anisotropy and domain patterning of amorphous films by He-ion irradiation. *Appl. Phys. Lett.*, 86:162502, 2005.

[60] J. Trützschler, K. Sentosun, M. Langer, I. Mönch, R. Mattheis, J. Fassbender, and J. McCord. Optimization of magneto-resistive response of ion-irradiated exchange biased films through zigzag arrangement of magnetization. *J. Appl. Phys.*, 115:103901, 2014.

[61] S.I. Woods, S. Ingvarsson, J.R. Kirtley, H.F. Hamann, and R.H. Koch. Local magnetic anisotropy control in NiFe thin films via ion irradiation. *Appl. Phys. Lett.*, 81:1267–1269, 2002.

[62] J.H. Franken, H.J.M. Swagten, and B. Koopmans. Shift registers based on magnetic domain wall ratchets with perpendicular anisotropy. *Nat. Nanotechnol.*, 7:499–503, 2012.

[63] J.H. Franken, M. Hoeijmakers, R. Lavrijsen, J.T. Kohlhepp, H.J.M. Swagten, B. Koopmans, E. van Veldhoven, and D.J. Maas. Precise control of domain wall injection and pinning using helium and gallium focused ion beams. *J. Appl. Phys.*, 109:07D504, 2011.

[64] S.P. Li, W.S. Lew, J.A.C. Bland, L. Lopez-Diaz, C.A.F. Vaz, M. Natali, and Y. Chen. Magnetic Domain Confinement by Anisotropy Modulation. *Phys. Rev. Lett.*, 88:087202, 2002.

[65] A. Berger and H.P. Oepen. Magnetic domain walls in ultrathin fcc cobalt films. *Phys. Rev. B*, 45:12596–12599, 1992.

[66] A. Hubert. Charged walls in thin magnetic films. *IEEE Trans. Magn.*, 15:1251–1260, 1979.

[67] Y. Nozaki, K. Matsuyama, T. Ono, and H. Miyajima. Micromagnetic Structure Analysis of Head-on-Head-Type 180° Domain Wall in Submicron Size Co Wires. *Jpn. J. Appl. Phys.*, 38:6282–6286, 1999.

[68] M. Kläui, C.A.F. Vaz, J.A.C. Bland, L.J. Heyderman, F. Nolting, A. Pavlovska, E. Bauer, S. Cherifi, S. Heun, and A. Locatelli. Head-to-head domain-wall phase diagram in mesoscopic ring magnets. *Appl. Phys. Lett.*, 85:5637–5639, 2004.

[69] B.A. Lilley. LXXI. Energies and widths of domain boundaries in ferromagnetics. *Philos. Mag.*, 41:792–813, 1950.

[70] J.P. Jakubovics. Comments on the definition of ferromagnetic domain wall width. *Philos. Mag. B*, 38:401–406, 1978.

[71] M. Kataja and S. van Dijken. Magneto-optical Kerr effect susceptometer for the analysis of magnetic domain wall dynamics. *Rev. Sci. Instrum.*, 82:103901, 2011.

[72] C.E. Patton. Mobility and Loss Mechanisms for Domain Wall Motion in Thin Ferromagnetic Films. *J. Appl. Phys.*, 37:4269, 1966.

[73] N.L. Schryer and L.R. Walker. The motion of 180° domain walls in uniform dc magnetic fields. *J. Appl. Phys.*, 45:5406, 1974.

[74] K. Kondou, N. Ohshima, D. Chiba, S. Kasai, K. Kobayashi, and T. Ono. Experimental detection of domain wall propagation above the Walker field. *J. Phys. Condens. Matter*, 24:024217, 2012.

[75] T. Ono, H. Miyajima, K. Shigeto, K. Mibu, N. Hosoito, and T. Shinjo. Propagation of a Magnetic Domain Wall in a Submicrometer Magnetic Wire. *Science*, 284:468–470, 1999.

[76] A. Himeno, T. Okuno, T. Ono, K. Mibu, S. Nasu, and T. Shinjo. Temperature dependence of depinning fields in submicron magnetic wires with an artificial neck. *J. Magn. Magn. Mater.*, 286:167–170, 2005.

[77] K. Shigeto, T. Shinjo, and T. Ono. Injection of a magnetic domain wall into a submicron magnetic wire. *Appl. Phys. Lett.*, 75:2815, 1999.

[78] G.S.D. Beach, C. Nistor, C. Knutson, M. Tsoi, and J.L. Erskine. Dynamics of field-driven domain-wall propagation in ferromagnetic nanowires. *Nat. Mater.*, 4:741–744, 2005.

[79] M. Yan, C. Andreas, A. Kákay, F. García-Sánchez, and R. Hertel. Fast domain wall dynamics in magnetic nanotubes: Suppression of Walker breakdown and Cherenkov-like spin wave emission. *Appl. Phys. Lett.*, 99:122505, 2011.

[80] D. Atkinson, D.A. Allwood, G. Xiong, M.D. Cooke, C.C. Faulkner, and R.P. Cowburn. Magnetic domain-wall dynamics in a submicrometre ferromagnetic structure. *Nat. Mater.*, 2:85–87, 2003.

[81] E.R. Lewis, D. Petit, L. O'Brien, A. Fernandez-Pacheco, J. Sampaio, A.-V. Jausovec, H. T. Zeng, D.E. Read, and R.P. Cowburn. Fast domain wall motion in magnetic comb structures. *Nat. Mater.*, 9:980–983, 2010.

[82] G. Malinowski, O. Boulle, and M. Kläui. Current-induced domain wall motion in nanoscale ferromagnetic elements. *J. Phys. D: Appl. Phys.*, 44:384005, 2011.

[83] D. Chiba, G. Yamada, T. Koyama, K. Ueda, H. Tanigawa, S. Fukami, T. Suzuki, N. Ohshima, N. Ishiwata, Y. Nakatani, and T. Ono. Control of Multiple Magnetic Domain Walls by Current in a Co/Ni Nano-Wire. *Appl. Phys. Express*, 3:073004, 2010.

[84] G. Tatara, H. Kohno, and J. Shibata. Microscopic approach to current-driven domain wall dynamics. *Phys. Rep.*, 468:213–301, 2008.

[85] L. Berger. Low-field magnetoresistance and domain drag in ferromagnets. *J. Appl. Phys.*, 49:2156–2161, 1978.

[86] J.C. Slonczewski. Current-driven excitation of magnetic multilayers. *J. Magn. Magn. Mater.*, 159:L1–L7, 1996.

[87] M.D. Stiles and J. Miltat. Spin-Transfer Torque and Dynamics. In B. Hillebrands and A. Thiaville, editors, *Spin Dynamics in Confined Magnetic Structures III*, pages 225–308. Springer, 2006.

[88] L. Berger. Exchange interaction between ferromagnetic domain wall and electric current in very thin metallic films. *J. Appl. Phys.*, 55:1954–1956, 1984.

[89] A. Yamaguchi, S. Nasu, H. Tanigawa, T. Ono, K. Miyake, K. Mibu, and T. Shinjo. Effect of Joule heating in current-driven domain wall motion. *Appl. Phys. Lett.*, 86:012511, 2005.

[90] M. Kläui, H. Ehrke, U. Rüdiger, T. Kasama, R.E. Dunin-Borkowski, D. Backes, L.J. Heyderman, C.A.F. Vaz, J.A.C. Bland, G. Faini, E. Cambril, and W. Wernsdorfer. Direct observation of domain-wall pinning at nanoscale constrictions. *Appl. Phys. Lett.*, 87:102509, 2005.

[91] S.-H. Yang, K.-S. Ryu, and S. Parkin. Domain-wall velocities of up to 750 m s^{-1} driven by exchange-coupling torque in synthetic antiferromagnets. *Nat. Nanotechnol.*, 10:221–226, 2015.

[92] K.-J. Kim, R. Hiramatsu, T. Koyama, K. Ueda, Y. Yoshimura, D. Chiba, K. Kobayashi, Y. Nakatani, S. Fukami, M. Yamanouchi, H. Ohno, H. Kohno, G. Tatara, and T. Ono. Two-barrier stability that allows low-power operation in current-induced domain-wall motion. *Nat. Commun.*, 4, 2013.

[93] G. Meier, M. Bolte, R. Eiselt, B. Krüger, D.-H. Kim, and P. Fischer. Direct Imaging of Stochastic Domain-Wall Motion Driven by Nanosecond Current Pulses. *Phys. Rev. Lett.*, 98:187202, 2007.

[94] M. Feigenson, J.W. Reiner, and L. Klein. Efficient Current-Induced Domain-Wall Displacement in $SrRuO_3$. *Phys. Rev. Lett.*, 98:247204, 2007.

[95] M. Tsoi, R.E. Fontana, and S.S.P. Parkin. Magnetic domain wall motion triggered by an electric current. *Appl. Phys. Lett.*, 83:2617, 2003.

[96] G. Tatara and H. Kohno. Theory of Current-Driven Domain Wall Motion: Spin Transfer versus Momentum Transfer. *Phys. Rev. Lett.*, 92, 2004.

[97] S. Emori, U. Bauer, S.-M. Ahn, E. Martinez, and G.S.D. Beach. Current-driven dynamics of chiral ferromagnetic domain walls. *Nat. Mater.*, 12:611–616, 2013.

[98] I. Dzyaloshinsky. A thermodynamic theory of "weak" ferromagnetism of antiferromagnetics. *J. Phys. Chem. Solids*, 4:241–255, 1958.

[99] T. Moriya. Anisotropic Superexchange Interaction and Weak Ferromagnetism. *Phys. Rev.*, 120:91–98, 1960.

[100] D. Bedau, M. Kläui, U. Rüdiger, C.A.F. Vaz, J. A.C. Bland, G. Faini, L. Vila, and W. Wernsdorfer. Angular dependence of the depinning field for head-to-head domain walls at constrictions. *J. Appl. Phys.*, 101:09F509, 2007.

[101] H. Barkhausen. Zwei mit Hilfe der Neuen Verstärker entdeckte Erscheinungen. *Phys. Z.*, 20:401–403, 1919.

[102] D. Ravelosona, F. Cayssol, J. Wunderlich, H.W. Schumacher, C. Chappert, V. Mathet, J. Ferré, and J.-P. Jamet. Dynamics of magnetization reversal in a mesoscopic wire. *J. Magn. Magn. Mater.*, 249:170–174, 2002.

[103] D. Bedau, M. Kläui, M.T. Hua, S. Krzyk, U. Rüdiger, G. Faini, and L. Vila. Quantitative Determination of the Nonlinear Pinning Potential for a Magnetic Domain Wall. *Phys. Rev. Lett.*, 101:256602, 2008.

[104] D. Petit, A.-V. Jausovec, D. Read, and R.P. Cowburn. Domain wall pinning and potential landscapes created by constrictions and protrusions in ferromagnetic nanowires. *J. Appl. Phys.*, 103:114307, 2008.

[105] L.K. Bogart, D. Atkinson, K. O'Shea, D. McGrouther, and S. McVitie. Dependence of domain wall pinning potential landscapes on domain wall chirality and pinning site geometry in planar nanowires. *Phys. Rev. B*, 79:054414, 2009.

[106] M.-Y. Im, L. Bocklage, P. Fischer, and G. Meier. Direct Observation of Stochastic Domain-Wall Depinning in Magnetic Nanowires. *Phys. Rev. Lett.*, 102:147204, 2009.

[107] E.R. Lewis, D. Petit, L. Thevenard, A.V. Jausovec, L. O'Brien, D.E. Read, and R.P. Cowburn. Magnetic domain wall pinning by a curved conduit. *Appl. Phys. Lett.*, 95:152505, 2009.

[108] A. Himeno, S. Kasai, and T. Ono. Current-driven domain-wall motion in magnetic wires with asymmetric notches. *Appl. Phys. Lett.*, 87:243108, 2005.

[109] D.A. Allwood, G. Xiong, and R.P. Cowburn. Domain wall diodes in ferromagnetic planar nanowires. *Appl. Phys. Lett.*, 85:2848–2850, 2004.

[110] M.T. Bryan, T. Schrefl, and D.A. Allwood. Symmetric and asymmetric domain wall diodes in magnetic nanowires. *Appl. Phys. Lett.*, 91:142502, 2007.

[111] J. Sampaio, L. O'Brien, D. Petit, D.E. Read, E.R. Lewis, H.T. Zeng, L. Thevenard, S. Cardoso, and R.P. Cowburn. Coupling and induced depinning of magnetic domain walls in adjacent spin valve nanotracks. *J. Appl. Phys.*, 113:133901, 2013.

[112] J.H. Franken, M.A.J. van der Heijden, T.H. Ellis, R. Lavrijsen, C. Daniels, D. McGrouther, H.J.M. Swagten, and B. Koopmans. Beam-Induced Fe Nanopillars as Tunable Domain-Wall Pinning Sites. *Adv. Funct. Mater.*, 24:3508–3514, 2014.

[113] P.-O. Jubert, R. Allenspach, and A. Bischof. Magnetic domain walls in constrained geometries. *Phys. Rev. B*, 69:220410, 2004.

[114] Z.J. Yang, L. Sun, X.P. Zhang, M. Cao, X.Y. Deng, A. Hu, and H.F. Ding. Control of ultranarrow Co magnetic domain wall widths in artificially patterned H-bar structures. *Appl. Phys. Lett.*, 94:062514, 2009.

[115] G. Chen, T. Ma, A.T. N'Diaye, H. Kwon, C. Won, Y. Wu, and A.K. Schmid. Tailoring the chirality of magnetic domain walls by interface engineering. *Nat. Commun.*, 4, 2013.

[116] G. Chen, A.T. N'Diaye, S.P. Kang, H.Y. Kwon, C. Won, Y. Wu, Z.Q. Qiu, and A.K. Schmid. Unlocking Bloch-type chirality in ultrathin magnets through uniaxial strain. *Nat. Commun.*, 6, 2015.

[117] D.A. Allwood, G. Xiong, C.C. Faulkner, D. Atkinson, D. Petit, and R.P. Cowburn. Magnetic Domain-Wall Logic. *Science*, 309:1688–1692, 2005.

[118] J.H. Franken, R. Lavrijsen, J.T. Kohlhepp, H.J.M. Swagten, and B. Koopmans. Tunable magnetic domain wall oscillator at an anisotropy boundary. *Appl. Phys. Lett.*, 98:102512, 2011.

[119] E. Martinez, L. Torres, and L. Lopez-Diaz. Oscillator based on pinned domain walls driven by direct current. *Phys. Rev. B*, 83, 2011.

[120] E.C. Stoner and E.P. Wohlfarth. A Mechanism of Magnetic Hysteresis in Heterogeneous Alloys. *Phil. Trans. R. Soc. A*, 240:599–642, 1948.

[121] D. Damjanovic. Ferroelectric, dielectric and piezoelectric properties of ferroelectric thin films and ceramics. *Rep. Prog. Phys.*, 61:1267, 1998.

[122] N.A. Spaldin. Analogies and Differences between Ferroelectrics and Ferromagnets. In K.M. Rabe, C.H. Ahn, and J.-M. Triscone, editors, *Physics of Ferroelectrics*, pages 175–218. Springer, 2007.

[123] M.E. Lines and A.M. Glass. *Principles and Applications of Ferroelectrics and Related Materials*. Clarendon Press, 1979.

[124] K.M. Rabe, M. Dawber, C. Lichtensteiger, C.H. Ahn, and J.-M. Triscone. Modern Physics of Ferroelectrics: Essential Background. In K.M. Rabe, C.H. Ahn, and J.-M. Triscone, editors, *Physics of Ferroelectrics*, pages 1–30. Springer, 2007.

[125] C.A.F. Vaz. Electric field control of magnetism in multiferroic heterostructures. *J. Phys. Condens. Matter*, 24:333201, 2012.

[126] D.I. Khomskii. Multiferroics: Different ways to combine magnetism and ferroelectricity. *J. Magn. Magn. Mater.*, 306:1–8, 2006.

[127] A.K. Tagantsev, L.E. Cross, and J. Fousek. *Domains in Ferroic Crystals and Thin Films*. Springer, 2010.

[128] R.K. Vasudevan, D. Marincel, S. Jesse, Y. Kim, A. Kumar, S.V. Kalinin, and S. Trolier-McKinstry. Polarization Dynamics in Ferroelectric Capacitors: Local Perspective on Emergent Collective Behavior and Memory Effects. *Adv. Funct. Mater.*, 23:2490–2508, 2013.

[129] J. Valasek. Piezo-Electric and Allied Phenomena in Rochelle Salt. *Phys. Rev.*, 17:475–481, 1921.

[130] W. Gilbert. *De Magnete*. Peter Short, 1600.

[131] L.E. Cross. Ferroelectric Ceramics: Tailoring Properties for Specific Applications. In N. Setter and E.L. Colla, editors, *Ferroelectric Ceramics*, pages 1–85. Birkhäuser, 1993.

[132] S. Pöykkö and D.J. Chadi. Ab initio study of 180° domain wall energy and structure in $PbTiO_3$. *Appl. Phys. Lett.*, 75:2830, 1999.

[133] H.H. Wieder. Electrical Behavior of Barium Titanatge Single Crystals at Low Temperatures. *Phys. Rev.*, 99:1161–1165, 1955.

[134] J.J. Wang, P.P. Wu, X.Q. Ma, and L.Q. Chen. Temperature-pressure phase diagram and ferroelectric properties of $BaTiO_3$ single crystal based on a modified Landau potential. *J. Appl. Phys.*, 108:114105, 2010.

[135] W. Zhong, R.D. King-Smith, and D. Vanderbilt. Giant LO-TO splittings in perovskite ferroelectrics. *Phys. Rev. Lett.*, 72:3618–3621, 1994.

[136] J.P. Boyeaux and F.M. Michel-Calendini. Small polaron interpretation of $BaTiO_3$ transport properties from drift mobility measurements. *J. Phys. C*, 12:545, 1979.

[137] K.-I. Sakayori, Y. Matsui, H. Abe, E. Nakamura, M. Kenmoku, T. Hara, D. Ishikawa, A. Kokubu, K.-I. Hirota, and T. Ikeda. Curie Temperature of $BaTiO_3$. *Jpn. J. Appl. Phys.*, 34:5443, 1995.

[138] A. Kvasov. *High-order electromechanical couplings in ferroelectrics*. PhD thesis, EPFL, Lausanne, 2014.

[139] M. Dawber, K.M. Rabe, and J.F. Scott. Physics of thin-film ferroelectric oxides. *Rev. Mod. Phys.*, 77:1083–1130, 2005.

[140] M.M. Vijatovic, J.D. Bobic, and B.D. Stojanovic. History and challenges of barium titanate: Part I. *Sci. Sinter.*, 40:155–165, 2008.

[141] G.H. Kwei, A.C. Lawson, S.J.L. Billinge, and S.W. Cheong. Structures of the ferroelectric phases of barium titanate. *J. Phys. Chem.*, 97:2368–2377, 1993.

[142] Y.G. Wang, J. Dec, and W. Kleemann. Study on surface and domain structures of $PbTiO_3$ crystals by atomic force microscopy. *J. Appl. Phys.*, 84:6795–6799, 1998.

[143] B. Matthias and A. von Hippel. Domain Structure and Dielectric Response of Barium Titanate Single Crystals. *Phys. Rev.*, 73:1378–1384, 1948.

[144] J.P. Velev, S.S. Jaswal, and E.Y. Tsymbal. Multi-ferroic and magnetoelectric materials and interfaces. *Phil. Trans. R. Soc. A*, 369:3069–3097, 2011.

[145] R.E. Cohen. Theory of ferroelectrics: a vision for the next decade and beyond. *J. Phys. Chem. Solids*, 61:139–146, 2000.

[146] J. Schwarzkopf and R. Fornari. Epitaxial growth of ferroelectric oxide films. *Prog. Cryst. Growth Charact. Mater.*, 52:159–212, 2006.

[147] R.E. Cohen. Origin of ferroelectricity in perovskite oxides. *Nature*, 358:136–138, 1992.

[148] R.E. Cohen and H. Krakauer. Electronic structure studies of the differences in ferroelectric behavior of $BaTiO_3$ and $PbTiO_3$. *Ferroelectrics*, 136:65–83, 1992.

[149] W. Zhong, D. Vanderbilt, and K.M. Rabe. Phase Transitions in $BaTiO_3$ from First Principles. *Phys. Rev. Lett.*, 73:1861–1864, 1994.

[150] J. Fousek. Ferroelectric Domains: Some Recent Advances. In N. Setter and E.L. Colla, editors, *Ferroelectric Ceramics*, pages 87–105. Birkhäuser, 1993.

[151] A.H.G. Vlooswijk, B. Noheda, G. Catalan, A. Janssens, B. Barcones, G. Rijnders, D.H.A. Blank, S. Venkatesan, B. Kooi, and J.T.M. de Hosson. Smallest 90° domains in epitaxial ferroelectric films. *Appl. Phys. Lett.*, 91:112901, 2007.

[152] P.W. Forsbergh. Domain Structures and Phase Transitions in Barium Titanate. *Phys. Rev.*, 76:1187–1201, 1949.

[153] I. Luk'yanchuk, A. Schilling, J. Gregg, G. Catalan, and J. Scott. Origin of ferroelastic domains in free-standing single-crystal ferroelectric films. *Phys. Rev. B*, 79, 2009.

[154] W.J. Merz. Domain Formation and Domain Wall Motions in Ferroelectric $BaTiO_3$ Single Crystals. *Phys. Rev.*, 95:690, 1954.

[155] G. Catalan, J. Seidel, R. Ramesh, and J.F. Scott. Domain wall nanoelectronics. *Rev. Mod. Phys.*, 84:119–156, 2012.

[156] N. Setter, D. Damjanovic, L. Eng, G. Fox, S. Gevorgian, S. Hong, A. Kingon, H. Kohlstedt, N.Y. Park, G.B. Stephenson, I. Stolitchnov, A.K. Taganstev, D.V. Taylor, T. Yamada, and S. Streiffer. Ferroelectric thin films: Review of materials, properties, and applications. *J. Appl. Phys.*, 100:051606, 2006.

[157] L.W. Martin, Y.-H. Chu, and R. Ramesh. Advances in the growth and characterization of magnetic, ferroelectric, and multiferroic oxide thin films. *Mater. Sci. Eng. R Rep.*, 68:89–133, 2010.

[158] S.V. Kalinin and D.A. Bonnell. Effect of phase transition on the surface potential of the $BaTiO_3$ (100) surface by variable temperature scanning surface potential microscopy. *J. Appl. Phys.*, 87:3950–3957, 2000.

[159] M.D. Dennis and R.C. Bradt. Thickness of 90° ferroelectric domain walls in (Ba,Pb)TiO_3 single crystals. *J. Appl. Phys.*, 45:1931–1933, 1974.

[160] J. Hlinka and P. Márton. Phenomenological model of a 90° domain wall in $BaTiO_3$-type ferroelectrics. *Phys. Rev. B*, 74, 2006.

[161] M.M. Vijatovic, J.D. Bobic, and B.D. Stojanovic. History and challenges of barium titanate: Part II. *Sci. Sinter.*, 40:235–244, 2008.

[162] E. Little. Dynamic Behavior of Domain Walls in Barium Titanate. *Phys. Rev.*, 98:978–984, 1955.

[163] A.L. Gruverman, J. Hatano, and H. Tokumoto. Scanning Force Microscopy Studies of Domain Structure in $BaTiO_3$ Single Crystals. *Jpn. J. Appl. Phys.*, 36:2207, 1997.

[164] J. Padilla, W. Zhong, and D. Vanderbilt. First-principles investigation of 180° domain walls in $BaTiO_3$. *Phys. Rev. B*, 53:R5969–R5973, 1996.

[165] L. McGilly, D. Byrne, C. Harnagea, A. Schilling, and J.M. Gregg. Imaging domains in $BaTiO_3$ single crystal nanostructures: comparing information from transmission electron microscopy and piezo-force microscopy. *J. Mater. Sci.*, 44:5197–5204, 2009.

[166] B. Meyer and D. Vanderbilt. Ab initio study of ferroelectric domain walls in $PbTiO_3$. *Phys. Rev. B*, 65:104111, 2002.

[167] Q. Zhang and W.A. Goddard. Charge and polarization distributions at the 90° domain wall in barium titanate ferroelectric. *Appl. Phys. Lett.*, 89:182903, 2006.

[168] X. Zhang, T. Hashimoto, and D.C. Joy. Electron holographic study of ferroelectric domain walls. *Appl. Phys. Lett.*, 60:784, 1992.

[169] E. Edlund and M.N. Jacobi. Universality of Striped Morphologies. *Phys. Rev. Lett.*, 105:137203, 2010.

[170] Z. Chen, J. Liu, Y. Qi, D. Chen, S.-L. Hsu, A.R. Damodaran, X. He, A.T. N'Diaye, A. Rockett, and L.W. Martin. 180° Ferroelectric Stripe Nanodomains in $BiFeO_3$ Thin Films. *Nano Lett.*, 15:6506–6513, 2015.

[171] S.K. Streiffer, J.A. Eastman, D.D. Fong, C. Thompson, A. Munkholm, M.V. Ramana Murty, O. Auciello, G.R. Bai, and G.B. Stephenson. Observation of Nanoscale 180° Stripe Domains in Ferroelectric $PbTiO_3$ Thin Films. *Phys. Rev. Lett.*, 89:067601, 2002.

[172] Y. Ivry, D. Chu, and C. Durkan. Nanometer resolution piezoresponse force microscopy to study deep submicron ferroelectric and ferroelastic domains. *Appl. Phys. Lett.*, 94:162903, 2009.

[173] J. Muñoz-Saldaña, G.A. Schneider, and L.M. Eng. Stress induced movement of ferroelastic domain walls in $BaTiO_3$ single crystals evaluated by scanning force microscopy. *Surf. Sci.*, 480:L402–L410, 2001.

[174] M. Takashige, S.-I. Hamazaki, N. Fukurai, F. Shimizu, and S. Kojima. Atomic Force Microscope Observation of Ferroelectrics: Barium Titanate and Rochelle Salt. *Jpn. J. Appl. Phys.*, 35:5181–5184, 1996.

[175] T. Mitsui and J. Furuichi. Domain Structure of Rochelle Salt and KH_2PO_4. *Phys. Rev.*, 90:193–202, 1953.

[176] N. Balke, M. Gajek, A.K. Tagantsev, L.W. Martin, Y.-H. Chu, R. Ramesh, and S.V. Kalinin. Direct Observation of Capacitor Switching Using Planar Electrodes. *Adv. Funct. Mater.*, 20:3466–3475, 2010.

[177] J.F. Scott and C.A. Paz de Araujo. Ferroelectric Memories. *Science*, 246:1400–1405, 1989.

[178] Y. Kim, X. Lu, S. Jesse, D. Hesse, M. Alexe, and S.V. Kalinin. Universality of Polarization Switching Dynamics in Ferroelectric Capacitors Revealed by 5d Piezoresponse Force Microscopy. *Adv. Funct. Mater.*, 23:3971–3979, 2013.

[179] C.T. Nelson, P. Gao, J.R. Jokisaari, C. Heikes, C. Adamo, A. Melville, S.-H. Baek, C.M. Folkman, B. Winchester, Y. Gu, Y. Liu, K. Zhang, E. Wang, J. Li, L.-Q. Chen, C.-B. Eom, D.G. Schlom, and X. Pan. Domain Dynamics During Ferroelectric Switching. *Science*, 334:968–971, 2011.

[180] E.-J. Guo, R. Roth, A. Herklotz, D. Hesse, and K. Dörr. Ferroelectric 180° Domain Wall Motion Controlled by Biaxial Strain. *Adv. Mater.*, 27:1615–1618, 2015.

[181] P. Gao, C.T. Nelson, J.R. Jokisaari, S.-H. Baek, C.W. Bark, Y. Zhang, E. Wang, D.G. Schlom, C.-B. Eom, and X. Pan. Revealing the role of defects in ferroelectric switching with atomic resolution. *Nat. Commun.*, 2:591, 2011.

[182] W.J. Merz. Switching Time in Ferroelectric $BaTiO_3$ and Its Dependence on Crystal Thickness. *J. Appl. Phys.*, 27:938–943, 1956.

[183] H.L. Stadler. Forward Velocity of 180° Ferroelectric Domain Walls in $BaTiO_3$. *J. Appl. Phys.*, 37:1947–1948, 1966.

[184] Q. Meng, M.-G. Han, J. Tao, G. Xu, D.O. Welch, and Y. Zhu. Velocity of domain-wall motion during polarization reversal in ferroelectric thin films: Beyond Merz's Law. *Phys. Rev. B*, 91:054104, 2015.

[185] R.C. Miller and A. Savage. Velocity of Sidewise 180° Domain-Wall Motion in $BaTiO_3$ as a Function of the Applied Electric Field. *Phys. Rev.*, 112:755–762, 1958.

[186] R.C. Miller and A. Savage. Further Experiments on the Sidewise Motion of 180° Domain Walls in $BaTiO_3$. *Phys. Rev.*, 115:1176–1180, 1959.

[187] R. Miller and G. Weinreich. Mechanism for the Sidewise Motion of 180° Domain Walls in Barium Titanate. *Phys. Rev.*, 117:1460–1466, 1960.

[188] H.L. Stadler and P.J. Zachmanidis. Nucleation and Growth of Ferroelectric Domains in $BaTiO_3$ at Fields from 2 to 450 kV/cm. *J. Appl. Phys.*, 34:3255–3260, 1963.

[189] A. Savage and R.C. Miller. Temperature Dependence of the Velocity of Sidewise 180° Domain-Wall Motion in $BaTiO_3$. *J. Appl. Phys.*, 31:1546–1549, 1960.

[190] J. Y. Son and S. M. Yoon. Fast ferroelectric domain wall motion in $BiAlO_3$. *Ceram. Int.*, 39:4031–4034, 2013.

[191] A. Gruverman, D. Wu, and J.F. Scott. Piezoresponse Force Microscopy Studies of Switching Behavior of Ferroelectric Capacitors on a 100-ns Time Scale. *Phys. Rev. Lett.*, 100:097601, 2008.

[192] J. Li, B. Nagaraj, H. Liang, W. Cao, C.H. Lee, and R. Ramesh. Ultrafast polarization switching in thin-film ferroelectrics. *Appl. Phys. Lett.*, 84:1174–1176, 2004.

[193] Y.-H. Shin, I. Grinberg, I-W. Chen, and A.M. Rappe. Nucleation and growth mechanism of ferroelectric domain-wall motion. *Nature*, 449:881–884, 2007.

[194] L. He and D. Vanderbilt. First-principles study of oxygen-vacancy pinning of domain walls in $PbTiO_3$. *Phys. Rev. B*, 68:134103, 2003.

[195] L. Hong, A.K. Soh, Q.G. Du, and J.Y. Li. Interaction of O vacancies and domain structures in single crystal $BaTiO_3$: Two-dimensional ferroelectric model. *Phys. Rev. B*, 77:094104, 2008.

[196] D. Lee, B.C. Jeon, A. Yoon, Y.J. Shin, M.H. Lee, T.K. Song, S.D. Bu, M. Kim, J.-S. Chung, J.-G. Yoon, and T.W. Noh. Flexoelectric Control of Defect Formation in Ferroelectric Epitaxial Thin Films. *Adv. Mater.*, 26:5005–5011, 2014.

[197] J.F. Scott and M. Dawber. Oxygen-vacancy ordering as a fatigue mechanism in perovskite ferroelectrics. *Appl. Phys. Lett.*, 76:3801–3803, 2000.

[198] K.J. Choi, M. Biegalski, Y.L. Li, A. Sharan, J. Schubert, R. Uecker, P. Reiche, Y.B. Chen, X.Q. Pan, V. Gopalan, L.-Q. Chen, D.G. Schlom, and C.B. Eom. Enhancement of Ferroelectricity in Strained $BaTiO_3$ Thin Films. *Science*, 306:1005–1009, 2004.

[199] J. Fousek and B. Březina. The movement of single 90° domain walls of $BaTiO_3$ in an alternating electric field. *Czech. J. Phys.*, 10:511–528, 1960.

[200] J. Fousek and B. Březina. Relaxation of 90° Domain Walls of $BaTiO_3$ and Their Equation of Motion. *J. Phys. Soc. Jpn.*, 19:830–838, 1964.

[201] T. Tsurumi, Y. Kumano, N. Ohashi, T. Takenaka, and O. Fukunaga. 90° Domain Reorientation and Electric-Field-Induced Strain of Tetragonal Lead Zirconate Titanate Ceramics. *Jpn. J. Appl. Phys.*, 36:5970, 1997.

[202] M.H. Lente, A. Picinin, J.P. Rino, and J.A. Eiras. 90° domain wall relaxation and frequency dependence of the coercive field in the ferroelectric switching process. *J. Appl. Phys.*, 95:2646–2653, 2004.

[203] T. Sluka, A.K. Tagantsev, P. Bednyakov, and N. Setter. Free-electron gas at charged domain walls in insulating $BaTiO_3$. *Nat. Commun.*, 4:1808, 2013.

[204] A. Schilling, T.B. Adams, R.M. Bowman, J.M. Gregg, G. Catalan, and J.F. Scott. Scaling of domain periodicity with thickness measured in $BaTiO_3$ single crystal lamellae and comparison with other ferroics. *Phys. Rev. B*, 74:024115, 2006.

[205] F. Tsai and J.M. Cowley. Thickness dependence of ferroelectric domains in thin crystalline films. *Appl. Phys. Lett.*, 65:1906–1908, 1994.

[206] R. Takahashi, Ø. Dahl, E. Eberg, J.K. Grepstad, and T. Tybell. Ferroelectric stripe domains in $PbTiO_3$ thin films: Depolarization field and domain randomness. *J. Appl. Phys.*, 104:064109, 2008.

[207] A. Schilling, R.M. Bowman, J.M. Gregg, G. Catalan, and J.F. Scott. Ferroelectric domain periodicities in nanocolumns of single crystal barium titanate. *Appl. Phys. Lett.*, 89:212902, 2006.

[208] G. Catalan, A. Schilling, J.F. Scott, and J.M. Gregg. Domains in three-dimensional ferroelectric nanostructures: theory and experiment. *J. Phys. Condens. Matter*, 19:132201, 2007.

[209] J.R. Whyte and J.M. Gregg. A diode for ferroelectric domain-wall motion. *Nat. Commun.*, 6, 2015.

[210] J.R. Whyte, R.G.P. McQuaid, P. Sharma, C. Canalias, J.F. Scott, A. Gruverman, and J.M. Gregg. Ferroelectric Domain Wall Injection. *Adv. Mater.*, 26:293–298, 2014.

[211] M. McMillen, R.G.P. McQuaid, S.C. Haire, C.D. McLaughlin, L.W. Chang, A. Schilling, and J.M. Gregg. The influence of notches on domain dynamics in ferroelectric nanowires. *Appl. Phys. Lett.*, 96:042904, 2010.

[212] R.G.P. McQuaid, L.-W. Chang, and J.M. Gregg. The Effect of Antinotches on Domain Wall Mobility in Single Crystal Ferroelectric Nanowires. *Nano Lett.*, 10:3566–3571, 2010.

[213] L.J. McGilly, P. Yudin, L. Feigl, A.K. Tagantsev, and N. Setter. Controlling domain wall motion in ferroelectric thin films. *Nat. Nanotechnol.*, 10:145–150, 2015.

[214] H. Schmid. Multi-ferroic magnetoelectrics. *Ferroelectrics*, 162:317–338, 1994.

[215] M. Fiebig. Revival of the magnetoelectric effect. *J. Phys. D: Appl. Phys.*, 38:R123, 2005.

[216] W. Eerenstein, N.D. Mathur, and J.F. Scott. Multiferroic and magnetoelectric materials. *Nature*, 442:759–765, 2006.

[217] C.-W. Nan, M.I. Bichurin, S. Dong, D. Viehland, and G. Srinivasan. Multiferroic magnetoelectric composites: Historical perspective, status, and future directions. *J. Appl. Phys.*, 103:031101, 2008.

[218] F. Matsukura, Y. Tokura, and H. Ohno. Control of magnetism by electric fields. *Nat. Nanotechnol.*, 10:209–220, 2015.

[219] J.F. Scott. Room-temperature multiferroic magnetoelectrics. *NPG Asia Mater.*, 5:e72, 2013.

[220] V. Garcia, M. Bibes, and A. Barthélémy. Artificial multiferroic heterostructures for an electric control of magnetic properties. *C. R. Phys.*, 16:168–181, 2015.

[221] J.-M. Hu, L.-Q. Chen, and C.-W. Nan. Multiferroic Heterostructures Integrating Ferroelectric and Magnetic Materials. *Adv. Mater.*, 28:15–39, 2015.

[222] S. Fusil, V. Garcia, A. Barthélémy, and M. Bibes. Magnetoelectric Devices for Spintronics. *Annu. Rev. Mater. Res.*, 44:91–116, 2014.

[223] N. Mathur. Materials science: A desirable wind up. *Nature*, 454:591–592, 2008.

[224] V. Laukhin, V. Skumryev, X. Martí, D. Hrabovsky, F. Sánchez, M. García-Cuenca, C. Ferrater, M. Varela, U. Lüders, J. Bobo, and J. Fontcuberta. Electric-Field Control of Exchange Bias in Multiferroic Epitaxial Heterostructures. *Phys. Rev. Lett.*, 97:227201, 2006.

[225] B.B. van Aken, T.T.M. Palstra, A. Filippetti, and N.A. Spaldin. The origin of ferroelectricity in magnetoelectric $YMnO_3$. *Nat. Mater.*, 3:164–170, 2004.

[226] BB. van Aken, A. Meetsma, and T.T.M. Palstra. Hexagonal $YMnO_3$. *Acta Crystallogr. Sect. C Cryst. Struct. Commun.*, 57:230–232, 2001.

[227] M. Fiebig, D. Fröhlich, K. Kohn, S. Leute, T. Lottermoser, V.V. Pavlov, and R.V. Pisarev. Determination of the Magnetic Symmetry of Hexagonal Manganites by Second Harmonic Generation. *Phys. Rev. Lett.*, 84:5620–5623, 2000.

[228] G. Catalan and J.F. Scott. Physics and Applications of Bismuth Ferrite. *Adv. Mater.*, 21:2463–2485, 2009.

[229] J. van den Brink and D.I. Khomskii. Multiferroicity due to charge ordering. *J. Phys. Condens. Matter*, 20:434217, 2008.

[230] M. Baum, J. Leist, T. Finger, K. Schmalzl, A. Hiess, L.P. Regnault, P. Becker, L. Bohatý, G. Eckold, and M. Braden. Kinetics of the multiferroic switching in $MnWO_4$. *Phys. Rev. B*, 89:144406, 2014.

[231] D. Niermann, C.P. Grams, P. Becker, L. Bohatý, H. Schenck, and J. Hemberger. Critical Slowing Down near the Multiferroic Phase Transition in $MnWO_4$. *Phys. Rev. Lett.*, 114:037204, 2015.

[232] F. Kagawa, M. Mochizuki, Y. Onose, H. Murakawa, Y. Kaneko, N. Furukawa, and Y. Tokura. Dynamics of Multiferroic Domain Wall in Spin-Cycloidal Ferroelectric $DyMnO_3$. *Phys. Rev. Lett.*, 102:057604, 2009.

[233] M. Kenzelmann, G. Lawes, A.B. Harris, G. Gasparovic, C. Broholm, A.P. Ramirez, G.A. Jorge, M. Jaime, S. Park, Q. Huang, A.Y. Shapiro, and L.A. Demianets. Direct Transition from a Disordered to a Multiferroic Phase on a Triangular Lattice. *Phys. Rev. Lett.*, 98:267205, 2007.

[234] N. Hur, S. Park, P.A. Sharma, J.S. Ahn, S. Guha, and S.-W. Cheong. Electric polarization reversal and memory in a multiferroic material induced by magnetic fields. *Nature*, 429:392–395, 2004.

[235] Y. Tokura, S. Seki, and N. Nagaosa. Multiferroics of spin origin. *Rep. Prog. Phys.*, 77:076501, 2014.

[236] Y. Wang, J. Hu, Y. Lin, and C.-W. Nan. Multiferroic magnetoelectric composite nanostructures. *NPG Asia Mater.*, 2:61–68, 2010.

[237] J.-Y. Kim, L. Yao, and S. van Dijken. Coherent piezoelectric strain transfer to thick epitaxial ferromagnetic films with large lattice mismatch. *J. Phys. Condens. Matter*, 25:082205, 2013.

[238] S.T.B. Goennenwein. Voltage-controlled spin mechanics. *Europhysics News*, 41:17–20, 2010.

[239] X.L. Zhong, J.B. Wang, M. Liao, G.J. Huang, S.H. Xie, Y.C. Zhou, Y. Qiao, and J.P. He. Multiferroic nanoparticulate $Bi_{3.15}Nd_{0.85}Ti_3O_{12}$-$CoFe_2O_4$ composite thin films prepared by a chemical solution deposition technique. *Appl. Phys. Lett.*, 90:152903, 2007.

[240] H. Ryu, P. Murugavel, J.H. Lee, S.C. Chae, T.W. Noh, Y.S. Oh, H.J. Kim, K.H. Kim, J.H. Jang, M. Kim, C. Bae, and J.-G. Park. Magnetoelectric effects of nanoparticulate $Pb(Zr_{0.52}Ti_{0.48})O_3$–$NiFe_2O_4$ composite films. *Appl. Phys. Lett.*, 89:102907, 2006.

[241] J. Zhai, N. Cai, Z. Shi, Y. Lin, and C.-W. Nan. Magnetic-dielectric properties of $NiFe_2O_4$/PZT particulate composites. *J. Phys. D: Appl. Phys.*, 37:823, 2004.

[242] F. Zavaliche, H. Zheng, L. Mohaddes-Ardabili, S.Y. Yang, Q. Zhan, P. Shafer, E. Reilly, R. Chopdekar, Y. Jia, P. Wright, D.G. Schlom, Y. Suzuki, and R. Ramesh. Electric Field-Induced Magnetization Switching in Epitaxial Columnar Nanostructures. *Nano Lett.*, 5:1793–1796, 2005.

[243] Z. Shi, C.W. Nan, J. Zhang, N. Cai, and J.-F. Li. Magnetoelectric effect of $Pb(Zr,Ti)O_3$ rod arrays in a $(Tb,Dy)Fe_2$/epoxy medium. *Appl. Phys. Lett.*, 87:012503, 2005.

[244] D. Dale, A. Fleet, J.D. Brock, and Y. Suzuki. Dynamically tuning properties of epitaxial colossal magnetoresistance thin films. *Appl. Phys. Lett.*, 82:3725–3727, 2003.

[245] C.A.F. Vaz, F.J. Walker, C.H. Ahn, and S. Ismail-Beigi. Intrinsic interfacial phenomena in manganite heterostructures. *J. Phys. Condens. Matter*, 27:123001, 2015.

[246] S. Geprägs, A. Brandlmaier, M. Opel, R. Gross, and S.T.B. Goennenwein. Electric field controlled manipulation of the magnetization in Ni/$BaTiO_3$ hybrid structures. *Appl. Phys. Lett.*, 96:142509, 2010.

[247] S. Geprägs, D. Mannix, M. Opel, S.T.B. Goennenwein, and R. Gross. Converse magnetoelectric effects in Fe_3O_4/$BaTiO_3$ multiferroic hybrids. *Phys. Rev. B*, 88:054412, 2013.

[248] S. Finizio, M. Foerster, M. Buzzi, B. Krüger, M. Jourdan, C.A.F. Vaz, J. Hockel, T. Miyawaki, A. Tkach, S. Valencia, F. Kronast, G.P. Carman, F. Nolting, and M. Kläui. Magnetic Anisotropy Engineering in Thin Film Ni Nanostructures by Magnetoelastic Coupling. *Phys. Rev. Appl.*, 1:021001, 2014.

[249] M. Liu, O. Obi, J. Lou, Y. Chen, Z. Cai, S. Stoute, M. Espanol, M. Lew, X. Situ, K.S. Ziemer, V.G. Harris, and N.X. Sun. Giant Electric Field Tuning of Magnetic Properties in Multiferroic Ferrite/Ferroelectric Heterostructures. *Adv. Funct. Mater.*, 19:1826–1831, 2009.

[250] T. Wu, A. Bur, K. Wong, P. Zhao, C.S. Lynch, P.K. Amiri, K.L. Wang, and G.P. Carman. Electrical control of reversible and permanent magnetization reorientation for magnetoelectric memory devices. *Appl. Phys. Lett.*, 98:262504, 2011.

[251] H.K.D. Kim, L.T. Schelhas, S. Keller, J.L. Hockel, S.H. Tolbert, and G.P. Carman. Magnetoelectric Control of Superparamagnetism. *Nano Lett.*, 13:884–888, 2013.

[252] K. Dörr, O. Bilani-Zeneli, A. Herklotz, A.D. Rata, K. Boldyreva, J.-W. Kim, M.C. Dekker, K. Nenkov, L. Schultz, and M. Reibold. A model system for strain effects: epitaxial magnetic films on a piezoelectric substrate. *EPJ B*, 71:361–366, 2009.

[253] S.F. Rus, A. Herklotz, R. Roth, L. Schultz, and K. Dörr. Thickness dependence of the magnetoelastic effect of $CoFe_2O_4$ films grown on piezoelectric substrates. *J. Appl. Phys.*, 114:043913, 2013.

[254] C. Thiele, K. Dörr, O. Bilani, J. Rödel, and L. Schultz. Influence of strain on the magnetization and magnetoelectric effect in $La_{0.7}A_{0.3}MnO_3$/PMN-PT(001) (A = Sr,Ca). *Phys. Rev. B*, 75, 2007.

[255] S. Li, Q. Xue, H. Du, J. Xu, Q. Li, Z. Shi, X. Gao, M. Liu, T. Nan, Z. Hu, N.X. Sun, and W. Shao. Large E-field tunability of magnetic anisotropy and ferromagnetic resonance frequency of co-sputtered $Fe_{50}Co_{50}$-B film. *J. Appl. Phys.*, 117:17D702, 2015.

[256] S.T.B. Goennenwein, M. Althammer, C. Bihler, A. Brandlmaier, S. Geprägs, M. Opel, W. Schoch, W. Limmer, R. Gross, and M.S. Brandt. Piezo-voltage control of magnetization orientation in a ferromagnetic semiconductor. *Phys. Status Solidi Rapid Res. Lett.*, 2:96–98, 2008.

[257] B. Botters, F. Giesen, J. Podbielski, P. Bach, G. Schmidt, L.W. Molenkamp, and D. Grundler. Stress dependence of ferromagnetic resonance and magnetic anisotropy in a thin NiMnSb film on InP(001). *Appl. Phys. Lett.*, 89:242505, 2006.

[258] A. Brandlmaier, M. Brasse, S. Geprägs, M. Weiler, R. Gross, and S.T.B. Goennenwein. Magnetooptical imaging of elastic strain-controlled magnetization reorientation. *EPJ B*, 85:1–8, 2012.

[259] A. Casiraghi, A.W. Rushforth, J. Zemen, J.A. Haigh, M. Wang, K.W. Edmonds, R.P. Campion, and B.L. Gallagher. Piezoelectric strain induced variation of the magnetic anisotropy in a high Curie temperature (Ga,Mn)As sample. *Appl. Phys. Lett.*, 101:082406, 2012.

[260] M. Weiler, A. Brandlmaier, S. Geprägs, M. Althammer, M. Opel, C. Bihler, H. Huebl, M.S. Brandt, R. Gross, and S.T.B. Goennenwein. Voltage controlled inversion of magnetic anisotropy in a ferromagnetic thin film at room temperature. *New J. Phys.*, 11:013021, 2009.

[261] G. Yu, Z. Wang, M. Abolfath-Beygi, C. He, X. Li, K.L. Wong, P. Nordeen, H. Wu, G.P. Carman, X. Han, I.A. Alhomoudi, P.K. Amiri, and K.L. Wang. Strain-induced modulation of perpendicular magnetic anisotropy in Ta/CoFeB/MgO structures investigated by ferromagnetic resonance. *Appl. Phys. Lett.*, 106:072402, 2015.

[262] N. Lei, S. Park, P. Lecoeur, D. Ravelosona, C. Chappert, O. Stelmakhovych, and V. Holý. Magnetization reversal assisted by the inverse piezoelectric effect in Co-Fe-B/ferroelectric multilayers. *Phys. Rev. B*, 84:012404, 2011.

[263] G.A. Lebedev, B. Viala, T. Lafont, D.I. Zakharov, O. Cugat, and J. Delamare. Converse magnetoelectric effect dependence with CoFeB composition in ferromagnetic/piezoelectric composites. *J. Appl. Phys.*, 111:07C725, 2012.

[264] A. Brandlmaier, S. Geprägs, M. Weiler, A. Boger, M. Opel, H. Huebl, C. Bihler, M.S. Brandt, B. Botters, D. Grundler, R. Gross, and S.T.B. Goennenwein. In situ manipulation of magnetic anisotropy in magnetite thin films. *Phys. Rev. B*, 77:104445, 2008.

[265] N.A. Pertsev. Giant magnetoelectric effect via strain-induced spin reorientation transitions in ferromagnetic films. *Phys. Rev. B*, 78:212102, 2008.

[266] N.A. Pertsev. Converse magnetoelectric effect via strain-driven magnetization reorientations in ultrathin ferromagnetic films on ferroelectric substrates. *Phys. Rev. B*, 92:014416, 2015.

[267] J. Ma, Y. Lin, and C.W. Nan. Anomalous electric field-induced switching of local magnetization vector in a simple FeBSiC-on-Pb(Zr,Ti)O_3 multiferroic bilayer. *J. Phys. D: Appl. Phys.*, 43:012001, 2010.

[268] Y. Iwasaki. Stress-driven magnetization reversal in magnetostrictive films with in-plane magnetocrystalline anisotropy. *J. Magn. Magn. Mater.*, 240:395–397, 2002.

[269] J.J. Wang, J.M. Hu, J. Ma, J.X. Zhang, L.Q. Chen, and C.W. Nan. Full 180° Magnetization Reversal with Electric Fields. *Sci. Rep.*, 4, 2014.

[270] R.-C. Peng, J.J. Wang, J.-M. Hu, L.-Q. Chen, and C.-W. Nan. Electric-field-driven magnetization reversal in square-shaped nanomagnet-based multiferroic heterostructure. *Appl. Phys. Lett.*, 106:142901, 2015.

[271] M. Ghidini, R. Pellicelli, J.L. Prieto, X. Moya, J. Soussi, J. Briscoe, S. Dunn, and N.D. Mathur. Non-volatile electrically-driven repeatable magnetization reversal with no applied magnetic field. *Nat. Commun.*, 4:1453, 2013.

[272] J.-M. Hu, T Yang, J. Wang, H. Huang, J. Zhang, L.-Q. Chen, and C.-W. Nan. Purely Electric-Field-Driven Perpendicular Magnetization Reversal. *Nano Lett.*, 15:616–622, 2015.

[273] C. Pettiford, J. Lou, L. Russell, and N.X. Sun. Strong magnetoelectric coupling at microwave frequencies in metallic magnetic film/lead zirconate titanate multiferroic composites. *Appl. Phys. Lett.*, 92:122506, 2008.

[274] J. Lou, M. Liu, D. Reed, Y. Ren, and N.X. Sun. Giant Electric Field Tuning of Magnetism in Novel Multiferroic FeGaB/Lead Zinc Niobate-Lead Titanate (PZN-PT) Heterostructures. *Adv. Mater.*, 21:4711–4715, 2009.

[275] N.N. Phuoc and C.K. Ong. Electric field control of microwave characteristics in composition-graded FeCoTa film grown onto $[Pb(Mg_{1/3}Nb_{2/3})O_3]_{0.68}$-$[PbTiO_3]_{0.32}$(011) crystal. *Appl. Phys. Lett.*, 105:032901, 2014.

[276] S. Shastry, G. Srinivasan, M.I. Bichurin, V.M. Petrov, and A.S. Tatarenko. Microwave magnetoelectric effects in single crystal bilayers of yttrium iron garnet and lead magnesium niobate-lead titanate. *Phys. Rev. B*, 70:064416, 2004.

[277] J. Heidler, C. Piamonteze, R.V. Chopdekar, M.A. Uribe-Laverde, A. Alberca, M. Buzzi, A. Uldry, B. Delley, C. Bernhard, and F. Nolting. Manipulating magnetism in $La_{0.7}Sr_{0.3}MnO_3$ via piezostrain. *Phys. Rev. B*, 91:024406, 2015.

[278] C. Thiele, K. Dörr, S. Fähler, L. Schultz, D.C. Meyer, A.A. Levin, and P. Paufler. Voltage-controlled epitaxial strain in $La_{0.7}Sr_{0.3}MnO_3$/$Pb(Mg_{1/3}Nb_{2/3})O_3$-$PbTiO_3$(001) films. *Appl. Phys. Lett.*, 87:262502, 2005.

[279] A.W. Rushforth, E. De Ranieri, J. Zemen, J. Wunderlich, K.W. Edmonds, C.S. King, E. Ahmad, R.P. Campion, C.T. Foxon, B.L. Gallagher, K. Výborný, J. Kučera, and T. Jungwirth. Voltage control of magnetocrystalline anisotropy in ferromagnetic-semiconductor-piezoelectric hybrid structures. *Phys. Rev. B*, 78:085314, 2008.

[280] T. Dietl and H. Ohno. Dilute ferromagnetic semiconductors: Physics and spintronic structures. *Rev. Mod. Phys.*, 86:187–251, 2014.

[281] S. Sahoo, S. Polisetty, C.-G. Duan, S. Jaswal, E. Tsymbal, and C. Binek. Ferroelectric control of magnetism in $BaTiO_3$/Fe heterostructures via interface strain coupling. *Phys. Rev. B*, 76:092108, 2007.

[282] G. Venkataiah, E. Wada, H. Taniguchi, M. Itoh, and T. Taniyama. Electric-voltage control of magnetism in Fe/$BaTiO_3$ heterostructured multiferroics. *J. Appl. Phys.*, 113:17C701, 2013.

[283] S. Geprägs, M. Opel, S.T.B. Goennenwein, and R. Gross. Giant magnetoelastic effects in $BaTiO_3$-based extrinsic multiferroic hybrids. *Phys. Rev. B*, 86:134432, 2012.

[284] G. Venkataiah, Y. Shirahata, M. Itoh, and T. Taniyama. Manipulation of magnetic coercivity of Fe film in Fe/$BaTiO_3$ heterostructure by electric field. *Appl. Phys. Lett.*, 99:102506, 2011.

[285] R.V. Chopdekar and Y. Suzuki. Magnetoelectric coupling in epitaxial $CoFe_2O_4$ on $BaTiO_3$. *Appl. Phys. Lett.*, 89:182506, 2006.

[286] C.A.F. Vaz, J. Hoffman, A.-B. Posadas, and C.H. Ahn. Magnetic anisotropy modulation of magnetite in Fe_3O_4/$BaTiO_3$(100) epitaxial structures. *Appl. Phys. Lett.*, 94:022504, 2009.

[287] H.F. Tian, T.L. Qu, L.B. Luo, J.J. Yang, S.M. Guo, H.Y. Zhang, Y.G. Zhao, and J.Q. Li. Strain induced magnetoelectric coupling between magnetite and $BaTiO_3$. *Appl. Phys. Lett.*, 92:063507, 2008.

[288] F.D. Czeschka, S. Geprägs, M. Opel, S.T.B. Goennenwein, and R. Gross. Giant magnetic anisotropy changes in Sr_2CrReO_6 thin films on $BaTiO_3$. *Appl. Phys. Lett.*, 95:062508, 2009.

[289] Y. Shirahata, T. Nozaki, G. Venkataiah, H. Taniguchi, M. Itoh, and T. Taniyama. Switching of the symmetry of magnetic anisotropy in Fe/$BaTiO_3$ heterostructures. *Appl. Phys. Lett.*, 99:022501, 2011.

[290] G. Venkataiah, Y. Shirahata, I. Suzuki, M. Itoh, and T. Taniyama. Strain-induced reversible and irreversible magnetization switching in Fe/$BaTiO_3$ heterostructures. *J. Appl. Phys.*, 111:033921, 2012.

[291] G.E. Sterbinsky, B.W. Wessels, J.-W. Kim, E. Karapetrova, P.J. Ryan, and D.J. Keavney. Strain-driven spin reorientation in magnetite/barium titanate heterostructures. *Appl. Phys. Lett.*, 96:092510, 2010.

[292] M.K. Lee, T.K. Nath, C.B. Eom, M.C. Smoak, and F. Tsui. Strain modification of epitaxial perovskite oxide thin films using structural transitions of ferroelectric $BaTiO_3$ substrate. *Appl. Phys. Lett.*, 77:3547–3549, 2000.

[293] M. Ghidini, F. Maccherozzi, X. Moya, L.C. Phillips, W. Yan, J. Soussi, N. Métallier, M.E. Vickers, N.-J. Steinke, R. Mansell, C.H.W. Barnes, S.S. Dhesi, and N.D. Mathur. Perpendicular Local Magnetization Under Voltage Control in Ni Films on Ferroelectric $BaTiO_3$ Substrates. *Adv. Mater.*, 27:1460–1465, 2015.

[294] T.H.E. Lahtinen, J.O. Tuomi, and S. van Dijken. Pattern Transfer and Electric-Field-Induced Magnetic Domain Formation in Multiferroic Heterostructures. *Adv. Mater.*, 23:3187–3191, 2011.

[295] T.H.E. Lahtinen, J.O Tuomi, and S. van Dijken. Electrical Writing of Magnetic Domain Patterns in Ferromagnetic/Ferroelectric Heterostructures. *IEEE Trans. Magn.*, 47:3768–3771, 2011.

[296] R.V. Chopdekar, V.K. Malik, A. Fraile Rodríguez, L. Le Guyader, Y. Takamura, A. Scholl, D. Stender, C.W. Schneider, C. Bernhard, F. Nolting, and L.J. Heyderman. Spatially resolved strain-imprinted magnetic states in an artificial multiferroic. *Phys. Rev. B*, 86:014408, 2012.

[297] R.V. Chopdekar, J. Heidler, C. Piamonteze, Y. Takamura, A. Scholl, S. Rusponi, H. Brune, L.J. Heyderman, and F. Nolting. Strain-dependent magnetic configurations in manganite-titanate heterostructures probed with soft X-ray techniques. *EPJ B*, 86:1–7, 2013.

[298] L.C. Phillips, R.O. Cherifi, V. Ivanovskaya, A. Zobelli, I.C. Infante, E. Jacquet, N. Guiblin, A.A. Ünal, F. Kronast, B. Dkhil, A. Barthélémy, M. Bibes, and S. Valencia. Local electrical control of magnetic order and orientation by ferroelastic domain arrangements just above room temperature. *Sci. Rep.*, 5:10026, 2015.

[299] F. Brandl, K.J.A. Franke, T.H.E. Lahtinen, S. van Dijken, and D. Grundler. Spin waves in CoFeB on ferroelectric domains combining spin mechanics and magnonics. *Solid State Commun.*, 198, 2014.

[300] S.W. Fackler, M.J. Donahue, T. Gao, P.N.A. Nero, S.-W. Cheong, J. Cumings, and I. Takeuchi. Local control of magnetic anisotropy in transcritical permalloy thin films using ferroelectric $BaTiO_3$ domains. *Appl. Phys. Lett.*, 105:212905, 2014.

[301] R. Streubel, D. Köhler, R. Schäfer, and L. Eng. Strain-mediated elastic coupling in magnetoelectric nickel/barium-titanate heterostructures. *Phys. Rev. B*, 87:054410, 2013.

[302] H.T. Chen, Y. Ni, and A.K. Soh. Modeling of ferroelectric control of magnetic domain pattern and domain wall properties. *J. Appl. Phys.*, 113:134102, 2013.

[303] T.N. Yang, J.-M. Hu, C.W. Nan, and L.Q. Chen. On the elastically coupled magnetic and ferroelectric domains: A phase-field model. *Appl. Phys. Lett.*, 104:202402, 2014.

[304] H.T. Chen and A.K. Soh. Precision electric control of magnetic domain wall motions in a multiferroic bilayer based on strain-mediated magnetoelectric coupling. *Mater. Res. Bull.*, 59:42–48, 2014.

[305] W. Eerenstein, M. Wiora, J.L. Prieto, J.F. Scott, and N.D. Mathur. Giant sharp and persistent converse magnetoelectric effects in multiferroic epitaxial heterostructures. *Nat. Mater.*, 6:348–351, 2007.

[306] R.O. Cherifi, V. Ivanovskaya, L.C. Phillips, A. Zobelli, I.C. Infante, E. Jacquet, V. Garcia, S. Fusil, P.R. Briddon, N. Guiblin, A. Mougin, A.A. Ünal, F. Kronast, S. Valencia, B. Dkhil, A. Barthélémy, and M. Bibes. Electric-field control of magnetic order above room temperature. *Nat. Mater.*, 13:345–351, 2014.

[307] T. Dietl, H. Ohno, F. Matsukura, J. Cibert, and D. Ferrand. Zener model description of ferromagnetism in zinc-blende magnetic semiconductors. *Science*, 287:1019–1022, 2000.

[308] T. Jungwirth, J. Sinova, J. Mašek, J. Kucera, and A.H. MacDonald. Theory of ferromagnetic (III,Mn)V semiconductors. *Rev. Mod. Phys.*, 78:809–864, 2006.

[309] M.K. Niranjan, C.-G. Duan, S.S. Jaswal, and E.Y. Tsymbal. Electric field effect on magnetization at the Fe/MgO(001) interface. *Appl. Phys. Lett.*, 96:222504, 2010.

[310] C.-G. Duan, J.P. Velev, R.F. Sabirianov, Z. Zhu, J. Chu, S.S. Jaswal, and E.Y. Tsymbal. Surface Magnetoelectric Effect in Ferromagnetic Metal Films. *Phys. Rev. Lett.*, 101:137201, 2008.

[311] C.-G. Duan, C.-W. Nan, S.S. Jaswal, and E.Y. Tsymbal. Universality of the surface magnetoelectric effect in half-metals. *Phys. Rev. B*, 79:140403, 2009.

[312] C.-G. Duan, S.S. Jaswal, and E.Y. Tsymbal. Predicted Magnetoelectric Effect in Fe/$BaTiO_3$ Multilayers: Ferroelectric Control of Magnetism. *Phys. Rev. Lett.*, 97:047201, 2006.

[313] S. Valencia, A. Crassous, L. Bocher, V. Garcia, X. Moya, R.O. Cherifi, C. Deranlot, K. Bouzehouane, S. Fusil, A. Zobelli, A. Gloter, N.D. Mathur, A. Gaupp, R. Abrudan, F. Radu, A. Barthélémy, and M. Bibes. Interface-induced room-temperature multiferroicity in $BaTiO_3$. *Nat. Mater.*, 10:753–758, 2011.

[314] T. Maruyama, Y. Shiota, T. Nozaki, K. Ohta, N. Toda, M. Mizuguchi, A.A. Tulapurkar, T. Shinjo, M. Shiraishi, S. Mizukami, Y. Ando, and Y. Suzuki. Large voltage-induced magnetic anisotropy change in a few atomic layers of iron. *Nat. Nanotechnol.*, 4:158–161, 2009.

[315] Y. Shiota, S. Murakami, F. Bonell, T. Nozaki, T. Shinjo, and Y. Suzuki. Quantitative Evaluation of Voltage-Induced Magnetic Anisotropy Change by Magnetoresistance Measurement. *Appl. Phys. Express*, 4:043005, 2011.

[316] Y. Shiota, T. Maruyama, T. Nozaki, T. Shinjo, M. Shiraishi, and Y. Suzuki. Voltage-Assisted Magnetization Switching in Ultrathin $Fe_{80}Co_{20}$ Alloy Layers. *Appl. Phys. Express*, 2:063001, 2009.

[317] T. Niazi, M. Cormier, D. Lucot, L. Largeau, V. Jeudy, J. Cibert, and A. Lemaître. Electric-field control of the magnetic anisotropy in an ultrathin (Ga,Mn)As/(Ga,Mn)(As,P) bilayer. *Appl. Phys. Lett.*, 102:122403, 2013.

[318] M. Cormier, V. Jeudy, T. Niazi, D. Lucot, M. Granada, J. Cibert, and A. Lemaître. Electric-field-induced magnetization reorientation in a (Ga,Mn)As/(Ga,Mn)(As,P) bilayer with out-of-plane anisotropy. *Phys. Rev. B*, 90:174418, 2014.

[319] T. Dietl, H. Ohno, and F. Matsukura. Hole-mediated ferromagnetism in tetrahedrally coordinated semiconductors. *Phys. Rev. B*, 63:195205, 2001.

[320] H. Ohno, D. Chiba, F. Matsukura, T. Omiya, E. Abe, T. Dietl, Y. Ohno, and K. Ohtani. Electric-field control of ferromagnetism. *Nature*, 408:944–946, 2000.

[321] D. Chiba, M. Yamanouchi, F. Matsukura, and H. Ohno. Electrical Manipulation of Magnetization Reversal in a Ferromagnetic Semiconductor. *Science*, 301:943–945, 2003.

[322] D. Chiba, M. Sawicki, Y. Nishitani, Y. Nakatani, F. Matsukura, and H. Ohno. Magnetization vector manipulation by electric fields. *Nature*, 455:515–518, 2008.

[323] E. Dagotto, T. Hotta, and A. Moreo. Colossal magnetoresistant materials: the key role of phase separation. *Phys. Rep.*, 344:1–153, 2001.

[324] C.A.F. Vaz, J. Hoffman, Y. Segal, J.W. Reiner, R.D. Grober, Z. Zhang, C.H. Ahn, and F.J. Walker. Origin of the Magnetoelectric Coupling Effect in $Pb(Zr_{0.2}Ti_{0.8})O_3/La_{0.8}Sr_{0.2}MnO_3$ Multiferroic Heterostructures. *Phys. Rev. Lett.*, 104:127202, 2010.

[325] H.J.A. Molegraaf, J. Hoffman, C.A.F. Vaz, S. Gariglio, D. van der Marel, C.H. Ahn, and J.-M. Triscone. Magnetoelectric Effects in Complex Oxides with Competing Ground States. *Adv. Mater.*, 21:3470–3474, 2009.

[326] T. Kanki, H. Tanaka, and T. Kawai. Electric control of room temperature ferromagnetism in a $Pb(Zr_{0.2}Ti_{0.8})O_3/La_{0.85}Ba_{0.15}MnO_3$ field-effect transistor. *Appl. Phys. Lett.*, 89:242506, 2006.

[327] S. Kanai, M. Yamanouchi, S. Ikeda, Y. Nakatani, F. Matsukura, and H. Ohno. Electric field-induced magnetization reversal in a perpendicular-anisotropy CoFeB-MgO magnetic tunnel junction. *Appl. Phys. Lett.*, 101:122403, 2012.

[328] J.-M. Hu, C.-W. Nan, and L.-Q. Chen. Size-dependent electric voltage controlled magnetic anisotropy in multiferroic heterostructures: Interface-charge and strain comediated magnetoelectric coupling. *Phys. Rev. B*, 83:134408, 2011.

[329] L. Shu, Z. Li, J. Ma, Y. Gao, L. Gu, Y. Shen, Y. Lin, and C.W. Nan. Thickness-dependent voltage-modulated magnetism in multiferroic heterostructures. *Appl. Phys. Lett.*, 100:022405, 2012.

[330] T. Nan, Z. Zhou, M. Liu, X. Yang, Y. Gao, B.A. Assaf, H. Lin, S. Velu, X. Wang, H. Luo, J. Chen, S. Akhtar, E. Hu, R. Rajiv, K. Krishnan, S. Sreedhar, D. Heiman, B.M. Howe, G.J. Brown, and N.X. Sun. Quantification of strain and charge co-mediated magnetoelectric coupling on ultra-thin Permalloy/PMN-PT interface. *Sci. Rep.*, 4:3688, 2014.

[331] P. Borisov, A. Hochstrat, X. Chen, W. Kleemann, and C. Binek. Magnetoelectric Switching of Exchange Bias. *Phys. Rev. Lett.*, 94:117203, 2005.

[332] X. Chen, A. Hochstrat, P. Borisov, and W. Kleemann. Magnetoelectric exchange bias systems in spintronics. *Appl. Phys. Lett.*, 89:202508, 2006.

[333] X. He, Y. Wang, N. Wu, A.N. Caruso, E. Vescovo, K.D. Belashchenko, P.A. Dowben, and C. Binek. Robust isothermal electric control of exchange bias at room temperature. *Nat. Mater.*, 9:579–585, 2010.

[334] V. Skumryev, V. Laukhin, I. Fina, X. Martí, F. Sánchez, M. Gospodinov, and J. Fontcuberta. Magnetization Reversal by Electric-Field Decoupling of Magnetic and Ferroelectric Domain Walls in Multiferroic-Based Heterostructures. *Phys. Rev. Lett.*, 106:057206, 2011.

[335] T. Zhao, A. Scholl, F. Zavaliche, K. Lee, M. Barry, A. Doran, M.P. Cruz, Y.H. Chu, C. Ederer, N.A. Spaldin, R.R. Das, D.M. Kim, S.H. Baek, C.B. Eom, and R. Ramesh. Electrical control of antiferromagnetic domains in multiferroic $BiFeO_3$ films at room temperature. *Nat. Mater.*, 5:823–829, 2006.

[336] L.W. Martin, Y.-H. Chu, M.B. Holcomb, M. Huijben, P. Yu, S.-J. Han, D. Lee, S.X. Wang, and R. Ramesh. Nanoscale Control of Exchange Bias with $BiFeO_3$ Thin Films. *Nano Lett.*, 8:2050–2055, 2008.

[337] H. Béa, M. Bibes, F. Ott, B. Dupé, X.-H. Zhu, S. Petit, S. Fusil, C. Deranlot, K. Bouzehouane, and A. Barthélémy. Mechanisms of Exchange Bias with Multiferroic $BiFeO_3$ Epitaxial Thin Films. *Phys. Rev. Lett.*, 100:017204, 2008.

[338] J.T. Heron, M. Trassin, K. Ashraf, M. Gajek, Q. He, S.Y. Yang, D.E. Nikonov, Y.-H. Chu, S. Salahuddin, and R. Ramesh. Electric-Field-Induced Magnetization Reversal in a Ferromagnet-Multiferroic Heterostructure. *Phys. Rev. Lett.*, 107:217202, 2011.

[339] S.M. Wu, S.A. Cybart, P. Yu, M.D. Rossell, J.X. Zhang, R. Ramesh, and R.C. Dynes. Reversible electric control of exchange bias in a multiferroic field-effect device. *Nat. Mater.*, 9:756–761, 2010.

[340] S.M. Wu, S.A. Cybart, D. Yi, J.M. Parker, R. Ramesh, and R.C. Dynes. Full Electric Control of Exchange Bias. *Phys. Rev. Lett.*, 110:067202, 2013.

[341] L. You, B. Wang, X. Zou, Z.S. Lim, Y. Zhou, H. Ding, L. Chen, and J. Wang. Origin of the uniaxial magnetic anisotropy in $La_{0.7}Sr_{0.3}MnO_3$ on stripe-domain $BiFeO_3$. *Phys. Rev. B*, 88:184426, 2013.

[342] Y.-H. Chu, L.W. Martin, M.B. Holcomb, M. Gajek, S.-J. Han, Q. He, N. Balke, C.-H. Yang, D. Lee, W. Hu, Q. Zhan, P.-L. Yang, A. Fraile-Rodríguez, A. Scholl, S.X. Wang, and R. Ramesh. Electric-field control of local ferromagnetism using a magnetoelectric multiferroic. *Nat. Mater.*, 7:478–482, 2008.

[343] M. Trassin, J.D. Clarkson, S.R. Bowden, J. Liu, J.T. Heron, R.J. Paull, E. Arenholz, D.T. Pierce, and J. Unguris. Interfacial coupling in multiferroic/ferromagnet heterostructures. *Phys. Rev. B*, 87:134426, 2013.

[344] J.T. Heron, J.L. Bosse, Q. He, Y. Gao, M. Trassin, L. Ye, J.D. Clarkson, C. Wang, J. Liu, S. Salahuddin, D.C. Ralph, D.G. Schlom, J. Íñiguez, B.D. Huey, and R. Ramesh. Deterministic switching of ferromagnetism at room temperature using an electric field. *Nature*, 516:370–373, 2014.

[345] F. Bonell, Y.T. Takahashi, D.D. Lam, S. Yoshida, Y. Shiota, S. Miwa, T. Nakamura, and Y. Suzuki. Reversible change in the oxidation state and magnetic circular dichroism of Fe driven by an electric field at the FeCo/MgO interface. *Appl. Phys. Lett.*, 102:152401, 2013.

[346] U. Bauer, L. Yao, A.J. Tan, P. Agrawal, S. Emori, H.L. Tuller, S. van Dijken, and G.S.D. Beach. Magneto-ionic control of interfacial magnetism. *Nat. Mater.*, 14:174–181, 2015.

[347] C. Bi, Y. Liu, T. Newhouse-Illige, M. Xu, M. Rosales, J.W. Freeland, O. Mryasov, S. Zhang, S.G.E. te Velthuis, and W.G. Wang. Reversible Control of Co Magnetism by Voltage-Induced Oxidation. *Phys. Rev. Lett.*, 113:267202, 2014.

[348] X. Chen, X. Zhu, W. Xiao, G. Liu, Y.P. Feng, J. Ding, and R.-W. Li. Nanoscale Magnetization Reversal Caused by Electric Field-Induced Ion Migration and Redistribution in Cobalt Ferrite Thin Films. *ACS Nano*, 9:4210–4218, 2015.

[349] S. Couet, M. Bisht, M. Trekels, M. Menghini, C. Petermann, M.J. Van Bael, J.-P. Locquet, R. Rüffer, A. Vantomme, and K. Temst. Electric Field-Induced Oxidation of Ferromagnetic/Ferroelectric Interfaces. *Adv. Funct. Mater.*, 24:71–76, 2014.

[350] M. Fiebig, T. Lottermoser, D. Fröhlich, A.V. Goltsev, and R.V. Pisarev. Observation of coupled magnetic and electric domains. *Nature*, 419:818–820, 2002.

[351] M. Fiebig, A.V. Goltsev, T. Lottermoser, and R.V. Pisarev. Structure and interaction of domain walls in $YMnO_3$. *J. Magn. Magn. Mater.*, 272–276, Part 1:353–354, 2004.

[352] T.I. Kasama, R.J. Harrison, N.S. Church, M. Nagao, J.M. Feinberg, and R.E. Dunin-Borkowski. Ferrimagnetic/ferroelastic domain interactions in magnetite below the Verwey transition. Part I: electron holography and Lorentz microscopy. *Phase Transit.*, 86:67–87, 2013.

[353] J. de la Figuera, Z. Novotny, M. Setvin, T. Liu, Z. Mao, G. Chen, A.T. N'Diaye, M. Schmid, U. Diebold, A.K. Schmid, and G.S. Parkinson. Real-space imaging of the Verwey transition at the (100) surface of magnetite. *Phys. Rev. B*, 88:161410, 2013.

[354] M. Mostovoy. Ferroelectricity in Spiral Magnets. *Phys. Rev. Lett.*, 96:067601, 2006.

[355] I. Dzyaloshinskii. Magnetoelectricity in ferromagnets. *EPL*, 83:67001, 2008.

[356] A.S. Logginov, G.A. Meshkov, A.V. Nikolaev, and A.P. Pyatakov. Magnetoelectric control of domain walls in a ferrite garnet film. *JETP Lett.*, 86:115–118, 2007.

[357] A.S. Logginov, G.A. Meshkov, A.V. Nikolaev, E.P. Nikolaeva, A.P. Pyatakov, and A.K. Zvezdin. Room temperature magnetoelectric control of micromagnetic structure in iron garnet films. *Appl. Phys. Lett.*, 93:182510, 2008.

[358] A.P. Pyatakov, D.A. Sechin, A.S. Sergeev, A.V. Nikolaev, E.P. Nikolaeva, A.S. Logginov, and A.K. Zvezdin. Magnetically switched electric polarity of domain walls in iron garnet films. *EPL*, 93:17001, 2011.

[359] A.I. Popov, Z.V. Gareeva, and A.K. Zvezdin. Magnetoelectricity of domain walls of rare-earth iron garnets. *Phys. Rev. B*, 92:144420, 2015.

[360] H.-B. Chen, Y.-H. Liu, and Y.-Q. Li. Electric field control of multiferroic domain wall motion. *J. Appl. Phys.*, 115:133913, 2014.

[361] A.J. Schellekens, A. van den Brink, J.H. Franken, H.J.M. Swagten, and B. Koopmans. Electric-field control of domain wall motion in perpendicularly magnetized materials. *Nat. Commun.*, 3:847, 2012.

[362] U. Bauer, S. Emori, and G.S.D. Beach. Electric field control of domain wall propagation in Pt/Co/GdO_x films. *Appl. Phys. Lett.*, 100:192408, 2012.

[363] P.M. Shepley, A.W. Rushforth, M. Wang, G. Burnell, and T.A. Moore. Modification of perpendicular magnetic anisotropy and domain wall velocity in Pt/Co/Pt by voltage-induced strain. *Sci. Rep.*, 5:7921, 2015.

[364] E. De Ranieri, P.E. Roy, D. Fang, E.K. Vehsthedt, A.C. Irvine, D. Heiss, A. Casiraghi, R.P. Campion, B.L. Gallagher, T. Jungwirth, and J. Wunderlich. Piezoelectric control of the mobility of a domain wall driven by adiabatic and non-adiabatic torques. *Nat. Mater.*, 12:808–814, 2013.

[365] D. Chiba, M. Kawaguchi, S. Fukami, N. Ishiwata, K. Shimamura, K. Kobayashi, and T. Ono. Electric-field control of magnetic domain-wall velocity in ultrathin cobalt with perpendicular magnetization. *Nat. Commun.*, 3:888, 2012.

[366] J.H. Franken, Y. Yin, A.J. Schellekens, A. van den Brink, H.J.M. Swagten, and B. Koopmans. Voltage-gated pinning in a magnetic domain-wall conduit. *Appl. Phys. Lett.*, 103:102411, 2013.

[367] A. Bernand-Mantel, L. Herrera-Diez, L. Ranno, S. Pizzini, J. Vogel, D. Givord, S. Auffret, O. Boulle, I.M. Miron, and G. Gaudin. Electric-field control of domain wall nucleation and pinning in a metallic ferromagnet. *Appl. Phys. Lett.*, 102:122406, 2013.

[368] U. Bauer, S. Emori, and G.S.D. Beach. Voltage-gated modulation of domain wall creep dynamics in an ultrathin metallic ferromagnet. *Appl. Phys. Lett.*, 101:172403, 2012.

[369] U. Bauer, S. Emori, and G.S.D. Beach. Voltage-controlled domain wall traps in ferromagnetic nanowires. *Nat. Nanotechnol.*, 8:411–416, 2013.

[370] S.A. Cavill, D.E. Parkes, J. Miguel, S.S. Dhesi, K.W. Edmonds, R.P. Campion, and A.W. Rushforth. Electrical control of magnetic reversal processes in magnetostrictive structures. *Appl. Phys. Lett.*, 102:032405, 2013.

[371] D.E. Parkes, S.A. Cavill, A.T. Hindmarch, P. Wadley, F. McGee, C.R. Staddon, K.W. Edmonds, R.P. Campion, B.L. Gallagher, and A.W. Rushforth. Non-volatile voltage control of magnetization and magnetic domain walls in magnetostrictive epitaxial thin films. *Appl. Phys. Lett.*, 101:072402, 2012.

[372] T. Brintlinger, S.-H. Lim, K.H. Baloch, P. Alexander, Y. Qi, J. Barry, J. Melngailis, L. Salamanca-Riba, I. Takeuchi, and J. Cumings. In Situ Observation of Reversible Nanomagnetic Switching Induced by Electric Fields. *Nano Lett.*, 10:1219–1223, 2010.

[373] T.-K. Chung, G.P. Carman, and K.P. Mohanchandra. Reversible magnetic domain-wall motion under an electric field in a magnetoelectric thin film. *Appl. Phys. Lett.*, 92:112509, 2008.

[374] J.L. Hockel, A. Bur, T. Wu, K.P. Wetzlar, and G.P. Carman. Electric field induced magnetization rotation in patterned Ni ring/$Pb(Mg_{1/3}Nb_{2/3})O_3]_{(1-0.32)}$-$[PbTiO_3]_{0.32}$ heterostructures. *Appl. Phys. Lett.*, 100:022401, 2012.

[375] H. Sohn, M.E. Nowakowski, C.-Y. Liang, J.L. Hockel, K. Wetzlar, S. Keller, B.M. McLellan, M.A. Marcus, A. Doran, A. Young, M. Kläui, G.P. Carman,

J. Bokor, and R.N. Candler. Electrically Driven Magnetic Domain Wall Rotation in Multiferroic Heterostructures to Manipulate Suspended On-Chip Magnetic Particles. *ACS Nano*, 9:4814–4826, 2015.

[376] J. Dean, M.T. Bryan, T. Schrefl, and D.A. Allwood. Stress-based control of magnetic nanowire domain walls in artificial multiferroic systems. *J. Appl. Phys.*, 109:023915, 2011.

[377] S.M. Rossnagel. Thin film deposition with physical vapor deposition and related technologies. *J. Vac. Sci. Technol. A*, 21:S74–S87, 2003.

[378] Donald M. Mattox. *Handbook of Physical Vapor Deposition (PVD) Processing*. William Andrew, 2010.

[379] P.R. Willmott. Deposition of complex multielemental thin films. *Prog. Surf. Sci.*, 76:163–217, 2004.

[380] Robin F.C. Farrow. *Molecular Beam Epitaxy: Applications to Key Materials*. Elsevier Science, 2012.

[381] K.-G. Wagner. A brief review of Knudsen-cells for applications in experimental research. *Vacuum*, 34:743–746, 1984.

[382] A. Beck, H. Jungen, B. Bullemer, and I. Eisele. A new effusion cell arrangement for fast and accurate control of material evaporation under vacuum conditions. *J. Vac. Sci. Technol. A*, 2:5–8, 1984.

[383] J. McCord. Progress in magnetic domain observation by advanced magneto-optical microscopy. *J. Phys. D: Appl. Phys.*, 48:333001, 2015.

[384] J. Kerr. On rotation of the plane of polarization by reflection from the pole of a magnet. *Philos. Mag. Series 5*, 3:321–343, 1877.

[385] J. Kerr. On reflection of polarized light from the equatorial surface of a magnet. *Philos. Mag. Series 5*, 5:161–177, 1878.

[386] P.N. Argyres. Theory of the Faraday and Kerr Effects in Ferromagnetics. *Phys. Rev.*, 97:334–345, 1955.

[387] G. Traeger, L. Wenzel, and A. Hubert. Computer experiments on the information depth and the figure of merit in magnetooptics. *Phys. Status Solidi A*, 131:201–227, 1992.

[388] M.R. Scheinfein, J. Unguris, J.L. Blue, K.J. Coakley, D.T. Pierce, R.J. Celotta, and P.J. Ryan. Micromagnetics of domain walls at surfaces. *Phys. Rev. B*, 43:3395–3422, 1991.

[389] S.D. Bader and J.L. Erskine. Magneto-Optical Effects in Ultrathin Magnetic Structures. In B. Heinrich and J.A.C. Bland, editors, *Ultrathin Magnetic Structures II*, pages 297–325. Springer, 1994.

[390] Z.Q. Qiu and S.D. Bader. Surface magneto-optic Kerr effect. *Rev. Sci. Instrum.*, 71:1243–1255, 2000.

[391] B. Jiang, Y. Bai, W. Chu, Y. Su, and L. Qiao. Direct observation of two 90° steps of 180° domain switching in $BaTiO_3$ single crystal under an antiparallel electric field. *Appl. Phys. Lett.*, 93:152905, 2008.

[392] J. Unguris, S.R. Bowden, D.T. Pierce, M. Trassin, R. Ramesh, S.-W. Cheong, S. Fackler, and I. Takeuchi. Simultaneous imaging of the ferromagnetic and ferroelectric structure in multiferroic heterostructures. *APL Mat.*, 2:076109, 2014.

[393] R. Allenspach. Spin-polarized scanning electron microscopy. *IBM J. Res. Dev.*, 44:553–570, 2000.

[394] H. Hopster and H.P. Oepen. *Magnetic microscopy of nanostructures*. Springer, 2005.

[395] H.P. Oepen, G. Steierl, and J. Kirschner. Scanning electron microscope with polarization analysis: Micromagnetic structures in ultrathin films. *J. Vac. Sci. Technol. B*, 20:2535–2538, 2002.

[396] D.T. Pierce, J. Unguris, and R.J. Celotta. Magnetic Coupling and Magnetoresistance. In B. Heinrich and J.A.C. Bland, editors, *Ultrathin Magnetic Structures II*, pages 45–194. Springer, 1994.

[397] M.R. Scheinfein, J. Unguris, M.H. Kelley, D.T. Pierce, and R.J. Celotta. Scanning electron microscopy with polarization analysis (SEMPA). *Rev. Sci. Instrum.*, 61:2501–2527, 1990.

[398] F. Porrati. *Spatially varying magnetic anisotropies in ultrathin films*. PhD thesis, Martin-Luther-Universität Halle-Wittenberg, Halle, 2002.

[399] M.J. Donahue and D.G Porter. *OOMMF user's guide, Version 1.0*. Interagency Report NISTIR 6376. National Institute of Standards and Technology, Gaithersburg, MD, 1999.

[400] A. Vansteenkiste and B. Van de Wiele. MuMax: A new high-performance micromagnetic simulation tool. *J. Magn. Magn. Mater.*, 323:2585–2591, 2011.

[401] A. Vansteenkiste, J. Leliaert, M. Dvornik, M. Helsen, F. Garcia-Sanchez, and B. Van Waeyenberge. The design and verification of MuMax3. *AIP Adv.*, 4:107133, 2014.

[402] W. Wang, C. Mu, B. Zhang, Q. Liu, J. Wang, and D. Xue. Two-dimensional periodic boundary conditions for demagnetization interactions in micromagnetics. *Comput. Mater. Sci.*, 49:84–87, 2010.

[403] A. Kakay, E. Westphal, and R. Hertel. Speedup of FEM Micromagnetic Simulations With Graphical Processing Units. *IEEE Trans. Magn.*, 46:2303–2306, 2010.

[404] R.C. Hall. Magnetic Anisotropy and Magnetostriction of Ordered and Disordered Cobalt-Iron Alloys. *J. Appl. Phys.*, 31:S157–S158, 1960.

[405] P. Li, A. Chen, D. Li, Y. Zhao, S. Zhang, L. Yang, Y. Liu, M. Zhu, H. Zhang, and X. Han. Electric Field Manipulation of Magnetization Rotation and Tunneling Magnetoresistance of Magnetic Tunnel Junctions at Room Temperature. *Adv. Mater.*, 26:4320–4325, 2014.

[406] V.A. Vas'ko, J.O. Rantschler, and M.T. Kief. Structure, stress, and magnetic properties of high saturation magnetization films of FeCo. *IEEE Trans. Magn.*, 40:2335– 2337, 2004.

[407] M.A. Basith, S. McVitie, T. Strache, M. Fritzsche, A. Muecklich, J. Fassbender, and J. McCord. Lorentz TEM Imaging of Stripe Structures Embedded in a Soft Magnetic Matrix. *Phys. Rev. Appl.*, 4:034012, 2015.

[408] S. Brivio, C. Rinaldi, D. Petti, R. Bertacco, and F. Sanchez. Epitaxial growth of Fe/$BaTiO_3$ heterostructures. *Thin Solid Films*, 519:5804–5807, 2011.

[409] D. López González, A. Casiraghi, B. Van de Wiele, and S. van Dijken. Reconfigurable magnetic logic based on the energetics of pinned domain walls. *Appl. Phys. Lett.*, 108:032402, 2016.

[410] B Van de Wiele, S.J. Hämäläinen, P. Balaz, F. Montoncello, and S. van Dijken. Tunable short-wavelength spin wave excitation from pinned magnetic domain walls. *Sci. Rep.*, 6:21330, 2016.

[411] B. Van de Wiele, L. Laurson, K.J.A. Franke, and S. van Dijken. Electric field driven magnetic domain wall motion in ferromagnetic-ferroelectric heterostructures. *Appl. Phys. Lett.*, 104:012401, 2014.

[412] B. Van de Wiele, J. Leliaert, K.J.A. Franke, and S. van Dijken. Electric-field-driven dynamics of magnetic domain walls in magnetic nanowires patterned on ferroelectric domains. *New J. Phys.*, 18:033027, 2016.

Aalto-DD 95/2016

ISBN 978-952-60-6816-9 (printed)
ISBN 978-952-60-6817-6 (pdf)
ISSN-L 1799-4934
ISSN 1799-4934 (printed)
ISSN 1799-4942 (pdf)

Aalto University
School of Science
Department of Applied Physics
www.aalto.fi

BUSINESS +
ECONOMY

ART +
DESIGN +
ARCHITECTURE

SCIENCE +
TECHNOLOGY

CROSSOVER

DOCTORAL
DISSERTATIONS